UNIVERSITÀ
DI PAVIA

KU LEUVEN

UNIVERSITÀ DEGLI STUDI DI PAVIA

Ph.D. School in Electronics, Computer Science and Electrical Engineering

Faculty of Engineering

KATHOLIEKE UNIVERSITEIT LEUVEN

Arenberg Doctoral School

Faculty of Engineering Science

DEVELOPMENT OF MICROFLUIDIC SENSORS BY ADDITIVE MANUFACTURING

Giulia Maria Rocco

Dissertation presented in partial fulfilment of the requirements for the

Joint Doctoral Degree of

Dottore di Ricerca in Ingegneria Elettronica, Informatica ed Elettrica

Doctor of Engineering Science: Electrical Engineering

Supervisors:

Prof. Maurizio Bozzi

Prof. Dominique Schreurs

CYCLE XXXII

2016-2019

Life is an opportunity, benefit from it.
Life is a beauty, admire it.
Life is bliss, taste it.
Life is a dream, realize it.
Life is a challenge, meet it.
Life is a duty, complete it.
Life is a game, play it.
Life is costly, care for it.
Life is wealth, keep it.
Life is love, enjoy it.
Life is mystery, know it.
Life is a promise, fulfill it.
Life is a sorrow, overcome it.
Life is a song, sing it.
Life is a struggle, accept it.
Life is a tragedy, confront it.
Life is an adventure, dare it.
Life is luck, make it.
Life is too precious, do not destroy it.
Life is Life, fight for it!

Mother Teresa

Abstract

Today, additive manufacturing (AM) technology is well-known to everybody: each of us has, at least once, heard about that and many have already seen a 3D printer at work. In last years, the cost reduction of 3D printers has meant that AM was no longer used just for rapid prototyping but, also, for the manufacturing of many end-use products. Moreover, its benefits (the material efficiency, the possibility to produce complex shapes in very fast time and at low-cost,...), attracted also the scientists, leading them to use this technology in their research. Recently, 3D-printing made its appearance in the microwave field, and the number of papers presenting devices fabricated with this technology grows every year more.

It is within this scenario that my PhD thesis is contributing, being entirely dedicated to 3D-printing technology and its applications in the development of microwave devices. In particular, my work is focused on the realization of microfluidic devices based on resonant cavities. The devices were designed, fabricated, and experimentally verified to demonstrate the potential of merging the microwave field with 3D printed sensing devices.

The thesis is organized in six chapters. In the first part, an introductory frame outlines the panorama in which the PhD thesis is situated, together with the state of the art of AM and microfluidics as applied to the microwave field and, eventually, the adopted technologies. The second part, the core of the thesis, deals with the fabricated microfluidic sensors, that is, devices that allow to extract liquids' dielectric properties. The retrieval of liquids properties, i.e., dielectric permittivity and loss tangent, has very important applications in chemical and biological fields. In this work, microfluidic sensors are realized through 3D-printed resonant cavities with a (3D-printed) pipe inside, where liquids under test (LUT) can be injected and their properties extracted. Sensors with two different geometries have been analyzed. The first one consists in a square Substrate Integrated Waveguide (SIW) cavity with a

multi-folded pipe inside. In the second structure, instead, the high quality factor of spherical-like shapes is exploited. A pumpkin-shape cavity resonator is fabricated, with a pipe passing, straight, between the two poles. One of the main advantages of AM fabrication is the possibility of emptying both structures, so to minimize as much as possible the dielectric losses due to the substrate. Moreover, the pumpkin structure, realized with a 2 mm-thick dielectric shell, was metallized in the inner part, thanks to electroplating. This guaranteed an increase in quality factor, especially if compared with the square structure. Both these structures were tested with nine different liquids, consisting of mixtures of water and isopropanol. To extract dielectric permittivity and loss tangent of the LUTs, the shift in the resonant frequency on one hand and the change of the quality factor on the other hand, have been considered. In particular, the procedure for the extraction of the dielectric permittivity has been improved, with respect to what can be read in literature, and also a novel method for the extraction of the loss tangent is proposed. The intention to create a self-sustained device for the retrieval of LUTs properties, is then pointed out. Such an investigation has culminated in the realization of an oscillator based on the aforementioned 3D-printed resonator. The design of the oscillator was performed in such a way to obtain an output signal with a working frequency similar to the resonator one and dependent on the LUT injected in the cavity. With a spectrum analyzer, the oscillation frequency was measured in different cases, and the permittivity of the different LUTs was obtained with good accuracy.

Beknopte samenvatting

Tegenwoordig is iedereen bekend met additieve productietechnologie (AM): ieder van ons heeft daar minstens één keer van gehoord en velen hebben al een 3D-printer aan het werk gezien. In de afgelopen jaren heeft de kostreductie van 3D-printers ertoe geleid dat AM niet langer alleen werd gebruikt voor snelle prototyping, maar ook voor de productie van vele eindproducten. Bovendien trokken de voordelen ervan (oa. materiaalefficiëntie, de mogelijkheid om complexe vormen in zeer snelle tijd en tegen lage kosten te produceren, ...) ook de wetenschappers aan, waardoor ze deze technologie in hun onderzoek gebruikten. Onlangs verscheen 3D-printing in het domein van mikrogolftechniek en het aantal artikels over componenten die met deze technologie zijn gefabriceerd, groeit elk jaar meer.

Het is binnen dit scenario dat mijn doctoraatsproefschrift bijdraagt, hetgeen volledig gewijd is aan 3D-printtechnologie en de toepassingen ervan bij de ontwikkeling van microgolfcomponenten. Mijn werk is met name gericht op de realisatie van microfluïdische componenten op basis van resonerende caviteiten. De componenten werden ontworpen, gefabriceerd en experimenteel geverifieerd om het potentieel van het samenbrengen van het microgolfdomein en 3D-geprinte sensoren aan te tonen.

Het proefschrift is georganiseerd in zes hoofdstukken. In het eerste deel schetst een inleidend kader het panorama waarin het proefschrift zich situeert, samen met de stand van de techniek van AM en microfluïdica toegepast op het microgolfdomein en, uiteindelijk, de aangewende technologieën. Het tweede deel, de kern van het proefschrift, gaat over de gefabriceerde microfluïdische sensoren, dit wil zeggen sensoren die het mogelijk maken om diëlektrische eigenschappen van vloeistoffen te extraheren. Het bepalen van de vloeistofeigenschappen, d.w.z. diëlektrische permittiviteit en verlies tangens, heeft zeer belangrijke toepassingen in de chemie en biologie. In dit doctoraatswerk worden microfluïdische sensoren gerealiseerd door

3D-geprinte resonantiecaviteiten met een (3D-geprinte) pijp erin, waar vloeistoffen die getest worden (LUT) kunnen worden geïnjecteerd en vervolgens hun eigenschappen worden geëxtraheerd. Sensoren met twee verschillende geometrieën werden geanalyseerd. De eerste bestaat uit een vierkante caviteit op basis van een substraat-geïntegreerde golfgeleider (SIW) met een meervoudig gevouwen pijp erin. In de tweede structuur wordt in plaats daarvan de hoge kwaliteitsfactor van bolvormige vormen benut. Een pompoenachtige caviteitsresonator werd vervaardigd, met een pijp die recht door de twee polen loopt. Eén van de belangrijkste voordelen van AM-fabricage is de mogelijkheid om beide structuren leeg te maken, om alzo de diëlektrische verliezen door het substraat zoveel mogelijk te minimaliseren. Bovendien werd de pompoenstructuur, gerealiseerd met 2 mm dikke diëlektrische schaal, gemetalliseerd in het binnenste gedeelte, dankzij galvanisatie. Dit garandeert een toename van de kwaliteitsfactor, vooral in vergelijking met de vierkante structuur. Beide structuren werden getest met negen verschillende vloeistoffen, bestaande uit mengsels van water en isopropanol. Om de diëlektrische permittiviteit en verlies tangens van de LUT's te extraheren, wordt de verschuiving in resonantiefrequentie enerzijds en de verandering van de kwaliteitsfactor anderzijds, in rekening gebracht. In het bijzonder werd de procedure voor de extractie van de diëlektrische permittiviteit verbeterd, relatief ten opzichte van bestaande literatuur, en een nieuwe methode voor de extractie van de verliestangens wordt voorgesteld. Vervolgens wordt gewezen op de intentie om een ontwerp te maken voor het automatisch bepalen van de LUT's-eigenschappen. Dit onderzoek heeft geleid tot de realisatie van een oscillator op basis van de eerder genoemde 3D-geprinte resonator. Het ontwerp van de oscillator werd zodanig uitgevoerd dat een uitgangssignaal wordt verkregen met een werkingsfrequentie vergelijkbaar met die van de resonator en afhankelijk van de LUT die in de caviteit werd geïnjecteerd. Met een spectrum analyser werd de oscillatiefrequentie voor verschillende gevallen gemeten en werd de permittiviteit van verschillende LUT's met goede nauwkeurigheid verkregen.

Abbreviations

ABS	Acrynolite Butadiene Styrene
ADS	Advanced Design System
AM	Additive Manufacturing
ASTM	American Society for Testing and Materials
CAD	Computer-Aided Drafting
CST	Computer Simulation Technology
EM	Electromagnetic
FDM	Fused Deposition Modeling
HFSS	High Frequency Structure Simulator
LUT	Liquid Under Test
MIMO	Multiple-input-multiple-output
SA	Spectrum Analyzer
SIW	Substrate Integrated Waveguide
SLA/SL	Stereolitography
TE	Transverse Electric
TM	Transverse Magnetic
WR	Waveguide Rectangular
VNA	Vector Network Analyzer

This page is intentionally left blank

List of Symbols

f	Hz	Frequency
f_c	Hz	Cutoff frequency
f_0	Hz	Resonance frequency
$Q - factor$	-	Quality factor
Q_c	-	Quality factor related to conductor losses
Q_d	-	Quality factor related to dielectric losses
Q_L	-	Loaded quality factor
Q_U	-	Unloaded quality factor
S_{11}	-	Ratio of reflected and incident wave at port 1
S_{11}^{sim}	-	Simulated value of S_{11}
S_{11}^{meas}	-	Measured value of S_{11}
S_{21}	-	Ratio of reflected wave at port 2 and incident wave at port 1
Tanδ	-	Dielectric loss coefficient of a substrate
ε	F/m	Complex permittivity
$\varepsilon^{'}$	-	Real part of complex permittivity
ε''	-	Imaginary part of complex permittivity
ε_0	F/m	Permittivity of vacuum, $8.854 \cdot 10^{-12}$
ε_r	-	Relative permittivity of a substrate
ε_e	-	Effective relative permittivity of a dielectric substrate
λ	m	Wavelength
λ_0	m	Wavelength in vacuum
λ_c	m	Cutoff wavelength
μ	H/m	Complex permeability
$\mu^{'}$	-	Real part of complex permeability

μ''	-	Imaginary part of complex permeability
μ_0	H/m	Permeability of vacuum, $4\pi \cdot 10^{-7}$
ω	rad/s	Angular frequency
ω_0	rad/s	Angular resonance frequency

Contents

This page is intentionally left blank

List of Figures

This page is intentionally left blank

List of Tables

Chapter 1

Introduction

We are going toward a fully connected world, where a huge number of wireless devices are connected among them and with people to provide any kind of information. We expect to have billions of sensors to provide an enormous quantity of information, that can be used in different services and that will have, as first purpose, improving the quality of life. Of course, this increasing need of wireless sensors and their future integration with every-day life, requires the development of compact wireless systems that have to be extremely low cost, power autonomous, easy to fabricate and with low weight [1],[2].

The natural choice is to exploit the recent progresses made in the field of Additive Manufacturing to create a class of fully printed low-cost RF sensors that, in near future, could constitute nodes of this network. The use of AM technologies for this aim, indeed, would add flexibility in creating all kinds of models in different scales, materials and colors, and, finally, would saves both costs - at least for small or medium productions - and time [3],[4],[5].

In this thesis, 3D-printed microfluidic sensors, realized in the form of cavity resonators, are presented. These sensors, conceived to be used in chemical and biological applications, allow the characterization of liquids in the lower portion of the UWB (3.2 GHz - 4.8 GHz). This choice for resonators' working frequencies has been done in order to guarantee a future applicability in wireless sensor networks (WSN) [6],[7],[8]. Moreover, since we are dealing with 3D-printed cavity resonators, the selected band of frequency offers the best tradeoff between losses and cavity dimensions. On one hand, indeed, if higher GHz frequencies are considered, the surface roughness of 3D-printed dielectrics can seriously degrade S-parameters loss; on the other hand, however, the dimensions of the cavities proportionally increases when the frequencies decrease, leading to realize very bulky devices.

The history of additive manufacturing and microfluidics is presented in subsection 1.1.1 and subsection 1.2.1, respectively. Afterwards, the state of the art of additive manufactured and microfluidic devices is discussed in subsection 1.1.4 and subsection 1.2.2. Together with the state of the art, benefits and drawbacks in using additive manufacturing techniques are reported in subsection 1.1.2. The previous discussion leads to motivation and objectives for research of 3D-printed microfluidic sensors, which is presented in section 1.3. Finally, in section 1.4, the outline of the complete doctoral thesis is presented.

1.1 Additive Manufacturing

Today, 3D printing is well-known to everybody: each of us has, at least once, heard about that and many have already seen a 3D printer at work. Nonetheless, the history of this extraordinary technological advancement - still in progress - is unknown to most. In fact, most people believe that 3D printing and additive manufacturing represent a recent phenomenon but, actually, the birth of this technology can be traced back to the beginning of the 1980s [9],[10].

1.1.1 A Brief History

It was in 1981 that Hideo Kodama, a researcher at Municipal Industrial Research Institute in Nagoya, registered the patent for two rapid prototyping techniques based on the UV-photo-curing of polymers.

Two years later Charles W. Hull, an American researcher, while using UV rays to harden paints, had the idea to exploit this technique to realize 3D objects. It was Hull to create the term *stereolithography*, using it in his U.S. Patent «Apparatus for Production of Three-Dimensional Objects by Stereolithography» issued on March 11, 1986 [11].

In the same years, Carl Deckard developed Chuck Hull's ideas and developed the Selective Laser Sintering (SLS) technique - a process that uses powder (instead of liquid material) which, hardened by a high power laser beam, creates the object layer by layer.

In the 1989, the first SLA printer was produced and Scott Crump invented a revolutionary 3D printing technique, the FDM (Fused Deposition Modeling). He put aside both the laser and the powder, exploiting melted plastic that, deposited layer by layer through a nozzle, fabricated the object.

In 1993 it was the turn of MIT in Boston, where the 4th printing technology was developed. It was then possible to print coloured objects - up to a maximum of 28 -

and for the first time the term *3D-printing* was used.

In 1995, at the Fraunhofer Institute in Munich, Selective Laser Melting technique was used for the first time. Thanks to this method, it is possible to melt metal powders obtaining objects with a density of 98%.

In 2001 Luke Massella received one of the first 3D-printed bladders, thanks to the Wake Forest Institute for Regenerative Medicine, in North Carolina. It was made by a combination of 3D-printed biomaterials and his own cells. Luke is now one of about 10 people alive thanks to the implantation of a replacement bladder grown from his own cells [12].

In the meanwhile, Electron Beam Melting was developed, and an Irish company invented 3D Paper Laminated printing. This technique consists in overlapping sheets of paper on which it has been printed, with thus the possibility of using many colors.

Another great turning point in 3D-printing took place in 2005, when, at the University of Bath, the RepRap (Replicating Rapid Prototyper) project was started. RepRap is an open-source project which aims to build self-replicating machines, that 3D-printers that can print most of their own components. The idea is to "democratize" 3D-printing, by expanding the technology to people all around the world. Since the project is all about replication and evolution, the initial RepRap printers (the first one, "Darwin", was released in March 2007) are named after famous evolutionary biologists.

In 2006 the first SLS machine became commercially viable and this opened the door to on-demand manufacturing of industrial parts.

In 2010 was developed Contour Crafting, a building printing technology that, employing computer-controlled gantries, allows to build edifices rapidly and with substantially less manual labor. NASA demonstrated interest in that, since potential applications of this technology could include constructing lunar structures with a material that is 90% lunar and only 10% transported from Earth.

A year later, an 83-year-old woman got a 3D-printed jaw thanks to the joint work of researchers at Hasselt University, in Belgium, and LayerWise company (now 3D Systems Leuven).

Thus we come to 2019, when the longest 3D printed pedestrian bridge in the world was inaugurated in Shanghai [13].

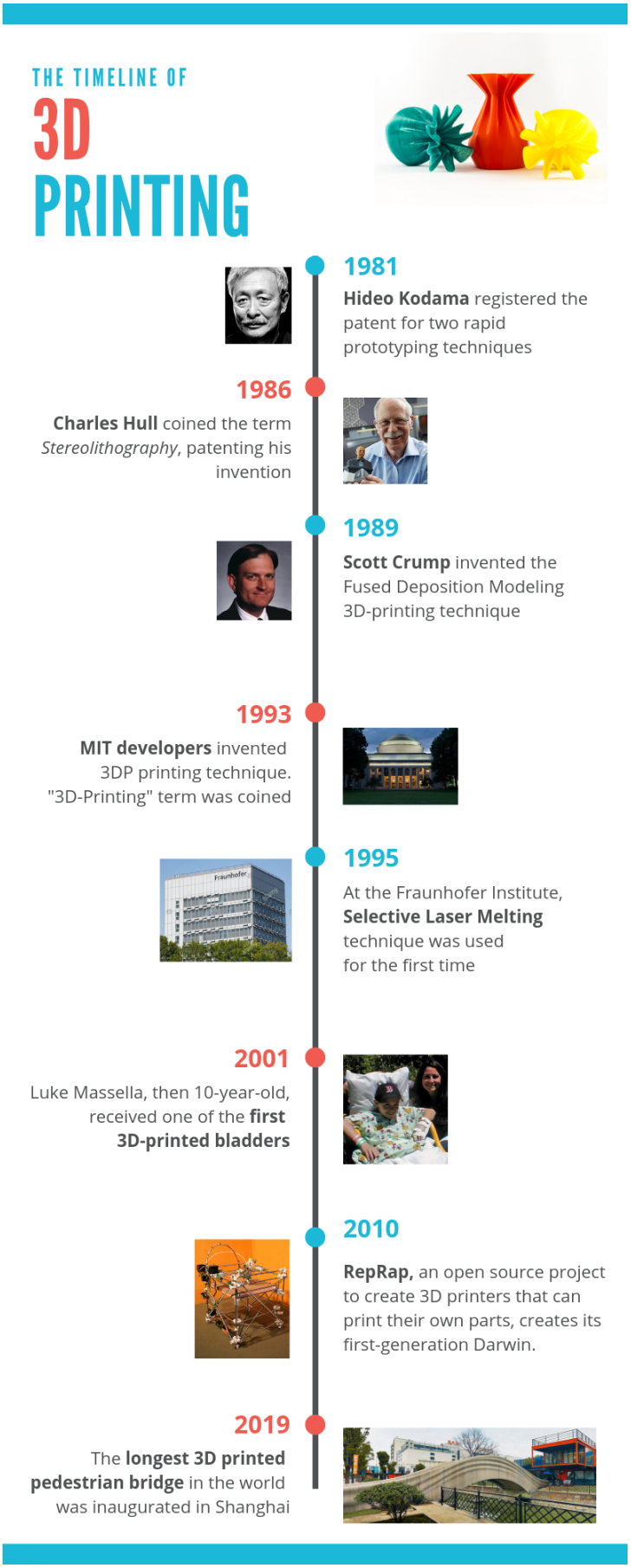

Figure 1.1: A timeline of the most important steps in 3D printing history.

What this brief history of the 3D-printing tells us is that technology is continuing to advance very quickly. Today, desktop 3D-printers are cheaper and better than ever and are continuing to improve. Soon, every home will have a 3D-printer.

1.1.2 Additive Manufacturing Benefits and Drawbacks

After this introduction, the first questions that arise regard the real benefits that such a technology would bring and why these would be interesting for future applications [14]. In the following, I gathered the main ones:

- First of all this technology allows to print objects in one process and easily produces complex shapes. Traditional constraints of manufacturing are thus reduced or eliminated.
- Unlike many widely used manufacturing techniques, no tooling is required, thus any high cost barrier to production is eliminated.
- Parts can be sent anywhere digitally, and printed in homes or locations near to consumers, reducing dependence on transport.
- Compared to conventional techniques with more geometric limitations, additive manufacturing can produce models quickly (in hours, not more in weeks!).
- Additively manufactured parts can be fully customised; this is valid in particular within the medical sector, where 3D-printed components can be tailored to patient's individual requirements.
- Material efficiency, due to the exact production of parts and no overproduction based on estimated demand. The material required matches the material used.
- Commercial advantage and increased competitiveness, in the form of reduced costs and risk, as the development time from concept to manufacturing is minimised.

Of course, like any other manufacturing technique, even 3D-printing presents some handicaps [15], [16]:

- Additive manufacturing is relatively expensive when it comes to large-scale production, where traditional manufacturing still carries lower costs.
- The surface finish and dimensional accuracy may present lower quality with respect to traditional manufacturing methods.
- Layering and multiple interfaces can possibly cause defects in the fabricated components.
- In most cases, polymer products are lower than 1 cubic meter in size, while metal parts may only be about 30 cubic decimeters and, the use of larger machines

comes at a cost.

- Extensive knowledge of material design and the additive manufacturing machine itself is required to make quality parts.

While it may not yet be the most cost-effective way to produce products in large quantities, the technology is advancing very rapidly and is here to stay. As the numbers of machines increases, 3D-printing becomes more and more affordable over time, whereas traditional milling machines remain relatively expensive and inaccessible for small or medium companies.

1.1.3 Additive Manufacturing Applications

AM applications are limitless. While early use of AM focused just on rapid prototyping, nowadays the use of AM regards rapid manufacturing of end-use products in aircraft, automobiles, biomedicine, space, construction, art and even jewelry fields.

If one would like to describe the state-of-the-art of 3D-Printing in all the application fields, an entire thesis would not be enough. I thus report just few examples of the most exciting applications of 3D-printing in biomedical and space sectors.

As regards the biomedical field, 3D-printing can be exploited for the fabrication of faithful reproduction of anatomical structures (for surgical planning and education purposes) and patient-specific devices, in tissue engineering and regenerative medicine. The University of Pavia participates to RAWINTS (Rapid Skin Wound healing by Integrated Tissue engineering and Sensing), an international project funded by NATO *Science for Peace and Security Programme*, which aims to generate artificial human disposable skin or mucosa patches (Fig. 1.2) for applications in case of medical emergencies [17].

Figure 1.2: Artificial human disposal patches providing fast relief to civilians or military personnel injured by chemical agents [17].

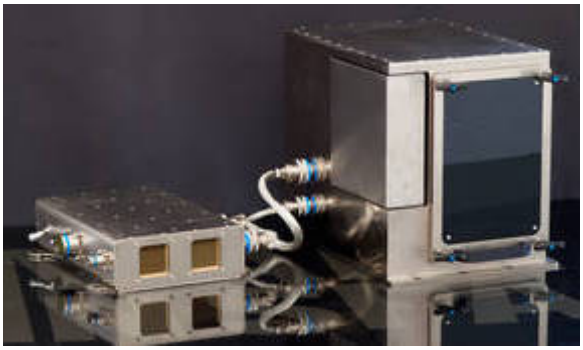

Figure 1.3: Portal, the 3D-printer developed by the American company *Made in Space* [19].

As concerns the space field, the American company *Made In Space*, assembled Portal, the first 3D printer that flew to the International Space Station, in 2014 [18], [19]. The printer (Fig. 1.3) has the size of a small microwave oven, and was placed inside a Microgravity Science Glovebox (a closed container where any element produced by the 3D printer - fumes, micro particles or other - remains confined) to carry out experiments provided by the specific NASA programmes. In 2016 *Made In Space* sent a second 3D printer, the *Additive Manufacturing Facility*, to ISS. With these 3D printers, it will be possible to manufacture tools and hardware components on demand, without the need of waiting for a visiting vehicle that delivers the required components.

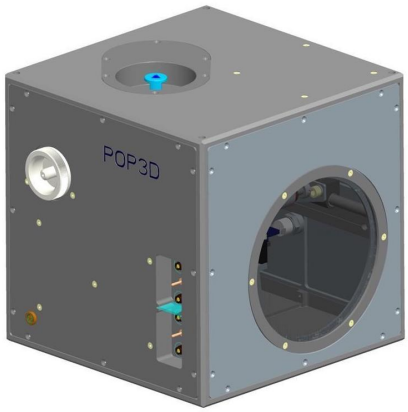

Figure 1.4: POP3D, the 3D-printer designed and built by Italian companies *Altran* and *Thales Alenia* [21].

In 2015, Europe's very first 3D printer in space was installed aboard the ISS [20],[21]. Portable On-Board Printer (POP3D) (Fig. 1.4) was designed and built in Italy thanks to a collaboration between Altran and Thales Alenia, and was put to the test as part of Samantha Cristoforetti's mission. The unit was a cube with 25 cm sides and printed with biodegradable and harmless plastic. This experiment consisted of one automated-fabrication session that produced, in approximately 50 minutes, one small

object, which was then returned to ground for analysis. The purpose of using in space a technology already used on the ground, was mainly to increase the technological maturity of polymer additive manufacturing process in microgravity conditions, but also constituted a promotion for further developments of 3D printing space applications.

1.1.4 Additive Manufacturing and Microwaves: State of the Art

In recent years, a large number of papers have been published about the possibility of integrating the 3D-printing in the development of wireless sensors, because of the huge benefits that this would bring. In [22], a novel solar energy and EM harvesting system is studied, and 3D-printing was used to fabricate the package for the antenna, in order to precisely control the distance between the ground of the antenna and the reflector (Fig.1.5).

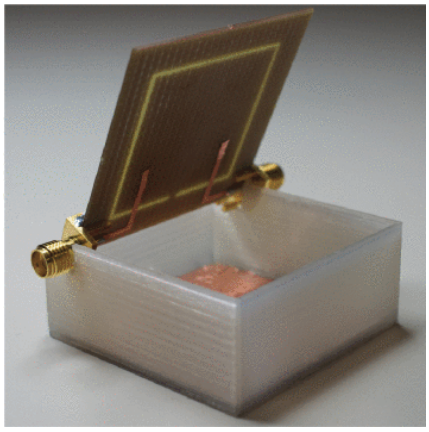

Figure 1.5: Top view of the prototype of rectangular shorted slot antenna with a flexible film solar cell on top [22].

3D-printing techniques can also be used, in addition to metallization methods like inkjet printing/metal coating/metal plating/liquid metal paste, for the implementation of low cost microwave components and antennas.

Here are listed some of the most relevant results reported in recent years literature:

- in [23] a flexible loop antenna, working at 2.4 GHz, is realized for wearable bio-monitoring purposes (Fig. 1.6(a));
- in [24] a 3D-printed LC tank is used as passive wireless-resonant sensor in food quality monitoring (Fig. 1.6(b)) ;
- in [25] an inkjet printed flexible Van-Atta reflectarray is presented, for applications in ubiquitous smart skins and the IoT multisensing topologies (Fig. 1.6(c));

- in [26] 3D-printing technology is used to manufacture a multiple-input-multiple-output (MIMO) antenna for 5G base stations (Fig. 1.6(d));
- in [27] a two-turn helical antenna integrated with 3-D inkjet printing lens is presented for the first time (Fig. 1.6(e));
- in [28] a ball grid array (BGA) module, working at 130 GHz, is integrated in 3D-printed plastic lens antenna (Fig. 1.6(f));
- in [29] stereolithography 3D-printing technique has been used to realize filters with mushroom-shaped resonators (Fig. 1.6(g));
- in [30] a MIMO antenna system, based on four annular slot antennas, is realized thanks to stereolithography 3D-printing technology and an ink based on silver nanoparticles (Fig. 1.6(h)).

All these 3D printed microwave components are meant to be used in a variety of wireless sensor networks (WSN) under IoT umbrella, which promise to reduce manufacturing costs and increase the efficiency of the devices while enabling all objects with identification, communication and sensing capabilities.

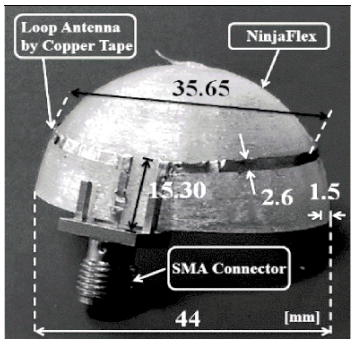

(a) *Image taken from* [23]

(b) *Image taken from* [24]

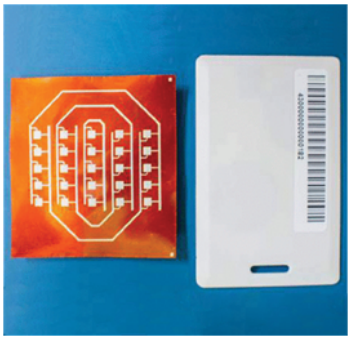

(c) *Image taken from* [25]

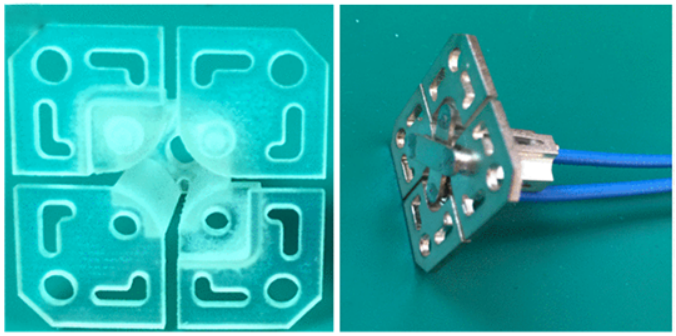

(d) *Images taken from* [26]

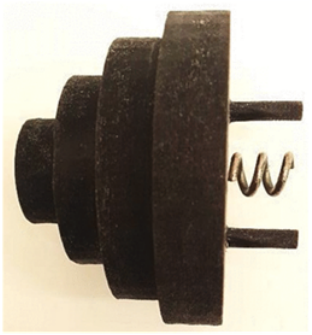

(e) *Image taken from* [27]

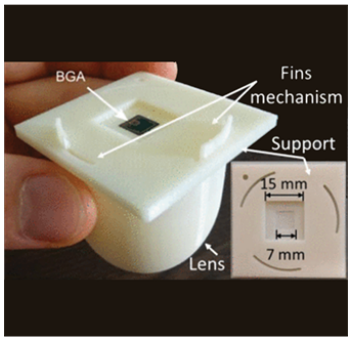

(f) *Image taken from* [28]

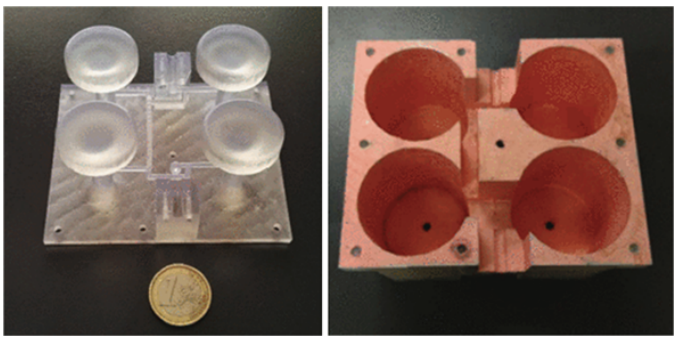

(g) *Images taken from* [29]

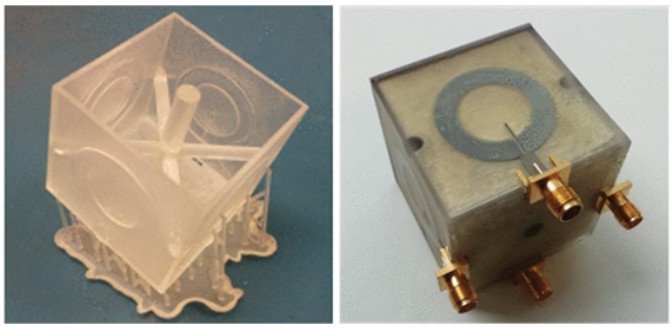

(h) *Images taken from* [30]

Figure 1.6: Some of the most relevant results reported in last five years literature, where 3D-printing techniques are used to fabricate microwave devices.

1.2 Microfluidics

3D-printed microwave sensing represents the first feature shared by the devices discussed in this doctoral thesis. The other one consists in the fact that they all manipulate small amounts of fluids. For this reason they are called *Microfluidic Sensors*.

1.2.1 A Brief History

The history of microfluidics [31],[32] dates back to the 1950s, when the first inkjet printer was patented by Siemens-Elema. The mechanism behind these printers is based on microfluidics, because it involves the use of very small tubes carrying the ink for printing.

In the mid-1970s Stephen Terry, from Stanford university, produced a miniaturized gas chromatograph integrated on a silicon wafer [33]. The system consisted essentially of an injection valve and a capillary, which were fabricated, through micromachining technique, onto a substrate silicon wafer. The application of IC processing techniques permitted to reduce the size of the sensor, passing from bulky laboratory instruments to a pocket-size package. This device was one of the first examples of "Laboratory-on-a-Chip" (LoC).

However, it was only at the beginning of the 1990s that LoC research really started to grow. In 1990, Andreas Manz, a Swiss chemist, published a paper in which he introduced the concept of miniaturized "Total chemical Analysis System" (μTAS), i.e., a microfluidic device capable of transforming chemical information into electronic information (Fig. 1.7) [34]. With μTAS it was possible to get a faster and more efficient sample separation (chromatographic or electrophoretic) as well as a reduced consumption of reagents, if compared to conventional analysis systems.

In 1993, Manz research group used micromachining technology to prepare chemical analysis systems that allowed capillary electrophoresis-based separations of amino acids [35].

In 1998, Whitesides group at Harvard university introduced fast and low-cost microfluidics prototyping, by using poly(dimethylsiloxane) (PDMS) [36]. Fig. 1.8 shows fluidic channels obtained in PDMS.

At the beginning of the 2000s, microfluidic cell biochips started to develop, as methods to miniaturize the body, investigating inter-organ connections and metabolism. In [37] an alternative model to *in vivo* evaluation of the chronic/acute toxicity of a substance is presented. Thanks to a microfluidic biochip, in fact, cellular

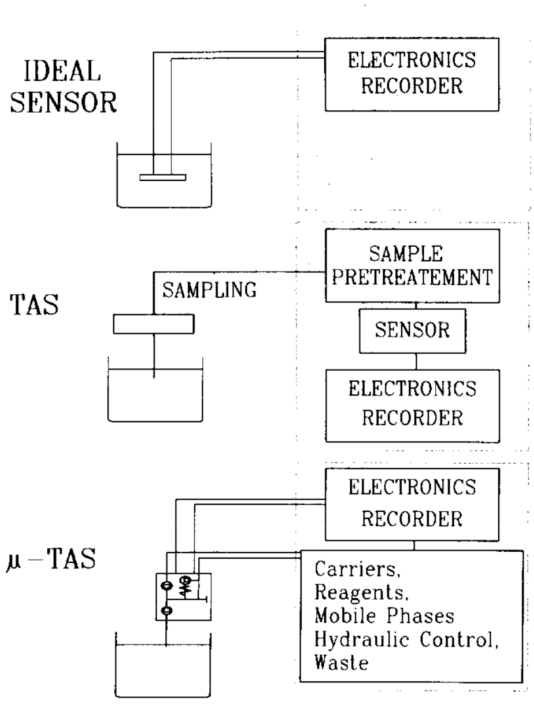

Figure 1.7: Schematic diagram of an ideal chemical sensor, a TAS and a miniaturized μTAS, as described by Manz in [34].

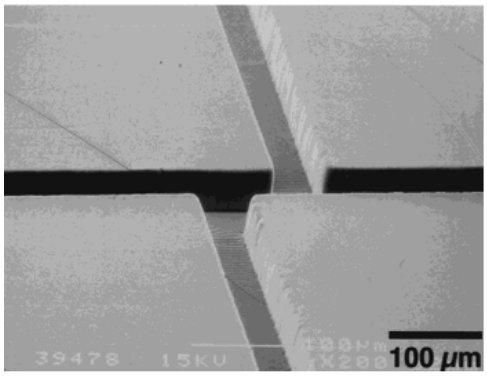

Figure 1.8: Scanning electron micrographs of the PDMS microfluidic channels created by Whitesides group [36].

function can be preserved, *in vitro*, over a long period of time.

In the last ten years, the organ-on-chip technology has evolved rapidly, thanks especially to the development of 3D-printing processes. For example, in [38], 3D-bioprinting is used to realize hydrogel scaffolds that, seeded by cardiomyocytes, creates endothelialized-myocardial-tissue. The organoid is then embedded into a microfluidic perfusion bioreactor, creating a complete endothelialized-myocardium-on-a-chip platform (Fig. 1.9), that is used for cardiovascular toxicity evaluation.

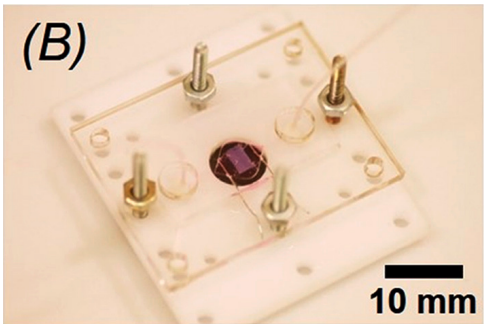

Figure 1.9: The "Heart-on-a-chip", presented in [38].

With AM techniques, a complex microfluidic environment, reproducing *in vivo* structures, can be easily mimicked in a fast and low-cost way. There are still some aspects that need to be investigated, such as vascularization and innervation, that are needed to guarantee longevity and functionality to the printed architectures. Once these issues will be addressed, *in vitro* constructed tissues will finally be perfusable, significally promoting tissue engineering and regenerative medicine.

1.2.2 Microfluidics and Microwaves: State of the Art

The microfluidics we know today are very small platforms, which give the possibility to scale and parallelize, on a single chip, sophisticated bio-chemical experiments. In the last decade, they have become widely used also for RF and microwave components [39]. In particular, they turned out to be very useful in biosensors for relative permittivity evaluation:

- In [40] a high frequency biosensor, constituted by a coplanar waveguide (CPW) and a microfluidic channel on top, was developed to make broadband measurements of the relative permittivity of human vein cells (Fig. 1.10(a)).
- In [41] a sensor based on an interdigitated capacitor and a microfluidic channel placed on top was used as accurate liquid sensing technique, from 40 MHz to 40 GHz (Fig. 1.10(b)).
- In [42] a coaxial resonator is used to quantify liquids' dielectric and magnetic properties using an optimized perturbation method. As shown in Fig. 1.10(c), the microfluidic capillary passes through the center of the resonator and the sample, depending on which TEM mode is interrogated, occupies the position of maximum electric or magnetic field.
- In [43] a coplanar resonator, with a PDMS microfluidic channel, allows to measure aqueous solutions with permittivity over a range from 20 to 40.
- In [44] and [45], split-ring resonators are used, along with microfluidics, as sensing

platform for the extraction of liquids complex permittivity. While in the first case a low-loss but bulky metallic resonant cavity is used to embed the SRR and the microfluidic (Fig. 1.10(e), in the second one microstrips are used, creating a compact and planar structure (Fig. 1.10(f)).

- In [46] a miniaturized transmission line is used to characterize samples of aqueous salt and protein solutions between 850 MHz and 40 GHz (Fig. 1.10(g)).
- In [47] a flexible sensing platform is realized by combining inkjet printing and soft lithography. It consists of a dual-spiral-shaped slot resonator with a microfluidic channel placed on top and embedded in the two ground planes of a CPW (Fig. 1.10(h)).
- In [48] a dual mode microstrip resonator, with a capillary inserted within the dielectric at the microstrip's end, is used to perform dielectric measurements (Fig. 1.10(i)). In order to avoid any possible temperature-variation in the sample permittivity, the resonator is enclosed inside an aluminum rectangular cavity, which can be used to monitor the ambient temperature changes. A similar device is presented in [49], where half-wave microstrip resonators sensor is packaged inside an aluminum rectangular cavity (Fig. 1.10(j)).
- In [50] and [51] CPW transmission lines are used in conjunction with microfluidic channels to extract dielectric permittivity of samples. In the former device (Fig. 1.10(k)), dielectric spectroscopy characterization is done between 300 kHz to 50 GHz, while, in the latter (Fig. 1.10(l)), are presented closed-form formulas to characterize liquids without using reference liquids or other calibration standards.
- In [52] a very high-sensitivity sensor, consisting in a microstrip line loaded with a shunt-connected series LC resonator, is presented (Fig. 1.10(m)). Here the microfluidic channel is positioned in the capacitive gap area of the sensor, modifying the capacitance value and thus the resonance frequency.

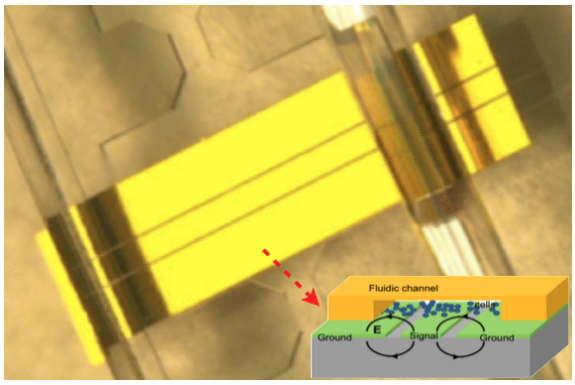

(a) *Image taken from* [40]

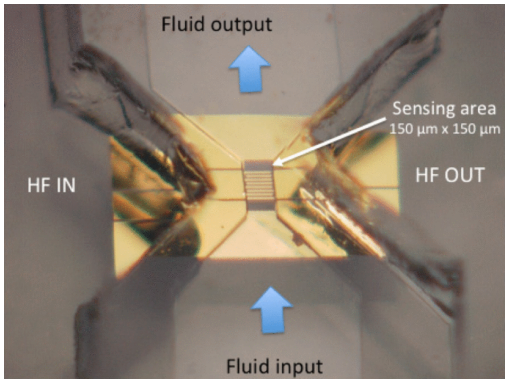

(b) *Image takenn from* [41]

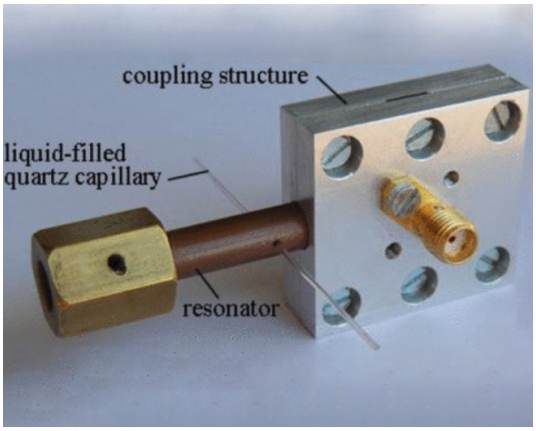

(c) *Image taken from* [42]

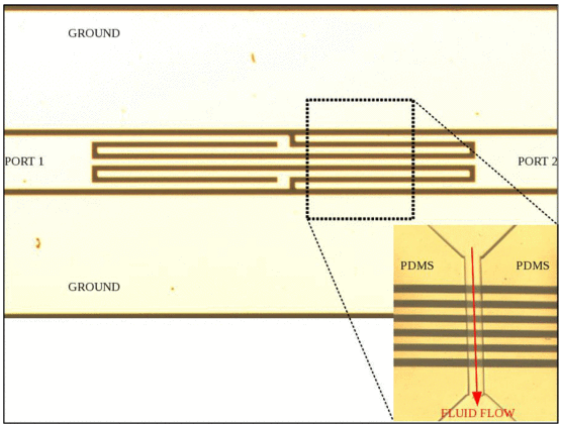

(d) *Image taken from* [43]

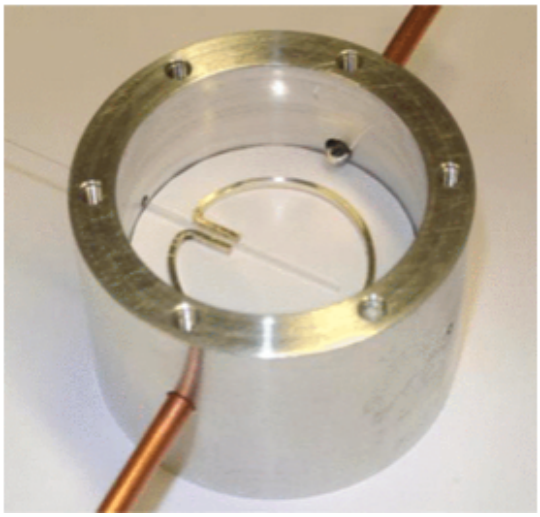

(e) *Image taken from* [44]

(f) *Image taken from* [45]

Figure 1.10: Some of the most relevant results reported in last ten years literature, where microfluidics are used in microwave devices (continued on next page).

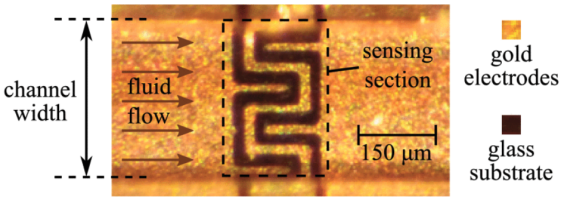

(g) *Image taken from* [46]

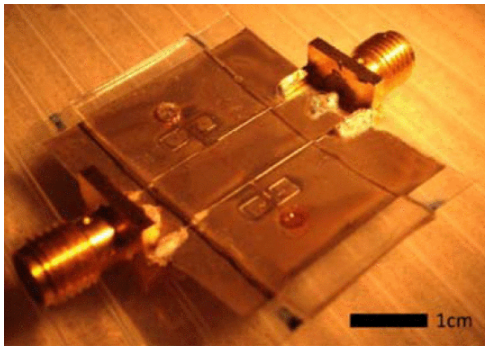

(h) *Image taken from* [47]

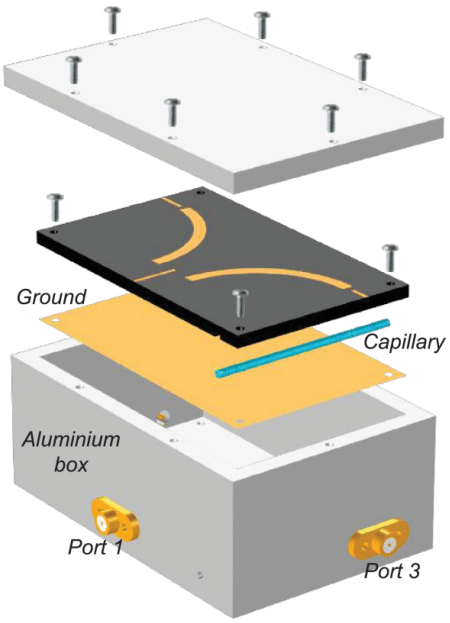

(i) *Image taken from* [48]

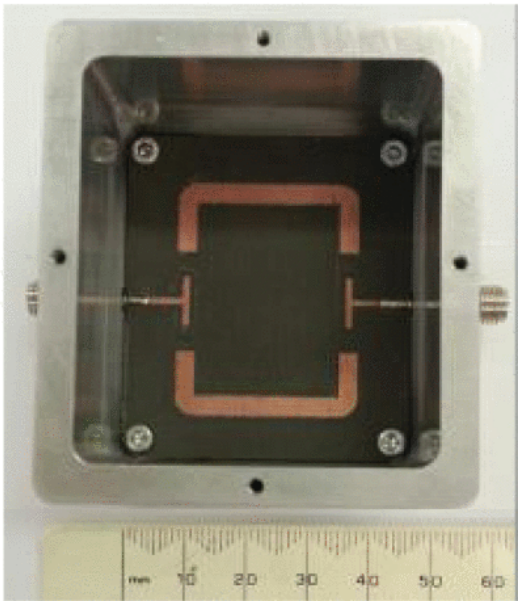

(j) *Image taken from* [49]

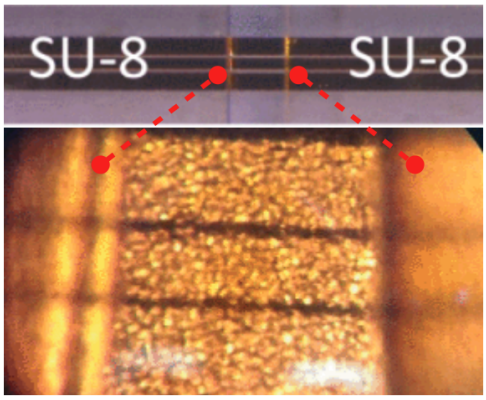

(k) *Image taken from* [50]

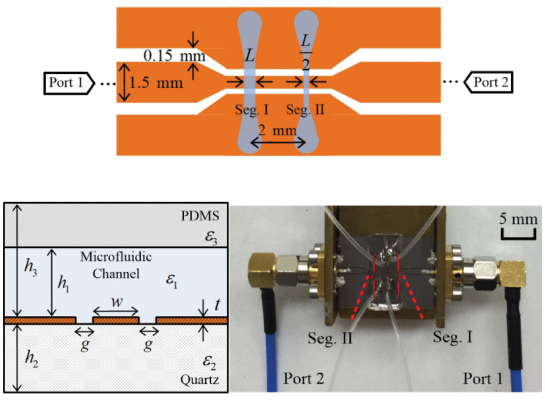

(l) *Images taken from* [51]

Figure 1.10: Some of the most relevant results reported in last ten years literature, where microfluidics are used in microwave devices (continued on next page).

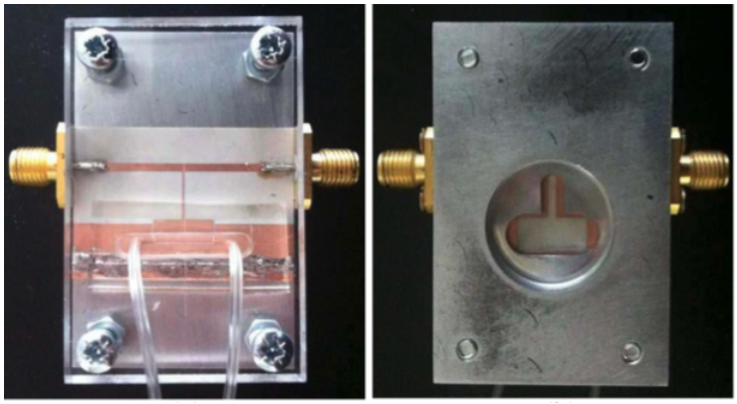

(m) *Images taken from* [52]

Figure 1.10: Some of the most relevant results reported in last ten years literature, where microfluidics are used in microwave devices.

1.3 Motivation and Objectives

1.3.1 Motivation

Additive manufacturing technology has experienced, in last years, a significant growth and almost any area of the market had invested on it, intrigued by its potentiality. In fact, while early use of AM focused just on rapid prototyping, nowadays AM is used for the rapid manufacturing of end-use products in aircraft, automobiles, biomedicine, space, construction, art and even jewellery fields. This same attractiveness led the scientists to apply it in their research. In particular, microwave engineers used 3D-printing to build many different components, as described with the state of the art in section subsection 1.1.4.

On the other hand, microfluidics, whose historical development has been presented in subsection 1.2.1, made a plenty of applications possible, in particular in biomedical fields. These devices are particularly suited for liquids' characterization, as highlighted with the state of the art in subsection 1.2.2.

The motivation for this PhD thesis is to bring together these two technologies, merging their benefits and exploiting them in the realization of tailored-shaped devices which present low-costs for medium productions and great versatility of printable materials. In particular, we want to perform the basic research which is needed to design and develop 3D-printed microfluidic devices for the characterization of liquids. These devices have to be cheap and easy to fabricate, so that any laboratory with a 3D-printer can create its own device, tailoring shape and dimensions to the type of application.

1.3.2 Objectives

Based on the presented motivation, and on the analysis of the SoA done in subsection 1.1.4 and subsection 1.2.2, the **following objectives** were set for our work:

I. The investigation of new materials to be used in the development of 3D-printed resonators, and their characterization in the frequency band of interest, as well as the investigation of new metallization techniques to be applied in components with complex shapes.

II. The development of 3D-printed resonant cavities with an embedded pipe which makes them suitable devices for dielectric characterization of liquids.

III. LUTs complex permittivity extraction through the use of the developed 3D-printed microfluidic cavities.

IV. The development of an oscillator which presents the 3D-printed cavity as the resonating part. The realization of such an oscillator would represent a first step in the creation of a handheld and self-sustained device for the characterization of liquids.

The ***first objective*** regards the characterization of 3D-printed materials chosen to be used for our devices. The determination of the type of material depends, obviously, on the printer employed which, in turn, is connected to the fact that the devices we want to fabricate have to be very low cost but also manufactured with a discrete accuracy. Part of this objective is also the research for metallization techniques to be adopted in devices with arbitrarily complex topologies.

The ***second objective*** deals with the developing, with AM techniques, of microfluidic cavity resonators for the characterization of liquids. The reason why cavity resonators have been chosen among other methods for the extraction of electromagnetic properties is that they are easier to metallize and guarantee more accurate measurements. Starting from the simpler shape (standard rectangular cavity) we want to develop a more complex one (spherical shaped cavity).

The ***third objective*** consists in the elaboration of an accurate algorithm to extract dielectric permittivity and loss tangent of a liquid under test, by looking at the frequency response of the microfluidic cavity. In particular:

- A method to extract the loss tangent of the LUT from the measured cavity Q-factor has to be found. This method should, preferably, de-embed the losses of the 3D-printed substrate, which are always quite high and thus, if not well-evaluated a priori, could jeopardize the estimation of the LUTs loss tangent.

- Since the resonance frequency of a cavity depends on the complex permittivity of the material constituting it, we want to find the relation between the complex permittivity of the LUT injected in the pipe inside the cavity and the cavity resonance frequency.

The ***fourth objective*** tackles the development of a microwave oscillator which, taking advantage of the realized 3D-printed resonant cavities, allows to estimate the liquids dielectric constant. In particular, based on the negative resistance concept, the oscillator realized will allow to extract information about the dielectric permittivity of the LUT by looking at the frequency of the system output.

1.4 Thesis Outline

The thesis is structured in the following way.

Chapter 2 summarizes the theory to conduct research on 3D-printed microfluidic sensor in microwave field. First of all, resonant cavities theory is reported, as fundamental topic used to develop the described sensor based on cavity resonators. Then, SIW technology is introduced, as method to metalize one of the sensors described. Afterwards, a classification of the different AM technologies is done, and special emphasis is applied to Fused Deposition Modeling and Stereolithography, which represent the techniques adopted to fabricate the devices object of this thesis. Since 3D-printed materials are not conceived for the use in microwave field, the evaluation of their electromagnetic characteristics is mandatory. For this reason, the techniques used to characterize the materials used to fabricate the sensors are eventually described. *This Chapter presents results for the objective I.*

Chapter 3 is devoted to square 3D-printed microfluidic cavities. The purpose of this kind of cavities is to determine liquids' electromagnetic properties - i.e., the dielectric permittivity and the loss tangent - by manipulating small amount of LUTs. In this thesis, microfluidic devices are based on cavity resonators, and present an embedded pipe where the LUT can be injected and characterized. The design of two rectangular resonant cavities is reported, followed by prototype fabrication description. Eventually, measurements results are presented, along with the algorithm developed to retrieve LUTs characteristics. *This Chapter presents results for objectives II and III.*

In **Chapter 4** a novel platform for the extraction of LUT dielectric properties is described. It consists of an oscillator based on the 3D-printed microfluidic cavity, i.e., whose resonating part is constituted by the 3D-printed sensor described in Chapter 3.

The oscillator represents the first step in realizing a complete low-cost and self-sustained system for the detection of the electromagnetic properties of liquids. The developed platform presents many amazing benefits, like low-cost, simplicity of calibration, design flexibility and the easy scalability. *This Chapter presents results for the objective IV.*

In **Chapter 5** a novel design of microfluidic resonant cavity is presented. This sensor consists in a pumpkin shaped cavity, i.e., a sphere slightly squeezed at the poles, with a pipe passing straight from the axis of symmetry. Different measurements were performed, with water, isopropanol and mixtures of them. Thanks to the spherical shape and to electroplating, which allowed to obtain the metallization of the structure in the inside, the quality factor of the cavity significantly increased with respect to the square sensor. Moreover, good performance in term of liquid characterization have been obtained, especially for the extracted value of loss tangent. *This Chapter presents further results for objectives II and III.*

Chapter 6 presents conclusions and future perspectives, based on the achieved results.

Concept Map

In order to keep the focus of the reader on the final aim of this research, i.e., the development of a 3D-printed self-sustained device for liquids characterization, a concept map is reported below, which could help in summarizing the work done during the PhD. Looking at this map, the reader get, at the first glance, the main aspects and parameters one has to consider along the path of developing 3D-printed self-sustained devices for LUTs characterization.

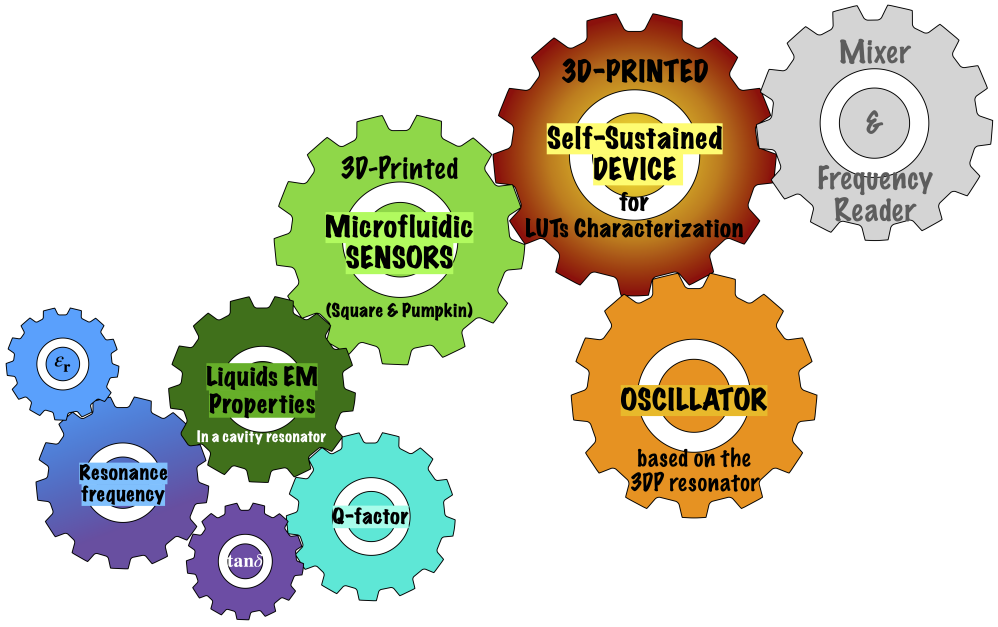

References

[1] M. Bozzi, E. Massoni, G. M. Rocco, C. Tomassoni, and L. Perregrini, "New Materials and Fabrication Technologies for Substrate Integrated Waveguide (SIW) Components," *Progress In Electromagnetics Research Symposium (PIERS 2017)*, Singapore, Singapore, 19-22 Nov. 2017 (invited paper).

[2] M. Bozzi, S. Moscato, L. Silvestri, E. Massoni, N. Delmonte, G.M. Rocco, M. Pasian, L. Perregrini, and C. Tomassoni, "Novel Materials and Fabrication Technologies for SIW Components for the Internet of Things," *2016 IEEE International Workshop on Electromagnetics: Applications (iWEM2016)*, Nanjing, China, May 16-18, 2016 (invited paper).

[3] S. Kulkarni, 2018, *3D Printing: The Next Big Thing in the Internet of Things*, RFID Journal, `https://www.rfidjournal.com/articles/view?18112`, accessed 30 August 2019.

[4] S. A. Nauroze *et al.*, "Additively Manufactured RF Components and Modules: Toward Empowering the Birth of Cost-Efficient Dense and Ubiquitous IoT Implementations," *Proceedings of the IEEE*, vol. 105, no. 4, pp. 702-722, April 2017.

[5] J. G. D. Hester, J. Kimionis, and M. M. Tentzeris, "Printed Motes for IoT Wireless Networks: State of the Art, Challenges, and Outlooks," *IEEE Transactions on Microwave Theory and Techniques*, vol. 65, no. 5, pp. 1819-1830, May 2017.

[6] A. Costanzo, D. Masotti, M. Fantuzzi, and M. Del Prete, "Co-Design Strategies for Energy-Efficient UWB and UHF Wireless Systems," *IEEE Transactions on Microwave Theory and Techniques*, vol. 65, no. 5, pp. 1852-1863, May 2017.

[7] J. Zhang, P. V. Orlik, Z. Sahinoglu, A. F. Molisch, and P. Kinney, "UWB Systems for Wireless Sensor Networks," *Proceedings of the IEEE*, vol. 97, no. 2, pp. 313-331, Feb. 2009.

[8] V. Kopta and C. C. Enz, "A 4-GHz Low-Power, Multi-User Approximate Zero-IF FM-UWB Transceiver for IoT," *IEEE Journal of Solid-State Circuits*, vol. 54, no. 9, pp. 2462-2474, Sept. 2019.

[9] C. Moore, 2018, *History of Additive Manufacturing Through the Years*, https://www.wazp.io/2018/07/25/history-of-additive-manufacturing-through-the-years/, accessed 3 September 2019.

[10] D. Goldberg, 2018, *History of 3D Printing: It's Older Than You Are (that is, if You're Under 30)*, https://www.autodesk.com/redshift/history-of-3d-printing/, accessed 3 September 2019.

[11] United States Patent, *Apparatus for Production of Three-Dimensional Objects by Stereolithography*, https://patentimages.storage.googleapis.com/5c/a0/27/e49642dab99cf6/US4575330.pdf, accessed 3 September 2019.

[12] P. Belton, 2018, *A new bladder made from my cells gave me my life back*, BBC,https://www.bbc.com/news/business-45470799, accessed 3 September 2019.

[13] E. Dixon, 2019, *Shanghai opens world's longest 3D-printed concrete bridge*, CNN, https://edition.cnn.com/style/article/shanghai-3d-printed-bridge-scli-intl/index.html, accessed 3 September 2019.

[14] AM Research Group - LoughBorough University, *About Additive Manufacturing*, https://www.lboro.ac.uk/research/amrg/about/whatisam/, accessed 4 September 2019.

[15] Global Electronic Services Inc., *What Are the Pros and Cons of Additive Manufacturing?*, https://gesrepair.com/what-are-the-pros-and-cons-of-additive-manufacturing/, accessed 25 January 2020.

[16] American Composites Manufacturers Association, *Pros and Cons of Additive Manufacturing*, http://compositesmanufacturingmagazine.com/2014/10/pros-cons-additive-manufacturing/2/, accessed 25 January 2020.

[17] *NATO exhibition features 60 years of scientific innovation*, 2018, https://www.nato.int/cps/en/natohq/news_161014.htm, accessed 8 September 2019.

[18] *3D Printer Headed to Space Station*, NASA, 2014, https://www.nasa.gov/content/3d-printer-headed-to-space-station, accessed 9 Sept. 2019.

[19] *Una stampante 3D a bordo della stazione orbitante*, Corriere della Sera, 2014, http://corriereinnovazione.corriere.it/tech/2014/21-novembre-2014/stampante-3d-bordo-stazione-orbitante-230584475104.shtml?refresh_ce-cp, accessed 9 Sept. 2019.

[20] *Europe's 3D Printer Set for Space Station*, 2014, ESA, https://www.esa.int/Our_Activities/Space_Engineering_Technology/Europe_s_3D_printer_set_for_Space_Station, accessed 9 Sept. 2019.

[21] *Portable On Board Printer 3D*, NASA, https://www.nasa.gov/mission_pages/station/research/experiments/explorer/Investigation.html?#id=1560, accessed 9 Sept. 2019.

[22] J. Bito *et al.*, "A Novel Solar and Electromagnetic Energy Harvesting System With a 3-D Printed Package for Energy Efficient Internet-of-Things Wireless Sensors," *IEEE Transactions on Microwave Theory and Techniques*, vol. 65, no. 5, pp. 1831-1842, May 2017.

[23] K. Nate and M. M. Tentzeris, "A novel 3-D printed loop antenna using flexible NinjaFlex material for wearable and IoT applications," *2015 IEEE 24th Electrical Performance of Electronic Packaging and Systems (EPEPS)*, San Jose, CA, 2015, pp. 171-174.

[24] S. Y. Wu, C. Yang, W. Hsu, and L. Lin, 2015, "3D-printed microelectronics for integrated circuitry and passive wireless sensors," *Microsystems & Nanoengineering*, https://www.nature.com/articles/micronano201513/, accessed 7 September 2019.

[25] J. G. D. Hester and M. M. Tentzeris, "Inkjet-Printed Flexible mm-Wave Van-Atta Reflectarrays: A Solution for Ultralong-Range Dense Multitag and Multisensing Chipless RFID Implementations for IoT Smart Skins," *IEEE Transactions on Microwave Theory and Techniques*, vol. 64, no. 12, pp. 4763-4773, Dec. 2016.

[26] Y. Li, C. Wang, H. Yuan, N. Liu, H. Zhao, and X. Li, "A 5G MIMO Antenna Manufactured by 3-D Printing Method," *IEEE Antennas and Wireless Propagation Letters*, vol. 16, pp. 657-660, 2017.

[27] M. F. Farooqui and A. Shamim, "3-D Inkjet-Printed Helical Antenna with Integrated Lens," *IEEE Antennas and Wireless Propagation Letters*, vol. 16, pp. 800-803, 2017.

[28] A. Bisognin *et al.*, "Ball Grid Array Module With Integrated Shaped Lens for 5G Backhaul/Fronthaul Communications in F-Band," *IEEE Transactions on Antennas and Propagation*, vol. 65, no. 12, pp. 6380-6394, Dec. 2017.

[29] C. Tomassoni, G. Venanzoni, M. Dionigi and R. Sorrentino, "Compact Quasi-Elliptic Filters With Mushroom-Shaped Resonators Manufactured With 3-D Printer," *IEEE Transactions on Microwave Theory and Techniques*, vol. 66, no. 8, pp. 3579-3588, Aug. 2018.

[30] V. Palazzi *et al.*, "3-D-Printing-Based Selective-Ink-Deposition Technique Enabling Complex Antenna and RF Structures for 5G Applications up to 6 GHz," *IEEE Transactions on Components, Packaging and Manufacturing Technology*, vol. 9, no. 7, pp. 1434-1447, July 2019.

[31] G. M. Whitesides, "The origins and the future of microfluidics," *Nature*, vol. 442, no. 7101, pp. 368-373, July 2006.

[32] *What is the History of Microfluidics?*, Fluigent, `https://www.fluigent.com/microfluidic-expertise/what-is-microfluidic/history-of-microfluidics/`, accessed 10 September.

[33] S. C. Terry, J. H. Jerman, and J. B. Angell, "A gas chromatographic air analyzer fabricated on a silicon wafer," *IEEE Transactions on Electron Devices*, vol. 26, no. 12, pp. 1880-1886, Dec. 1979.

[34] A. Manz, N. Graber, and H. M Widmer, "Miniaturized total chemical analysis systems: a novel concept for chemical sensing," *Sensors actuators B Chem.*, vol. 1, no. 1-6, pp. 244-248, 1990.

[35] D. J. Harrison, K. Fluri, K. Seiler, Z. Fan, C. S. Effenhauser, and A. Manz, "Micromachining a miniaturized capillary electrophoresis-based chemical analysis system on a chip," *Science*, vol. 261, no. 5123, pp. 895-897, 1993.

[36] D. C. Duffy, J. C. McDonald, O. J. A. Schueller, and G. M. Whitesides, "Rapid prototyping of microfluidic systems in poly (dimethylsiloxane)," *Analytic Chemistry*, vol. 70, no. 23, pp. 4974-4984, 1998.

[37] R. Baudoin, A. Corlu, L. Griscom, C. Legallais, and E. Leclerc, "Trends in the development of microfluidic cell biochips for in vitro hepatotoxicity," *Toxicology in Vitro*, vol. 21, issue 4, pp. 535-544, 2007.

[38] Y. S. Zhang *et al.*, "Bioprinting 3D microfibrous scaffolds for engineering endothelialized myocardium and heart-on-a-chip," *Biomaterials*, vol. 110, pp. 45-59, 2016.

[39] T. Lin, W. Su, and M. M. Tentzeris, "Expand Horizons of Microfluidic Systems: An Inkjet Printed Flexible Energy Autonomous Micropump System for Wearable and IoT Microfluidic Applications," 2018 IEEE/MTT-S International Microwave Symposium - IMS, Philadelphia, PA, 2018, pp. 812-815.

[40] K. Grenier *et al.*, "Integrated Broadband Microwave and Microfluidic Sensor Dedicated to Bioengineering," *IEEE Transactions on Microwave Theory and Techniques*, vol. 57, no. 12, pp. 3246-3253, Dec. 2009.

[41] T. Chen, D. Dubuc, M. Poupot, J. Fournie, and K. Grenier, "Accurate Nanoliter Liquid Characterization Up to 40 GHz for Biomedical Applications: Toward Noninvasive Living Cells Monitoring," *IEEE Transactions on Microwave Theory and Techniques*, vol. 60, no. 12, pp. 4171-4177, Dec. 2012.

[42] D. J. Rowe, A. Porch, D. A. Barrow, and C. J. Allender, "Microfluidic Microwave Sensor for Simultaneous Dielectric and Magnetic Characterization," *IEEE Transactions on Microwave Theory and Techniques*, vol. 61, no. 1, pp. 234-243, Jan. 2013.

[43] T. Chretiennot, D. Dubuc, and K. Grenier, "A Microwave and Microfluidic Planar Resonator for Efficient and Accurate Complex Permittivity Characterization of Aqueous Solutions," *IEEE Transactions on Microwave Theory and Techniques*, vol. 61, no. 2, pp. 972-978, Feb. 2013.

[44] D. J. Rowe *et al.*, "Improved Split-Ring Resonator for Microfluidic Sensing," *IEEE Transactions on Microwave Theory and Techniques*, vol. 62, no. 3, pp. 689-699, March 2014.

[45] A. A. Abduljabar, D. J. Rowe, A. Porch, and D. A. Barrow, "Novel Microwave Microfluidic Sensor Using a Microstrip Split-Ring Resonator," *IEEE Transactions on Microwave Theory and Techniques*, vol. 62, no. 3, pp. 679-688, March 2014.

[46] N. Meyne née Haase, G. Fuge, H. K. Trieu, A. Zeng, and A. F. Jacob, "Miniaturized Transmission-Line Sensor for Broadband Dielectric Characterization of Biological Liquids and Cell Suspensions," *IEEE Transactions on Microwave Theory and Techniques*, vol. 63, no. 10, pp. 3026-3033, Oct. 2015.

[47] W. Su, B. S. Cook, and M. M. Tentzeris, "Additively Manufactured Microfluidics-Based "Peel-and-Replace" RF Sensors for Wearable Applications," *IEEE Transactions on Microwave Theory and Techniques*, vol. 64, no. 6, pp. 1928-1936, June 2016.

[48] A. A. Abduljabar, N. Clark, J. Lees, and A. Porch, "Dual Mode Microwave Microfluidic Sensor for Temperature Variant Liquid Characterization," *IEEE Transactions on Microwave Theory and Techniques*, vol. 65, no. 7, pp. 2572-2582, July 2017.

[49] A. A. Abduljabar, H. Hamzah, and A. Porch, "Double Microstrip Microfluidic Sensor for Temperature Correction of Liquid Characterization," *IEEE Microwave and Wireless Components Letters*, vol. 28, no. 8, pp. 735-737, Aug. 2018.

[50] X. Bao *et al.*, "Broadband Dielectric Spectroscopy of Cell Cultures," *IEEE Transactions on Microwave Theory and Techniques*, vol. 66, no. 12, pp. 5750-5759, Dec. 2018.

[51] D. Ye, M. S. Islam, G. Yu, and P. Wang, "A Single-Line Single-Channel Method With Closed-Form Formulas for the Characterization of Dielectric Liquids," *IEEE Transactions on Microwave Theory and Techniques*, vol. 67, no. 6, pp. 2443-2450, June 2019.

[52] A. Ebrahimi, J. Scott, and K. Ghorbani, "Ultrahigh-Sensitivity Microwave Sensor for Microfluidic Complex Permittivity Measurement," *IEEE Transactions on Microwave Theory and Techniques*, Early Access.

Chapter 2

Introduction to Technology

This chapter introduces the most relevant concepts regarding the technologies adopted for the implementation of the devices presented in next chapters. In particular, section 2.1 is devoted to resonant cavities, which represent the basic structure for the microfluidic sensors described in following chapters. Then, Substrate Integrated Waveguide (SIW) technology is described in section 2.2, as it represents the approach used to implement the metallization of the microfluidic cavities described in Chapter 3. Section 2.3 presents AM technologies, with particular focus on the two technologies used to print the objects described later in this thesis. Eventually, the techniques used to characterize, in the microwave range of frequencies, the 3D-printed substrates, are depicted in section 2.4.

2.1 Resonant Cavities

A resonator is an element capable of storing frequency-dependent electric and magnetic energy [1], [2], [3].

Let's consider any volume of space V which is capable of exchanging energy with the outside just through a transmission line (or through a couple of terminals, in case we are considering lumped circuits). Let's apply the Poynting theorem to V:

$$P_{in} = P_d + 2j\omega(W_m - W_e) \tag{2.1}$$

where P_{in} is the complex power flowing into the circuit, P_d is the (real) power dissipated through Joule effect, W_m and W_e are, respectively, the average magnetic and electric energies stored in V over a period.

By expressing the input power in terms of voltage and current $P_{in} = VI^*/2$ and

by introducing the input impedance $Z_{in} = V/I$, a definition of impedance in terms of energies can be retrieved from (2.1) as:

$$Z_{in} = \frac{P_d + 2j\omega(W_m - W_e)}{II^*/2} \tag{2.2}$$

Eq. (2.2) shows that the input impedance of V is purely real if when the following condition is true:

$$W_m = W_e \tag{2.3}$$

Eq. (2.3) represents the *resonance condition*. The resonant frequency of a resonator is thus the frequency at which the energy stored in electric field equals the energy stored in the magnetic field.

2.1.1 Resonance Frequency

In the most general case, a microwave resonator is constituted by any volume surrounded by a metallic surface. The field distribution (and hence the stored electric and magnetic energies) in this structure is affected by the shape of the structure itself.

As before, let's consider V, a volume of space enclosed by a perfect conductor and let's study how EM fields behave in it. From Maxwell's equations we know that:

$$\nabla \times \boldsymbol{H} = j\omega\varepsilon\boldsymbol{E} \tag{2.4}$$

$$\nabla \times \boldsymbol{E} = -j\omega\mu\boldsymbol{H} \tag{2.5}$$

Let's now substitute the curl of (2.5) into (2.4). The following equation is obtained:

$$\nabla \times \nabla \times \boldsymbol{E} - \omega^2\varepsilon\mu\boldsymbol{E} = 0 \tag{2.6}$$

where ε and μ are assumed constant in the volume V of the cavity.

Now, let's apply the boundary condition for $\boldsymbol{E}$:

$$\boldsymbol{n} \times \boldsymbol{E} = 0 \qquad (\text{on } S) \tag{2.7}$$

where $\boldsymbol{n}$ is the unit vector directed outwards normal to the volume surface S.

Equations (2.6) and (2.7) constitute an eigenvalue problem, whose solutions can exist only when $\omega^2\varepsilon\mu = k^2$ takes certain discrete values.

Let's consider a rectangular cavity with sides a, b and d, as shown in Fig. 2.1.

In this case, the eigenvalues are given by:

$$k_a{}^2 = \omega_a{}^2 \varepsilon\mu = (n\pi/a)^2 + (m\pi/b)^2 + (l\pi/d)^2 \tag{2.8}$$

where n, m and l are arbitrary integers including zero, provided two of them do not become zero simultaneously.

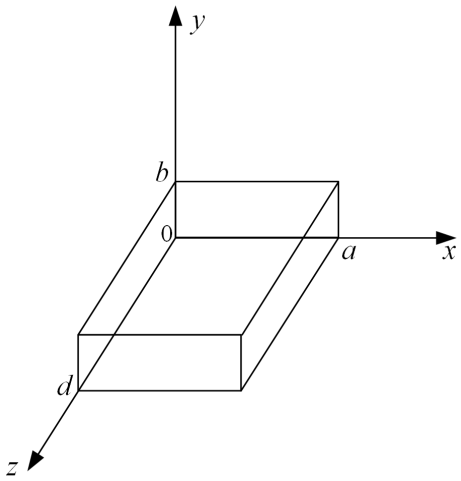

Figure 2.1: A rectangular cavity resonator.

Thus, a finite EM field existing in a space enclosed by a perfect conductor should have, at least, one of the discrete frequencies determined by $\omega_a = k_a\sqrt{\varepsilon\mu}$, where k_a's are the eigenvalues of (2.6) and (2.7).

Any microwave structure is capable to constitute a resonator, and its resonant frequencies are determined by its structure's physical characteristics and dimensions.

2.1.2 Quality Factor

When dealing with a resonator (or an oscillator), in order to describe the nature of the generated oscillations (whether they maintain their amplitude or they are damped over time) a dimensionless parameter is used, and it is called Quality Factor.

The quality factor (Q-factor) is defined as

$$\mathcal{Q} = \omega_0 \frac{W_T}{P_{loss}} \tag{2.9}$$

where ω_0 is the angular resonance frequency, W_T is the average EM energy stored in the cavity and P_{loss} is the total power dissipated in the cavity. In particular, W_T is the sum of the stored electric and magnetic energies, W_e and W_m, in the volume V:

$$W_T = W_e + W_m = \frac{\varepsilon}{4}\int_V \boldsymbol{E}\cdot\boldsymbol{E}^*\,dv + \frac{\mu}{4}\int_V \boldsymbol{H}\cdot\boldsymbol{H}^*\,dv \tag{2.10}$$

P_{loss}, instead, is the sum of the power dissipated on the conducting walls, P_c, and in the dielectric, P_d:

$$P_{loss} = P_c + P_d = \frac{R_s}{2}\int_S |\boldsymbol{H_t}|^2\,ds + \frac{\omega_0\varepsilon''}{2}\int_V \boldsymbol{E}\cdot\boldsymbol{E}^*\,dv \tag{2.11}$$

where S is the surface of the cavity, $\boldsymbol{H_t}$ is the tangential magnetic field at the surface, R_s represents the surface resistance of the conducting walls ($R_s = \sqrt{\omega\mu_0/2\sigma}$, with σ the conductivity of the metallic walls), and ε'' is the imaginary part of the permittivity.

Let's now call with $Q_c = \omega_0 W_T/P_c$ the Q-factor related to conductor losses and with $Q_d = \omega_0 W_T/P_d$ the one related to dielectric losses.

In view of (2.9), the total quality factor of the resonator, also called *unloaded* quality factor, can be written as:

$$\frac{1}{Q_U} = \frac{1}{Q_c} + \frac{1}{Q_d} \tag{2.12}$$

where, therefore, the overall Q_U can be obtained as harmonic mean of the two contributions.

In resonant circuits are always present dissipative elements, which give rise to unwanted losses inside the circuit. However, dissipative elements give rise also to losses in an *external circuit*, which absorbs power from the resonator. In order to take into account these extra losses, an external Q-factor, Q_e, is defined, which is related to this external load. By adding the contribution of the unloaded Q-factor of the resonator Q_U and the, just defined, contribution of the external circuit Q_e, we obtain Q_L, the *loaded* quality factor, as:

$$Q_L = \left(\frac{1}{Q_U} + \frac{1}{Q_e}\right)^{-1} \tag{2.13}$$

The calculation of the quality factor of a resonator is particularly useful, since it allows to estimate the loss tangent of the material inside the cavity. In the following section, the procedure to extract the unloaded quality factor of a resonator, starting from the measured S-parameters, is presented.

2.1.2.1 Extraction of the Q-factor from S_{11} Measurements

Let's consider a 1-port cavity resonator, which represents the case analyzed in this thesis. Once the S-parameters measurements have been completed, we can use the

measured reflection coefficient, S_{11}, to extract the quality factor, according to [2], [4].

By definition, the loaded quality factor can be calculated as

$$Q_L = \frac{f_0}{\Delta f} \tag{2.14}$$

where f_0 is the resonance frequency and Δf is the half-power bandwidth which, depending if we have reflection or transmission coefficient, can be determined in different ways. In particular, since the presented microfluidic sensor is a 1-port device, the half-power width is determined directly from the magnitude of the S_{11}. As shown in Fig. 2.2, the half-power width is calculated as $f_2 - f_1$, where f_1 and f_2 are the frequencies where the reflection coefficient is equal to

$$|S_{11}| = \sqrt{\frac{|S_{11}^{b}|^2 + |S_{11}^{min}|^2}{2}} = 10\log_{10}\left(\frac{10^{S_{11}^{b}/10} + 10^{S_{11}^{min}/10}}{2}\right) \text{ (dB)} \tag{2.15}$$

where $|S_{11}^{b}|$ (indicated in Fig. 2.2) is the base-line value of $|S_{11}|$ out of resonance, and $|S_{11}^{min}|$ is the $|S_{11}|$ value at the resonance frequency.

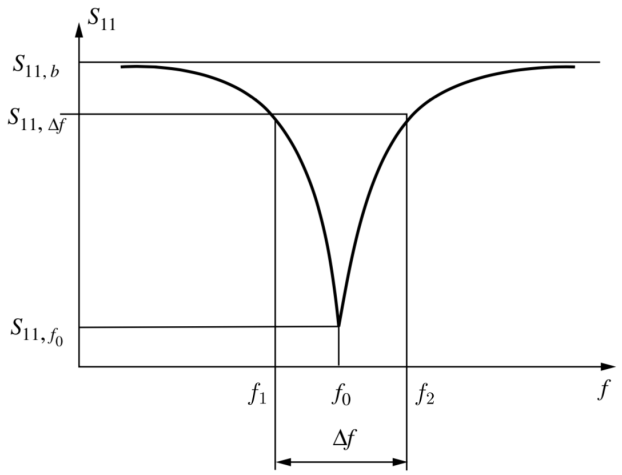

Figure 2.2: Illustrative representation of a possible $|S_{11}|$ plot, where the half-power bandwidth and the baseline are reported [4].

In order to retrieve the *unloaded* quality factor, one more element is needed, which is the coupling coefficient k. It is defined as

$$k = \frac{P_{\text{loss,ex}}}{P_{\text{loss,res}}} \tag{2.16}$$

where $P_{\text{loss,ex}}$ is the amount of power dissipated in the external circuit, and $P_{\text{loss,res}}$ is the power dissipated in the resonator. When $k > 1$ (the power dissipated in the external circuit is more than that dissipated in the resonator) we speak of *overcoupling*; when

$k < 1$ (the power dissipated in the external circuit is less than that dissipated in the resonator) we speak of *undercoupling*; when $k = 1$, the coupling is said to be *critical*.

The coupling coefficient can be determined by looking at the plot of the reflection coefficient on the Smith Chart. As shown in Fig. 2.3, if we call d is the diameter of the "resonant circle", the coupling coefficient can be expressed as

$$k = \frac{d}{2 - d} \tag{2.17}$$

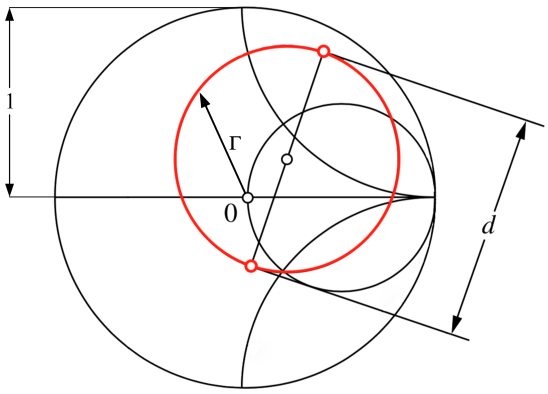

Figure 2.3: Plot of the reflection coefficient on the Smith chart.

Another way to determine k is to express it in terms of $|S_{11}^{min}|$ as follows:

$$k = \frac{1 - \left|S_{11}^{min}\right|}{1 + \left|S_{11}^{min}\right|}, \quad \text{in case of undercoupling} \tag{2.18a}$$

$$k = \frac{1 + \left|S_{11}^{min}\right|}{1 - \left|S_{11}^{min}\right|}, \quad \text{in case of overcoupling} \tag{2.18b}$$

Of course, in order to apply (2.18a) or (2.18b) the kind of coupling needs to be known *a priori* and, to determine that, a glance at the "resonant circle" on the Smith chart is usually enough. A small "resonant circle" indicates undercoupling ($k < 1$); a large "resonant circle" represents overcoupling ($k > 1$); otherwise, we have critical coupling. An example is reported in Fig. 2.4, where it is clear the difference between an undercoupled "resonant circle" (on the left) and an overcoupled one (on the right).

Finally, having retrieved Q_L and k, the unloaded quality factor of the resonator can be calculated as

$$Q_U = Q_L\,(1 + k) \tag{2.19}$$

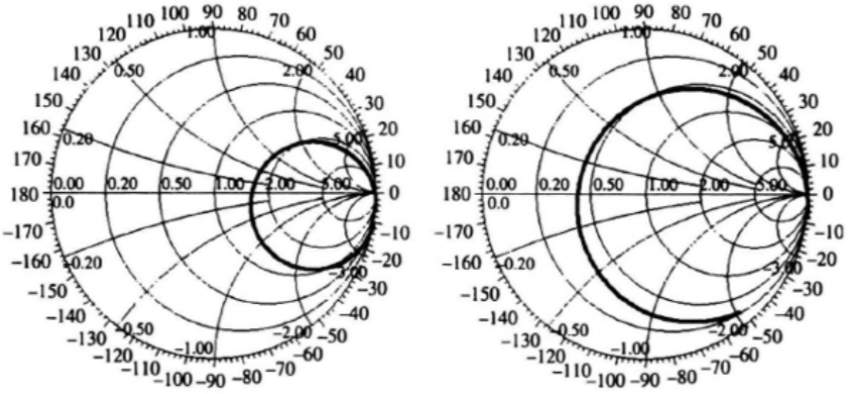

Figure 2.4: "Resonant circles" for two illustrative cases [2].

2.2 Substrate Integrated Waveguide Technology

Traditional transmission lines are of two types: microstrip line and rectangular waveguide. Microstrip lines are very compact and low cost, but, if we go to millimeter waves, there are problems like high losses, spurious radiation and coupling with adjacent circuits. Rectangular waveguides are completely shielded and have very low losses but, on the other hand, they are very expensive and bulky, and, if there is the necessity to integrate them with active components, proper transitions from the rectangular waveguide to the planar structure are needed. This increases the complexity of the system and also creates some problems of additional losses.

In order to have something that closes the technological gap between the planar structures and the rectangular waveguides, substrate integrated waveguide structures have been developed [5], [6]. SIW structures consist of a dielectric layer with top and bottom metallization and two rows of metal cylinders that connect the two parallel metal plates (Figure 2.5). With this technology it is thus possible to fabricate transmission lines which are like rectangular waveguides but in planar form.

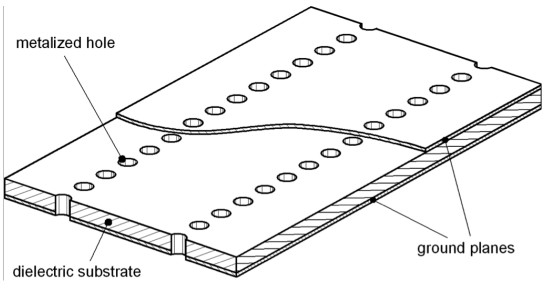

Figure 2.5: Example of Substrate Integrated Waveguide structure [6].

The modes of the SIW are very similar to the modes of the rectangular waveguides; we have *quasi*-TE_{10} mode (Fig. 2.6), *quasi*-TE_{20} mode and so on. In SIWs, however,

there are no TM modes, because this would imply having a longitudinal current flowing on the side walls, but in SIW we do not have continuous side walls.

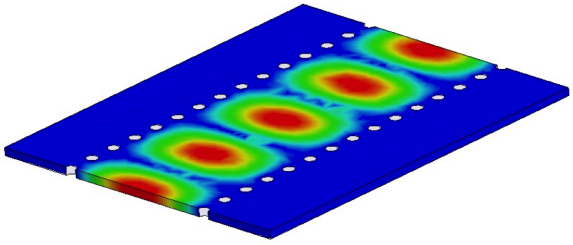

Figure 2.6: TE_{10} mode in a SIW interconnect. Only TE_{n0} modes (n=1, 2, ...) can be supported by SIW structures.

With SIWs, it is possible to implement any shape by simply replacing the solid metal side walls of the waveguide component with rows of metal cylinders, which can be located wherever it is necessary. This gives a lot of flexibility, making structures with elaborated shapes no more expensive than simpler shapes' structures.

As for the fabrication, the process starts with the perforation of the dielectric substrate by mechanical drilling or laser (with 3D-printing, instead, the holes are realized during the printing process itself) and then the holes are metallized. At the very beginning the metallization was done using rivets, then conductive paste or some electrochemical solution was preferred. This fabrication process, simpler with respect to traditional processes, is accessible to small and medium enterprises and permits low manufacturing costs.

2.2.1 Loss Mechanisms

In SIW structures, three sources of losses can be identified [7], [8]:

- Conductor losses, due to ohmic losses on top and bottom metal walls and in the rows of metal cylinders;
- Dielectric losses, due to the substrate material that we find inside the SIW structure;
- Radiation losses, when the distance between the metal cylinders is too large and so we have leakage through the gaps.

2.2.1.1 Conductor Losses

If we consider SIW with finite conductivity in the top, bottom and side walls, we can think, by exploiting the analogy between SIW and rectangular waveguide, to use for SIW the same attenuation constant formula as used for rectangular waveguide:

$$\alpha_c(f) = \frac{\sqrt{\pi f \varepsilon_0 \varepsilon_r}\,[1 + 2(f_c/f)^2\, h/w]}{h\,\sqrt{\sigma_c}\,\sqrt{1 - (f_c/f)^2}} \tag{2.20}$$

In this formula, f represents the operating frequency, f_c is the cutoff frequency, h is the thickness of the SIW and w is the width of the structure. However, in (2.20), attention must be paid on inserting the right width for the SIW structure. Indeed, while in rectangular waveguides w is equal to the width of the structure, in SIWs w represents an effective width, which is slightly less than the distance between the metal cylinders centers [9].

The thickness of the dielectric substrate h plays an important role: Figure 2.7 shows the different contributions to the attenuation constant versus h, while keeping all other geometrical dimensions at their nominal values. It results that increasing h determines a significant reduction in the conductor loss and no effect on the dielectric loss. Radiation loss is practically negligible in this case, and in general it is not affected by the substrate thickness.

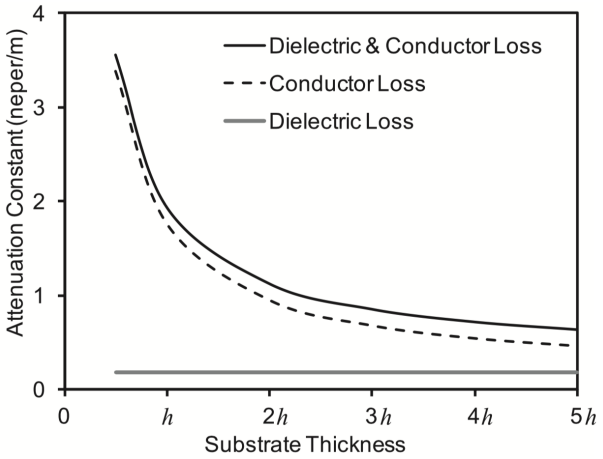

Figure 2.7: Attenuation constant α_c versus substrate thickness at $f = 1.5\ f_c$ [7].

The decreasing of α_c with the increasing in h has a straightforward explanation [10]. The conductor losses depend on the surface integral of $|\mathbf{J}|^2$ over the metal surface, where $\mathbf{J}$ represents the electric current density flowing on top and bottom metal layers and on the surface of the metal vias. When the substrate height is increased, $|\mathbf{J}|$ reduces proportionally to $\sqrt{h}$. On one hand, this brings the conductor loss on the top and bottom layers to scale as $1/h$. On the other hand, since the lateral surface of metal vias increases with h, this compensates the reduction of $|\mathbf{J}|^2$, leaving the contribution of the metal vias to conductor loss unchanged with h. The dielectric loss, instead, depends on the volume integral of $|\mathbf{E}|^2$, where $\mathbf{E}$ represents the electric field over the whole substrate volume. When the substrate height is increased, $|\mathbf{E}|$ reduces

proportionally to $\sqrt{h}$. However, the volume of the substrate increases with h, thus making the dielectric loss independent from any change in h.

2.2.1.2 Dielectric Losses

Also in the case of dielectric losses, the analogy with rectangular waveguide is exploited. They can be expressed as:

$$\alpha_D(f) = \frac{\pi f \sqrt{\varepsilon_r}}{c\sqrt{1-(f_c/f)^2}} \tan\delta \tag{2.21}$$

where f represents the operating frequency, f_c is the cutoff frequency, $\tan\delta$ is the loss tangent of the substrate and c is the light velocity in vacuum. Figure 2.8 shows, again, that the full-wave analysis fits very well with the plot obtained by (2.21).

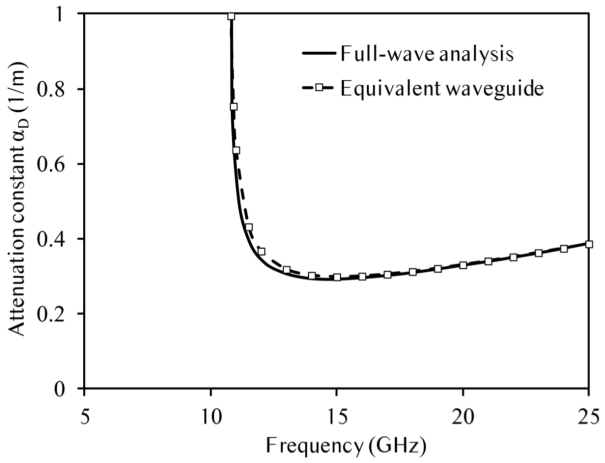

Figure 2.8: Attenuation constant α_D versus frequency for an SIW structure ($w = 10$ mm, $d = 1$ mm, $s = 2$ mm, $h = 1$ mm, $\varepsilon_r = 2.2$, $\tan\delta = 0.0009$) [8].

If we refer back to Fig.2.7 - which results from (2.21) - there is no dependence on the thickness h, meaning that the increase of the thickness does not have any impact on the dielectric losses. This is because dielectric losses depend on the volume integral of $|\mathbf{E}|^2$ (where $\mathbf{E}$ represents the electric field) over the whole volume of the substrate. If h is increased, $|\mathbf{E}|$ reduces proportionally to $\sqrt{h}$ but, also, the volume of the substrate linearly increases with h, making the dielectric loss independent of h.

Thus, there are two ways to decrease dielectric losses: either to use a better material or, as it was done for the devices described in this thesis, the structure has to be designed as empty as possible (this can be easily realised thanks to the flexibility of 3D-printing).

2.2.1.3 Radiation Losses

Radiation loss is due to the radiation leakage through the gaps between the metallized vias. In Fig. 2.9(a) radiation loss is plotted *vs* frequency. It can be noticed how radiation loss, large at the cutoff, decreases with frequency.

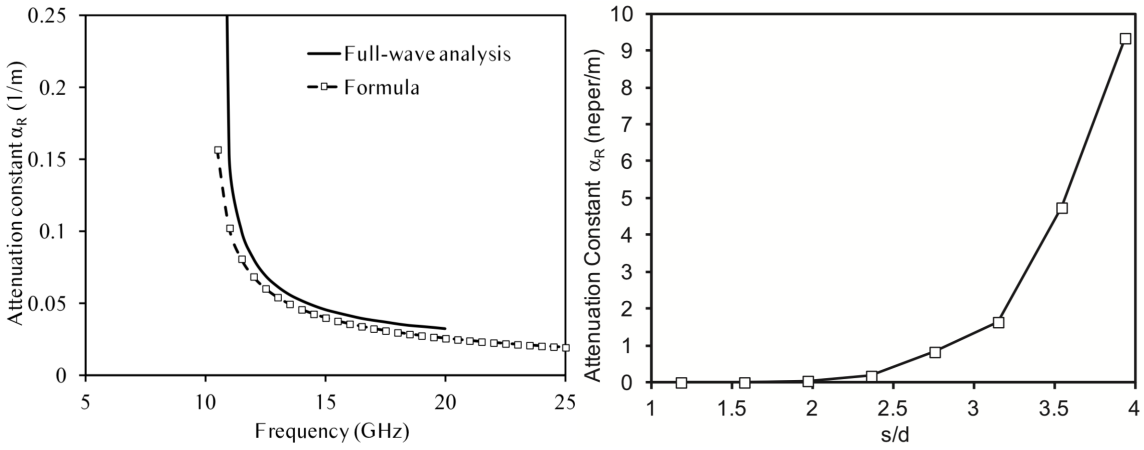

Figure 2.9: Attenuation constant α_R for an SIW structure with $w = 10$ mm, $d = 1$ mm, $h = 1$ mm, $\varepsilon_r = 2.2$: (a) Comparison between results obtained from full-wave analysis and from formula (2.22) [8]; (b) Attenuation constant versus the ratio s/d calculated at 15 GHz [6].

The following formula has been derived to calculate the attenuation due to radiation in SIW structures [11]:

$$\alpha_R = \frac{\frac{1}{w}\left(\frac{d}{w}\right)^{2.84}\left(\frac{s}{d}-1\right)^{6.28}}{4.85\sqrt{\left(\frac{2w}{\lambda}\right)^2-1}}\left[\frac{dB}{m}\right] \tag{2.22}$$

Figure 2.9(b), instead, reports the behaviour of the radiation loss while increasing the ratio s/d. It can be seen that α_R starts to increase for $s > 2d$.

2.2.2 SIW Design Rules

To conclude this section devoted to SIW technology, a set of design rules is presented, which allow to choose the geometrical dimensions of SIW structures [6]. These rules ensure that minimum radiation leakage and no band-gap occur in SIW transmission lines [12]. They can be summarized in four equations:

1. The first one has a physical reason: the diameter d of the metallized vias must be smaller than their longitudinal spacing s, and therefore:

$$s > d \tag{2.23a}$$

2. The second one, which blocks any band-gap in the single-mode frequency of the waveguide, relates the longitudinal spacing between the vias s to the cutoff wavelength:

$$\frac{s}{\lambda_c} < 0.25 \tag{2.23b}$$

3. The third equation sets a limit to the maximum spacing between the vias in order to minimize the radiation leakage, and relates s to the post diameter d:

$$\frac{s}{d} < 2 \tag{2.23c}$$

4. Finally, in order to avoid over-perforated substrates, the vias should not be more than 20 per wavelength:

$$s > \frac{\lambda_c}{20} \tag{2.23d}$$

2.3 Additive Manufacturing Technologies

In order to describe what Additive Manufacturing is, the best thing is to use a definition from American Society for Testing and Materials (ASTM)[1]. It says that AM consists of "a process of joining materials to make objects from 3D model data, usually layer upon layer, as opposed to subtractive manufacturing methodologies".

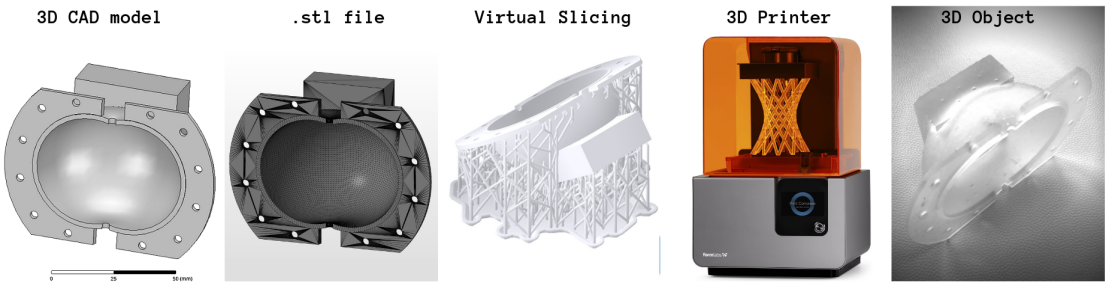

Figure 2.10: Steps of a general 3D-printing process.

As summed up in Fig. 2.10, every 3D-printing process is constituted by 5 steps: once a CAD sketch is produced with 3D modeling software, the AM equipment reads

[1] ASTM is an international standards organization that develops and publishes voluntary consensus technical standards for a wide range of materials, products, systems, and services.

in data, creating a .stl file, which describes a solid through the discretization of its surface in triangles. A virtual slicing is successively done via software (cura, Slic3r,...) and, finally, the file is passed to the printer, which lays down or adds successive layers of liquid, powder, sheet material or other, in a layer-upon-layer fashion, creating the 3D object [13].

Although media likes to use the term "3D Printing" as a synonym for all additive manufacturing processes, there are actually lots of individual processes which vary depending on the used material, and the way it is deployed and cured.

Hence, in 2010, the ASTM International Committee F42 on Additive Manufacturing Technologies formulated a set of standards that classify the range of Additive Manufacturing processes into 7 categories [14],[15]:

Binder jetting: a liquid bonding agent is selectively deposited to join powder materials.

Material extrusion: material is selectively dispensed through a nozzle or orifice (Fused Deposition Modeling).

Direct energy deposition: focused thermal energy is used to melt materials as they are being deposited.

Material jetting: droplets of build materials are selectively deposited (3-D inkjet printing).

Powder bed fusion: thermal energy selectively fuses regions of a powder bed (Electron Beam Melting, Selective Laser Melting).

Sheet laminations: sheets of material are bonded to form an object.

Vat photo-polymerization: liquid photopolymer in a vat is selectively cured by light-activated polymerization (Stereolithography).

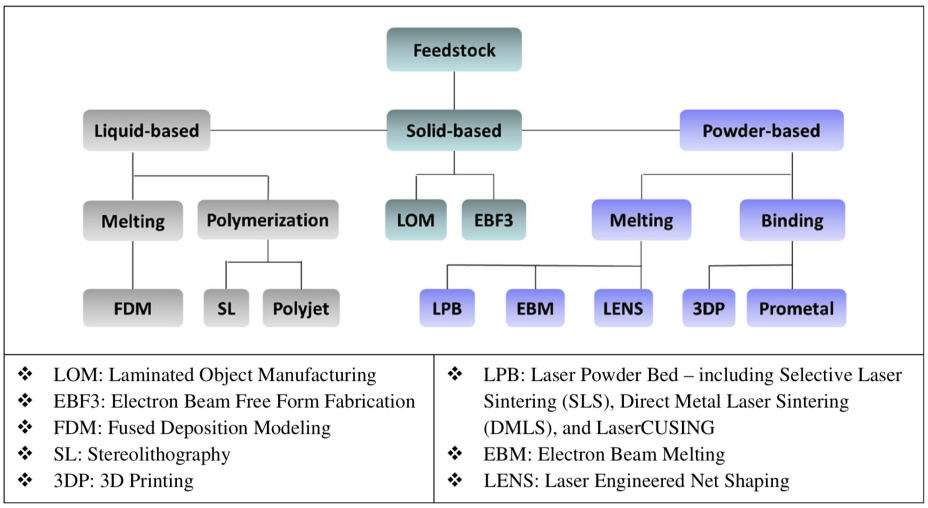

Figure 2.11: Classification of AM technologies based on input material [16].

Fig. 2.11 shows a possible classification of the aforementioned AM technologies, which is based on the material used for the fabrication [16].

In the following sections, two of these techniques are presented in detail, Fused Deposition Modeling (FDM) and Stereolithography (SLA). These two technologies, indeed, are the one used to print the devices objects of this thesis.

2.3.1 Material Extrusion

This process was patented by Stratasys Inc. in 1992, with the name of Fused Deposition Modeling (FDM).

This process consists in having a thermo-plastic filament pushed through a heating chamber and then extruded through a small nozzle, which deposited it layer by layer. The nozzle can move horizontally and a platform moves up and down vertically after each new layer is deposited. The printable material is extruded in a continuous stream and is kept under constant pressure, in order to enable accurate results. Material layers can be bonded by temperature control or through the use of chemical agents.

Here the process is described step-by-step (Figure 2.12):

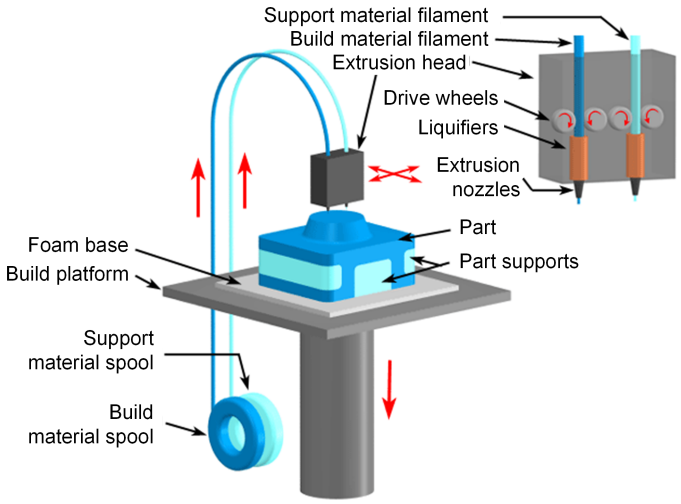

Figure 2.12: The FDM process. As we see here, material is often added to the machine in spool form [17].

1. After the material is heated in the liquefier chamber, the first object slice is built as nozzle deposits the semi-liquid material;
2. The build platform is lowered and other material is deposited on top of previous layers;
3. The process restarts.

Advantages and disadvantages

The most significant advantage of FDM is the use of thermoplastics filaments like PLA and ABS, which are easily accessible materials that allow to produce models with good structural properties. These benefits contribute to making FDM the most inexpensive and widespread process, used also on many inexpensive, domestic and hobby 3D printers.

On the other hand, this process has the lowest resolution ($\pm 0.15\,\text{mm}$) with respect to all the other processes; it is the nozzle radius that, indeed, limits the final quality of the printed object. Moreover, this technique requires post-processing, which consists in heat treatment, sanding and removal of support structures.

2.3.1.1 3D-Printer

Fig. 2.13 is a photograph of the 3D printer used for the fabrication of (part of) the first prototype of microfluidic sensor, described in Chapter 3. It is the 3NTR A4v3 model, and exploit the triple extruder technology (two extruder for the materials and one for the soluble support).

This printer works with thermoplastic materials. We chose to use acrylonitrile butadiene styrene (ABS) for our device because of its ductility and machinability, which makes it particularly suited for end use products [18].

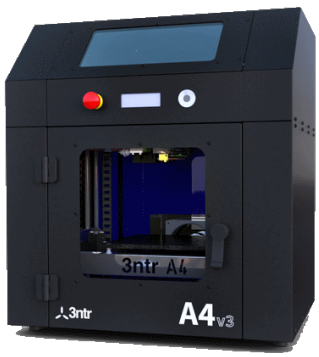

Figure 2.13: 3NTR A4v3, the FDM printer used for the fabrication of the first prototype of microfluidic sensor [15].

2.3.2 Vat Photo-Polymerization

Vat photopolymerization process, also known as stereolithography (SLA), was invented by an American engineer, Charles Hull, in 1984.

This process uses a vat of liquid photopolymer resin, out of which the model is constructed layer by layer. The resin is cured using UV light, which is directed on

it with the use of motor controlled mirrors, while a platform moves the object being made downwards after each new layer is cured.

As the process uses liquid to form objects, support structures will often need to be added during the build phase.

Here the process is described step-by-step (Figure 2.14) [19]:

1. The build platform is lowered downwards by the layer thickness while UV light cures the resin layer by layer.
2. The previous step is repeated and additional layers are continuously built on top of the former.
3. Once the object has been realized, the vat is drained of resin and the object removed.

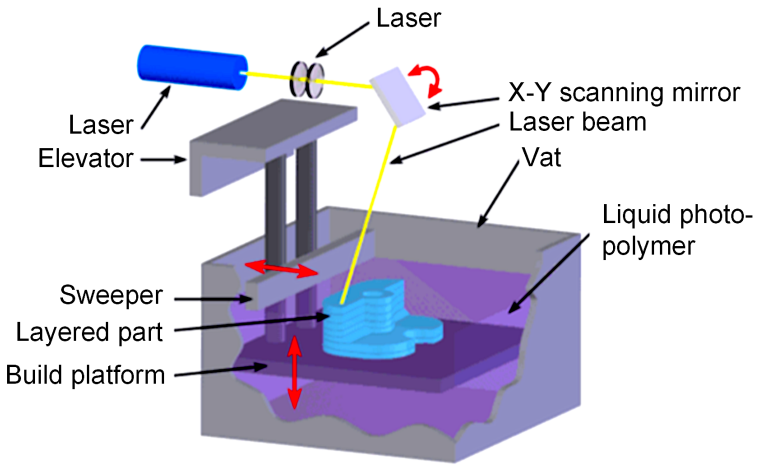

Figure 2.14: Vat Photopolymerization process [20].

Advantages and disadvantages

The advantages of vat photopolymerization consist in a high level of accuracy (± 0.025 mm) and good surface finish. Moreover the process is relatively quick.

The drawbacks are the high cost of the process, the length of the post processing time, and the limited range of usable materials.

2.3.2.1 3D-Printer

Fig. 2.15 is a photograph of the 3D printer used - as described in Chapter 3 - for the fabrication of (part of) the first prototype and for the realization of the second one. It is the FORM 2 Desktop SLA and employs photopolymeric resins to create the object. It prints, with a high level of precision (100/50/25 μm), medium/small models with fine details.

This printer works with photopolymer resins. We chose the Clear FLGPCL02 (and, later, Clear FLGPCL04) amongst the resins provided by Formlabs because, as the name says, it is transparent and so it is easier, once the printing process is completed, to assess the inner structural integrity of the components.

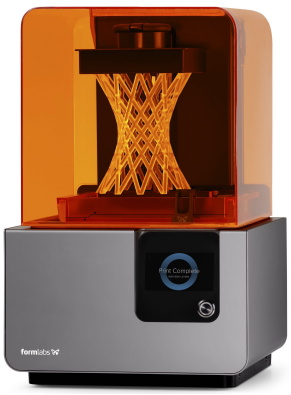

Figure 2.15: FORM 2 Desktop SLA, the stereolithography printer used for the fabrication of the first and second prototypes of microfluidic sensors [15].

2.4 Dielectric Material Characterization

In recent years, AM is being increasingly employed for the manufacturing of a wide variety of RF and microwave components and antennas. The design and the modeling of these devices requires the adopted 3D-printed dielectric substrate to be accurately characterized at microwave frequencies.

Thus, anytime a new 3D printed material has to be used for the fabrication of microwave devices, a preliminary electromagnetic (EM) characterization of its electrical properties is mandatory.

Since the 3D-printed dielectric materials adopted to fabricate the devices described in this PhD thesis were *non-magnetic*, their permeability was real, and in particular $\mu = \mu_0$. Thus, in order to be characterized, it was enough to extract their permittivity ε_{3D} and loss tangent $\tan\delta_{3D}$. We thus considered only the contribution of the complex dielectric permittivity:

$$\varepsilon = \varepsilon_0(\varepsilon'_{3D} - j\varepsilon''_{3D}) = \varepsilon_0\varepsilon'_{3D}(1 - j\tan\delta_{3D}) \tag{2.24}$$

2.4.1 Dielectric Materials Characterization Techniques

Each dielectric characterization method has its frequency range of applicability, and, also, uses a specific electric-field orientation [21]. They are usually divided in

two categories: resonant methods and non-resonant methods. While the former allows to have accurate information on dielectric properties at single or several discrete frequencies, the latter permits to get an overall knowledge of the electromagnetic properties over a certain frequency range [4].

2.4.1.1 Resonant Methods

Resonant methods are based, as the name suggests, on resonant cavities theory. In a resonant cavity with given dimensions, the resonant frequency and the quality factor are determined just by the permittivity and the permeability of the material constituting the cavity.

Within the resonant methods set, are generally included the resonator method and the resonant-perturbation method. Both methods exploit the capability of extracting material characteristics by measuring the resonant frequency and the quality factor of a resonant cavity. The difference between them is that, while in the resonator method it is the resonator itself to be constituted by the material to be characterized, in the resonant-perturbation method the sample to characterize is inserted inside a resonator with given EM boundaries.

As examples, in Fig. 2.16 are reported two experiments where these methods have been adopted to characterize materials: in Fig. 2.16(a) a ring resonator is used to characterize a substrate, in Fig. 2.16(b) an SIW cavity, fabricated using standard substrate, permits to characterize liquids injected in a glass testing pipe positioned at the center of the cavity.

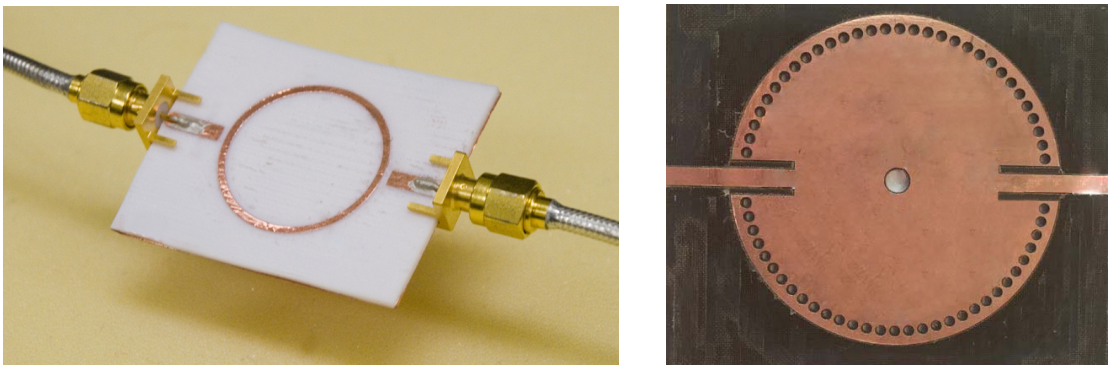

(a) (b)

Figure 2.16: Characterization of materials with resonant methods: (a) with a ring resonator [22]; (b) with an SIW cavity [23].

Resonant methods are largely adopted for materials characterization, because of their high accuracy and sensitivity. As said, the key condition to apply this technique

for material characterization is that the sample to test constitute the whole resonator or a critical portion of it, so that the algorithm to calculate the sample's properties is related to the EM field distributions inside the resonator (and the sample). In particular, in a resonator, the more the electric energy is concentrated on the sample under test, the higher is the sensitivity and the accuracy of the characterization method [4].

The resonant method constitutes the key concept exploited for the characterization of LUTs with the 3D-printed sensor, as will be explained in the following chapters.

2.4.1.2 Non-Resonant Methods

In non-resonant methods, the properties of materials are fundamentally deduced from their impedance and the wave velocity in the materials. In fact, when an EM wave propagating in free space bumps into the interface with another material, both the characteristic wave impedance and the wave velocity change. Due to the presence of the interface, a part of the energy is transmitted through the interface and a part is reflected back (Fig. 2.17). By computing the complex ratio of transmitted and reflected waves, it is then possible to get enough information to retrieve the permittivity relationship between the two materials.

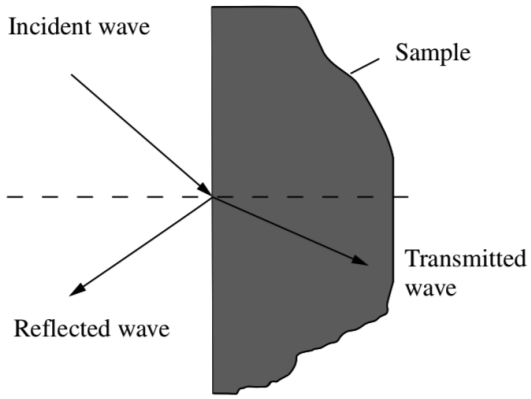

Figure 2.17: Boundary condition for material characterization using a nonresonant method [4].

Since non-resonant methods consist in directing the electromagnetic energy toward a material, and, then, measuring what is reflected-back/transmitted-through the material, any kind of transmission line can be used to characterize materials: coaxial lines, hollow metallic waveguides, dielectric waveguides, planar transmission lines and free space.

In the two following sections, three techniques are presented, which are the ones used to characterize the samples of 3D-printed materials: the microstrip line technique,

the waveguide technique and the coaxial probe technique. The instrumentation and the specimen preparation are illustrated, as well as the measurements results.

Waveguide Technique Waveguides are widely used, due to their relative simplicity, as broadband measurement techniques. These methods consist in having a precisely machined specimen which is placed in a section of waveguide and, then, in measuring the scattering parameters with a VNA. For simplicity of fabrication of the sample, a hollow rectangular waveguide was used to characterize the material, in the open-ended configuration. The presence of the sample inside the waveguide generates an impedance discontinuity, which causes EM energy reflection that, in turn, permits the extraction of the electromagnetic properties of the sample.

Of course, the selection of the waveguide to be used depends on the frequencies range in which we need to characterize the sample. Since we want the microfluidic sensor to work in the lower UWB, the range of frequencies from 3 GHz to 5 GHz, at least, has to be covered.

This can be done by using two rectangular waveguides, WR-284 and WR-187, whose frequency and size characteristics are reported in Table 2.1. FORM 2 Desktop SLA printer (subsubsection 2.3.2.1) was employed to print the samples of resin Clear FLGPCL04, whose dimensions follow, of course, the dimensions of the waveguides.

Waveguide name	**Recommended frequency**	**Cutoff frequency lowest order mode**	**Cutoff frequency next mode**	**Inner dimensions of waveguide opening**	
				a **(mm)**	***b*** **(mm)**
WR-284	2.60 - 3.95 GHz	2.078 GHz	4.156 GHz	72.136	34.036
WR-187	3.95 - 5.85 GHz	3.153 GHz	6.305 GHz	47.5488	22.1488

Table 2.1: Details on the two rectangular waveguides used for sample characterisation.

As shown in Fig. 2.18, the setup is constituted by a truncated metallic waveguide which is connected to the VNA by a coaxial-to-waveguide right angle adapter. The waveguide is placed against a brass plate, which constitutes a short circuit. A foil of aluminum was also added, improving the results. The sample to be characterized was inserted in the lower portion of the waveguide, to be in contact with the metallic slab.

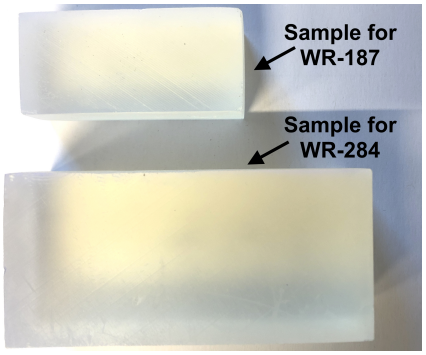

(a)

(b)

(c)

Figure 2.18: Setups used for the S-parameter measurements: (a) 3D-printed samples; (b) WR-284; (c) WR-187.

In the meanwhile, with CST Microwave Studio software, the electromagnetic simulation of the systems was performed. The purpose was to use these simulations (where $\varepsilon_{\text{sample}}$ and $\tan\delta_{\text{sample}}$ represented the variables) to fit the measurement.

Once completed the measurements of the S_{11}, they were imported in CST and, subsequently, magnitude and phase error functions (between simulations and measurements) were computed, as

Magnitude Error Function (MEF):

$$\mathbb{E}rr_M = 100 \left| \frac{|\overline{S_{11}^{sim}}| - |\overline{S_{11}^{meas}}|}{|\overline{S_{11}^{meas}}|} \right| \tag{2.25a}$$

Phase Error Function (PEF):

$$\mathbb{E}rr_P = \frac{180}{\pi}\left|\mathcal{U}(\angle\overline{S_{11}^{sim}}) - \mathcal{U}(\angle\overline{S_{11}^{meas}})\right| \tag{2.25b}$$

where $\overline{S_{11}^{sim}}$ and $\overline{S_{11}^{meas}}$ denote, respectively, the simulated and measured S_{11} normalized to shorted condition, while $\mathcal{U}$ indicates the phase-unwrapping function.

Once computed MEF and PEF, a CST optimization algorithm was used to minimize them. This algorithm, basically, performs the S-parameters analysis of the system while changing, inside a user-defined range, $\varepsilon_{\text{sample}}$ and $\tan\delta_{\text{sample}}$. In this way, $\varepsilon_{\text{sample}}$ and $\tan\delta_{\text{sample}}$ that best fit simulations to measurements were extracted.

Fig. 2.19 shows the plots obtained once the minimization algorithm was applied to the system with WR-284. On the y-axis the magnitude and phase error functions are reported *versus* the frequency range, which goes from the cutoff frequency of the lowest order mode to the cutoff of the next mode. The red lines represent the initial error functions, while the green line show the best result obtained once the parametric analysis was completed. This analysis gave as output an $\varepsilon_{\text{sample}} = 2.9$ and a loss tangent $\tan\delta_{\text{sample}} = 0.034$.

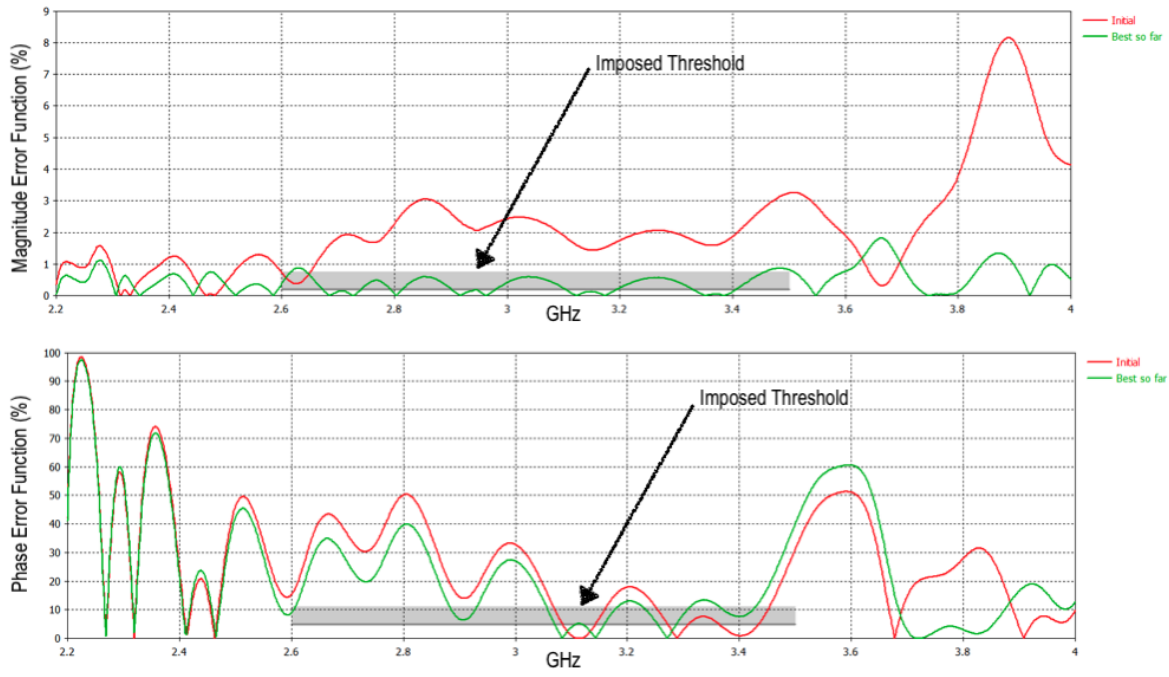

Figure 2.19: MEF and PEF in percentage. After the minimization algorithm was applied, the functions drop almost completely below the strict user-fixed threshold.

Microstrip Line Technique In this case, the sample under test is the microstrip-line substrate itself, and its EM characteristics are obtained from

transmission and reflection properties of the microstrip circuit. The advantage of using microstrips instead of closed structures is that no air gap exists between the strip and the substrate. On the other hand, however, open structures can radiate and have a field structure which is difficult to compute.

The calculation of material properties is based on the S-parameter measurements of microstrip lines at their access planes (P_1 and P_2 in Fig. 2.20). This method is based on formulas in [24], and requires two lines with different lengths.

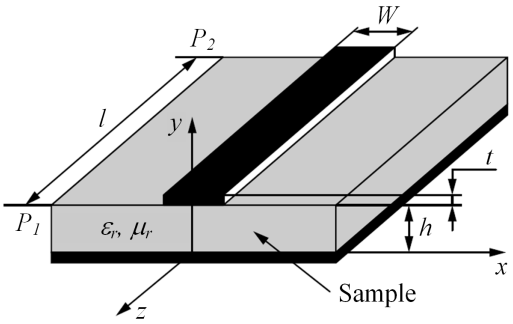

Figure 2.20: Microstrip transmission line [4].

The phase values of the S_{21}, measured for both the lines, allow the determination of the phase constant β as

$$\beta = \frac{\Phi_2(f) - \Phi_1(f)}{\ell_2 - \ell_1} = \frac{\Delta\Phi}{\Delta\ell} \tag{2.26}$$

where ℓ_1 and ℓ_2 represent the length of the two microstrip lines.

The effective dielectric constant of the microstrip lines can then be calculated as

$$\varepsilon_e = \left(\frac{\beta\, c}{2\pi f}\right)^2 \tag{2.27}$$

where c is the light speed in vacuum and f is the measurement frequency.

From the expression relating ε_e to ε_r, the dielectric permittivity is finally retrieved:

$$\varepsilon_r = \frac{2\varepsilon_e - 1 + \frac{1}{\sqrt{1+12\frac{d}{w}}}}{1 + \frac{1}{\sqrt{1+12\frac{d}{w}}}} \tag{2.28}$$

The loss tangent, instead, can be calculated as

$$\tan\delta = \frac{\alpha_d\, \lambda_0\, \sqrt{\varepsilon_e}(\varepsilon_r - 1)}{\pi\, \varepsilon_r(\varepsilon_e - 1)} \tag{2.29}$$

where $\alpha_d = -\frac{\ln(S_{21})}{l}$ [Np/m] is the attenuation constant due to the dielectric, and λ_0 is the wavelength in vacuum.

The microstrip method has been used to characterize both ABS and Clear FGLPLC02. In Fig. 2.21(a) and Fig. 2.21(c) the photographs of the 3D-printed microstrip lines prepared for the characterization are reported; in Fig. 2.21(b) and Fig. 2.21(d) the dielectric permittivity and the loss tangent extracted are reported.

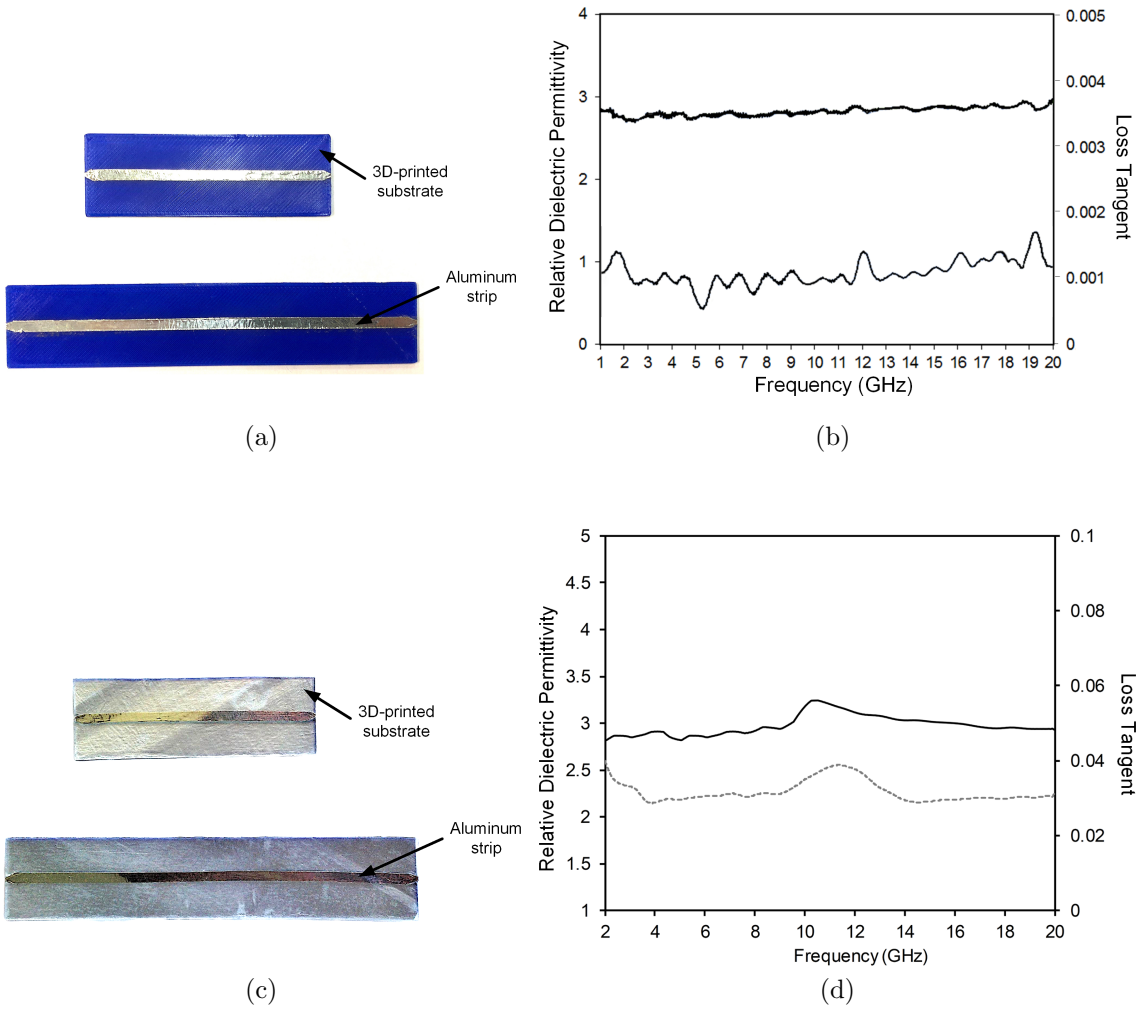

Figure 2.21: Dielectric characterization of 3D-printed substrates: (a) Photograph of ABS microstrip lines; (b) Dielectric permittivity and loss tangent extracted; (c) Photograph of Clear FLGPCL02 microstrip lines; (d) Dielectric permittivity and loss tangent extracted.

In the frequency range of interest, we obtained $\varepsilon_{\text{sample}} = 2.75$ and $\tan\delta_{\text{sample}} = 0.001$ for the ABS and $\varepsilon_{\text{sample}} = 2.9$ and $\tan\delta_{\text{sample}} = 0.031$ for the photopolymeric resin. These last results are in good agreement with the ones obtained with waveguide characterization, thus highlighting the validity of the methods.

Table 2.2 summarizes the results obtained from the dielectric characterization of the 3D-printed materials used for the proposed devices.

	ABS	**Clear FLGPCL02/04**	
	Microstrip Characterization Technique	Waveguide Characterization Technique	Microstrip Characterization Technique
ε_r	2.75	2.9	2.9
$tan\delta$	0.001	0.034	0.031

Table 2.2: Dielectric permittivity and loss tangent of the 3D-printed materials used for the realization of the devices discussed in this thesis.

Coaxial Probe Technique This open - reflection method was employed as reference method for the characterization of the LUTs used in the microfluidic sensors described in Chapter 3 and Chapter 5. Electromagnetic waves are directed on the sample and, by looking at the reflection coefficient at a defined reference plane, the properties of the material sample are retrieved.

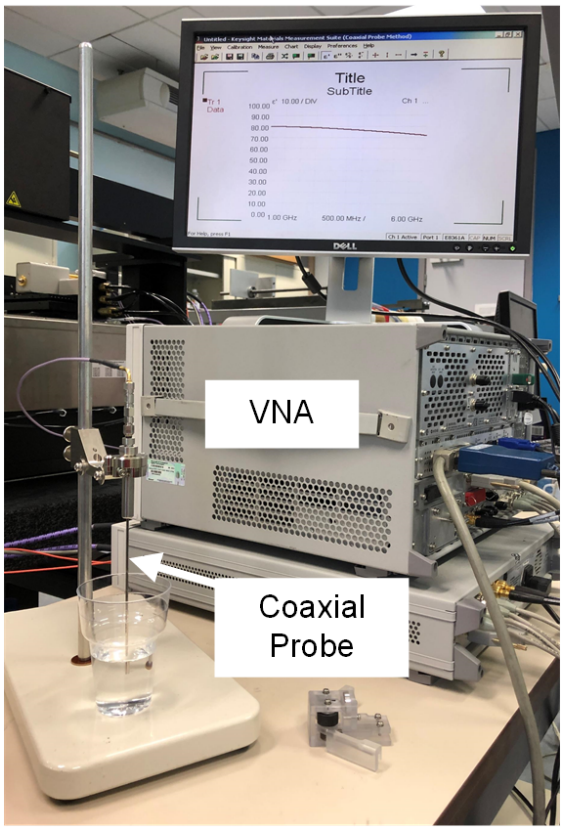

Figure 2.22: Measurement setup with coaxial probe for liquids characterization.

We used the commercial open-ended coaxial probe Keysight N1501A Dielectric Probe Kit, operating over the frequency range from 0.5 GHz to 50 GHz. As shown in Fig. 2.22, the open-ended coaxial probe is connected through a flexible coaxial cable to the vector network analyzer (VNA) Keysight E8361A. Proprietary software converts

the measured reflection coefficient into the complex dielectric permittivity of the LUT. This setup was used as the reference method, as will be better explained in Section 3.4.

The coaxial probe has been used to characterize, in the frequency band of interest (from 2 GHz to 5 GHz) ten different LUTs. Fig. 2.23 reports the resulting plots for the permittivity and the loss tangent. All these LUTs will be used to test the microfluidic sensors described in Chapter 3 and Chapter 5.

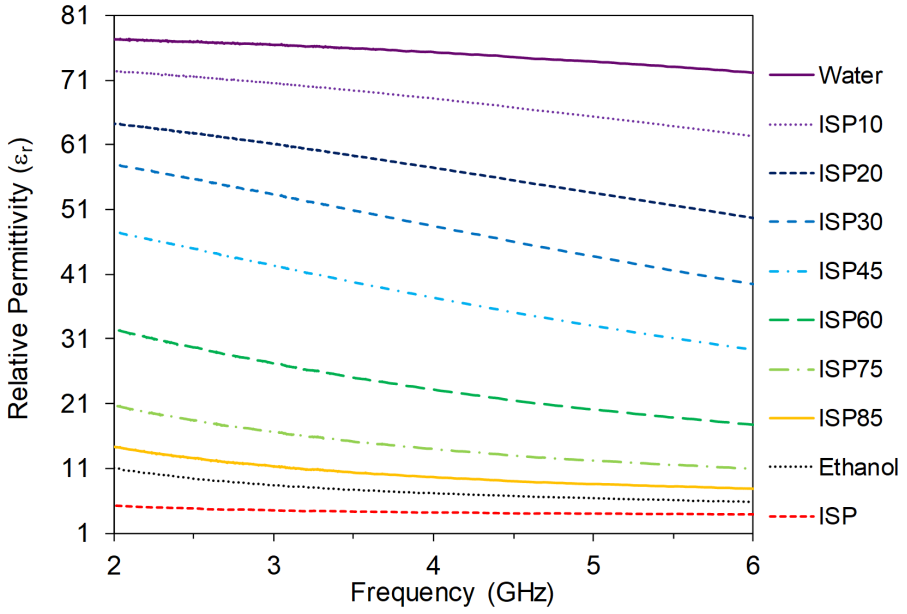

(a)

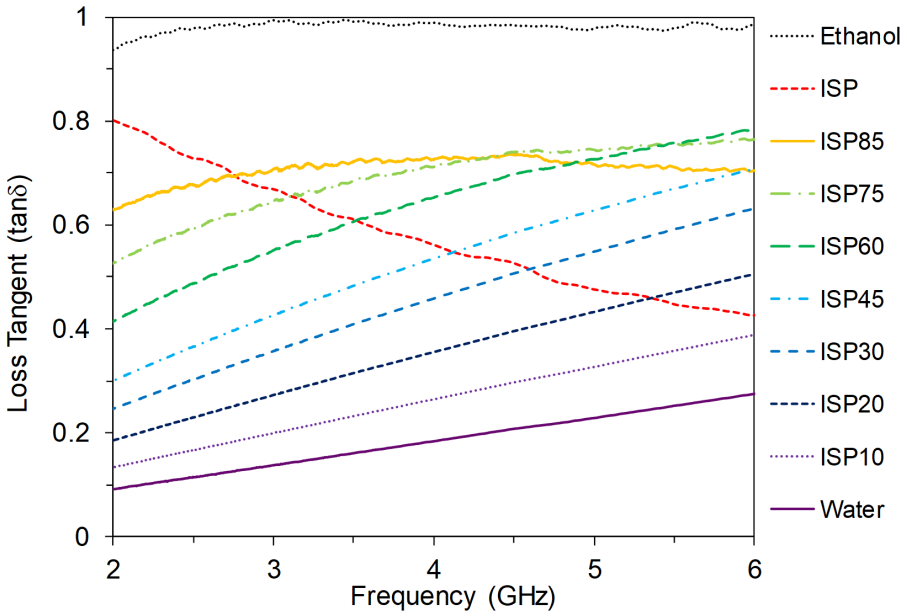

(b)

Figure 2.23: Characterization of the LUTs with the coaxial probe: (a) dielectric permittivity; (b) loss tangent.

2.5 Chapter Summary

This chapter provides a technical introduction to the technologies and the structures adopted to fabricate the microfluidic sensors subject of this thesis. Resonant cavities theory is presented, as they constitute the basic structures for the microfluidic devices discussed in Chapter 3 and Chapter 5. SIW technology has then been introduced, as it was applied, in Chapter 3, for the metallization of the square microfluidic sensor. The fundamental difference between standard waveguides and SIW structures consists in the presence of metallic screws that create the side walls. For this reason, design rules that regulate the distance between the vias are presented. They allow to control the radiation leakage as well as the band-gap effect. Eventually, Additive Manufacturing technologies have been presented, with a special focus on Material Extrusion (FDM) and Vat Photopolymerization (SLA), which are the ones employed in this thesis. The techniques to characterize, in microwave region, the printed material are then discussed, together with the coaxial probe method, which allows to retrieve the permittivity and loss tangent of the LUTs later injected in the sensor. The coaxial probe represents a reference method for the algorithm to retrieve the dielectric properties which will be presented in the following chapter.

This page is intentionally left blank

References

[1] R. Sorrentino, G. Bianchi, *Ingegneria delle microonde e radiofrequenze*, McGraw-Hill, 2014.

[2] R. J. Cameron, C. M. Kudsia, and R. Mansour, *Microwave Filters for Communication Systems*, John Wiley & Sons, 2007.

[3] K. Kurokawa, *An Introduction to the Theory of Microwave Circuits*, Academic Press, 1969.

[4] L. F. Chen, C. K. Ong, C. P. Neo, V. V. Varadan, and V. K. Varadan, *Microwave Electronics: Measurement and Materials Characterization*, Hoboken, NJ, USA: Wiley, 2004.

[5] M. Bozzi, A. Georgiadis, and K. Wu "Review of Substrate Integrated Waveguide Circuits and Antennas," *IET Microwaves, Antennas & Propagation*, Vol. 5, No. 8, pp. 909-920, June 2011.

[6] R. Garg, I. Bahl, and M. Bozzi, *Microstrip Lines and Slotlines*, Third Edition, Artech House, May 2013.

[7] M. Bozzi, M. Pasian, L. Perregrini, and K. Wu, "On the losses in substrate-integrated waveguides and cavities," *International Journal of Microwave and Wireless Technologies*, 1(5), 395-401, 2009.

[8] M. Bozzi, M. Pasian, and L. Perregrini, "Advanced modeling and design of substrate integrated waveguide components," *2014 IEEE International Wireless Symposium (IWS 2014)*, X'ian, 2014, pp. 1-4.

[9] Y. Cassivi *et al.*, "Dispersion Characteristics of Substrate Integrated Rectangular Waveguide," *IEEE Microwave Wireless Component Letters*, Vol. 12, No. 9, pp. 333-335, Sept. 2002.

[10] M. Bozzi , L. Perregrini , K. Wu, and P. Arcioni, "Current and future research trends in substrate integrated waveguide technology," *Radioengineering* Vol. 18, No. 2, pp. 201 - 209, June 2009.

[11] M. Pasian, M. Bozzi, and L. Perregrini, "A Formula for Radiation Loss in Substrate Integrated Waveguide," *IEEE Transactions on Microwave Theory and Techniques*, Vol. 62, No. 10, pp. 2205-2213, Oct. 2014.

[12] D. Deslandes and K. Wu, "Accurate modeling, wave mechanisms, and design considerations of a substrate integrated waveguide," *IEEE Transactions on Microwave Theory and Techniques*, vol. 54, no. 6, pp. 2516-2526, June 2006.

[13] H. Giberti, *Modellazione CAD*, lecture notes, "Virtual Modeling and Additive Manufacturing" course, Almo Collegio Borromeo, delivered 2 November 2017.

[14] *AM Basics*, Additive Manufacturing, `http://additivemanufacturing.com/basics/`, accessed 4 September 2019.

[15] F. Auricchio, *Stampa 3D come tecnologia abilitante: sviluppo di nuove idee progettuali, dalla chirurgia all'edilizia*, lecture notes, "Virtual Modeling and Additive Manufacturing" course, Almo Collegio Borromeo, delivered 31 October 2017.

[16] Y. Zhai, D. A. Lados, and J. L. LaGoy, "Additive manufacturing: Making imagination the major limitation," JOM-J. Minerals Met. Mater. Soc., vol. 66, no. 5, pp. 808-816, May 2014.

[17] *Fused Deposition Modeling (FDM)*, `https://www.custompartnet.com/wu/fused-deposition-modeling`, accessed 4 Sept. 2019.

[18] *PLA vs. ABS: What's the difference?*, `https://www.3dhubs.com/knowledge-base/pla-vs-abs-whats-difference/#what-are-abs-and-pla`, accessed 4 Sept. 2019.

[19] `https://www.lboro.ac.uk/research/amrg/about/the7categoriesofadditivemanufacturing/vatphotopolymerisation/`, accessed 4 Sept. 2019.

[20] *Stereolithography*, `https://www.custompartnet.com/wu/stereolithography`, accessed 4 September 2019.

[21] J. B. Jarvis *et al.*,"Measuring the Permittivity and Permeabiiity of Lossy Materials: Solids, Liquids, Metals, Building Materials, and Negative-Index Materials", NIST technical note, 2005.

[22] S. Moscato *et al.*, "Infill Dependent 3D-Printed Material Based on NinjaFlex Filament for Antenna Applications," *IEEE Antennas and Wireless Propagation Letters*, Vol. 15, pp. 1506-1509, Jan. 2016.

[23] E. Massoni, G. Siciliano, M. Bozzi and L. Perregrini, "Enhanced Cavity Sensor in SIW Technology for Material Characterization," *IEEE Microwave and Wireless Components Letters*, vol. 28, no. 10, pp. 948-950, Oct. 2018.

[24] D. M. Pozar, *Microwave Engineering*, John Wiley & Sons, 2005.

This page is intentionally left blank

Chapter 3

3D-Printed Square Microfluidic Sensor

This chapter presents two 3D-printed microwave sensors for the characterization of liquids which operate in the lower portion of the UWB band. As said in Chapter 1, the choice of this range of frequencies is dictated by the fact that, since these devices are conceived to be possibly used in WSNs, it is sufficiently high to allow the creation of devices with reasonable dimensions for end-use purposes but also sufficiently low so that no significant issues related to 3D-printed material roughness could arise.

In section 3.1 the design of the microfluidic sensors are reported, along with a presentation of the simulations results. Later, the fabrication details are discussed in section 3.2 and the measurements results are presented (section 3.3). Eventually, in section 3.4 the method developed to extract the properties of the liquid under test is presented, followed by chapter summary.

3.1 Design of Square Microfluidic Sensors

The proposed sensor consists of a square SIW cavity with an embedded multi-folded pipe, where the LUT can be injected and its dielectric characteristics extracted. The reason why such a shape was chosen to be used was that, as it was the first prototype, we preferred to start from a standard shape. In particular, a square shape was preferred to a rectangular one because, considering the same fundamental mode, in a square structure the quality factor is higher than in a rectangular structure.

In the course of this PhD, two different prototypes of SIW microfluidic sensor have been designed and realized, using two different AM processes and materials. Since the two prototypes are similar from the point of view of the design, the basic design is

presented first, and then, in the fabrication section, the differences between the two prototypes will be highlighted.

As shown in Fig. 3.1, the sensors consist of a square SIW cavity with a meandered micro-pipe inside, where the liquid under test (LUT) can be injected and extracted through two access points. This cavity has been designed to work with the fundamental TM_{110} mode (with respect to the z-axis) at 4 GHz with empty pipe. As known from (2.8), the resonance frequency of a cavity is related to both the cavity's dimensions and the effective dielectric permittivity of the material forming the cavity. When the LUT is injected in the pipe, the cavity's effective permittivity changes and, consequently, the frequency behaviour of the device changes. In particular, the resonance frequency decreases and, in addition, since the losses associated to the liquid are higher than losses of air, a reduction of the quality factor of the cavity mode occurs.

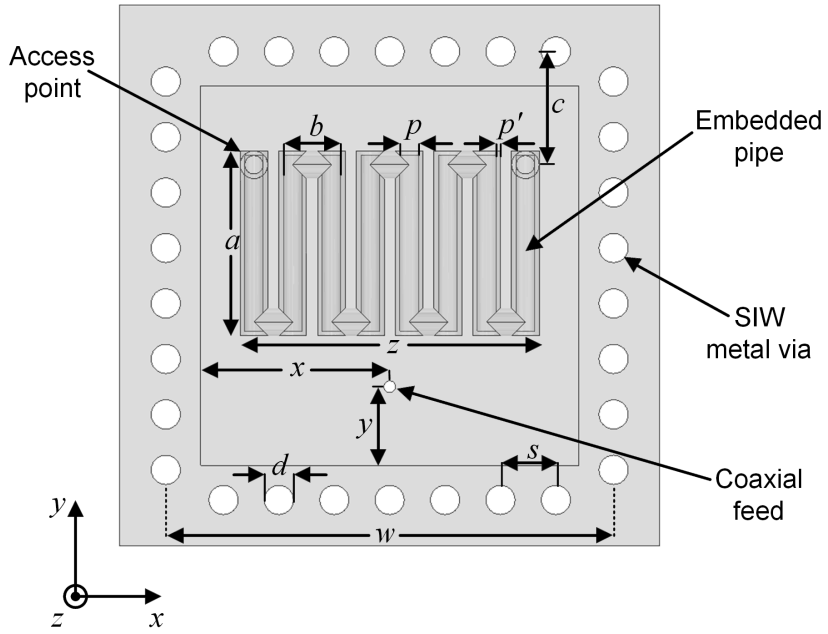

Figure 3.1: Geometry of the 3D-printed microfluidic sensors. In Table 3.1 are reported the different dimensions for both prototypes.

The purpose of this sensor is to allow the extraction of liquids' EM characteristics: to do so, we exploited the knowledge of resonance frequency and quality factor variation given by measurements. In fact, the former allows to retrieve the relative permittivity of the LUT, while the variation of the Q-factor permits to extract the LUT's losses.

By properly designing the geometry of the pipe, the frequency response of the sensor can be tailored, in such a way that the resonance frequency fits the desired frequency range. Moreover, the pipe shape was always chosen to maximize the effect of the fluid on the frequency variation and that it is compatible with the manufacturing process.

The resonant cavity is fed by a coaxial probe, positioned in a side portion of the cavity. The small opening to place the coaxial feed, as well as the holes to accomodate metal screws that constitute the cavity side walls, were realized in the dielectric during the printing phase. In order to determine the optimum location of the coaxial probe, the position of the pipe inside the cavity was considered fixed, and then parametric simulations, where the position of the coaxial pin was made variable, were performed for each LUT. The goal was to determine the position of the pin (its distance from the side of the cavity, y in Fig. 3.1) such that the coupling resulted maximized. Because of the wide range of permittivities (from $\approx$ 4to $\approx$ 80), the position of maximum coupling changed of few mm when considering empty-pipe case or water-filled case. For this reason, we decided to maximize the coupling in the intermediate cases. In Fig. 3.2, the $|S_{11}|$ plots resulting from parametric simulations performed with the mixture ISP 85% - Water 15%, are reported. As can be noticed, the coupling is maximum for $y = 9$ mm. This condition, which applies also in the case of ISP and the mixture ISP 75% - Water 25%, led us to choose y to be equal to 9 mm.

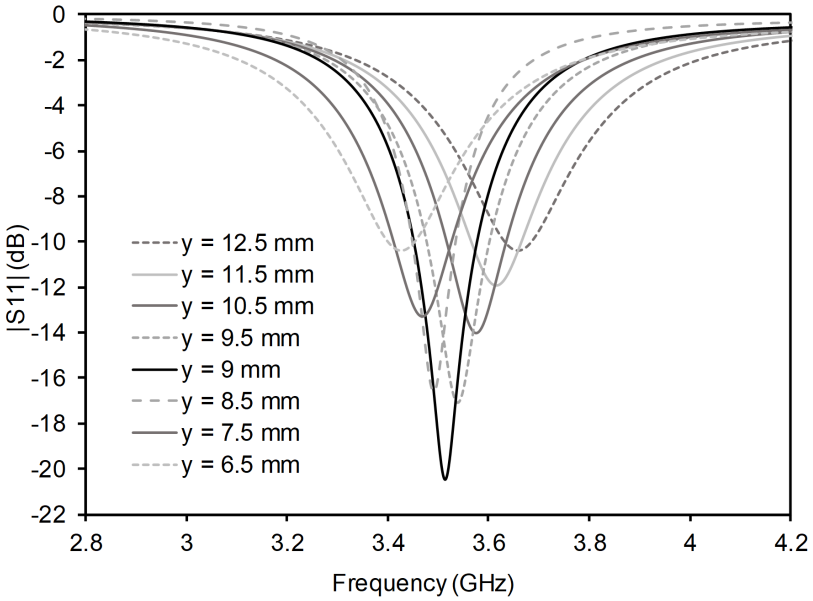

Figure 3.2: Simulations performed with pipe filled with ISP 85% - Water 15%. The position of the pin (indicated with y in Fig. 3.1) was made variable in a range of 6 mm.

The length a of the pipe was chosen in order to maximize the sensitivity while limiting the losses associated to the LUT, which impact significantly on the quality factor of the cavity mode, leading to a poor estimation of the LUT's loss tangent. Moreover, the number of turns have been chosen to cover as much as possible the central part of the cavity, where is the higher amplitude of the electric field of the TM_{110} mode.

1^{st}**Prototype**	**Dimensions (mm)**	2^{nd}**Prototype**	**Dimensions (mm)**
a	19.2	a	20.12
b	6.7	b	5.51
c	12.5	c	12.25
d	3.2	d	3.2
p	2	p	1.6
$p^{'}$	–	$p^{'}$	0.76
s	5.1	s	6
w	47	w	48.5
x	21	x	20.5
y	6	y	9
z	33.7	z	30.42

Table 3.1: Dimensions of the proposed 3D-printed microfluidic sensors (with reference to the labels in Fig. 3.1).

3.1.1 Simulations of Microfluidic Cavities

In this work, Ansys HFSS has been used as EM simulation tool. As previously mentioned, our purpose is to calculate the resonance frequency of the fundamental mode as well as the unloaded quality factor of the resonator. To do that, HFSS offers two different tools: the eigenmode analysis and the scattering parameter analysis.

By performing the **eigenmode analysis**, HFSS provides information about resonant frequency, unloaded Q factor, and field distribution. Once specified the frequency range, the eigenmode simulation tool identifies all the resonant modes existing in that range of frequencies.

If the **S-parameter** analysis is performed, the resonant frequency and quality factor need to be retrieved by looking at the S-parameters plots. Let's consider a 1-port device (our case): the S_{11} needs to be computed. For most of the frequencies, the RF energy is reflected back; in correspondence of the resonant frequencies, instead, there are dips. By looking at the location and the width of those dips, one can get, respectively, information about the frequencies at which the RF energy is stored in the resonator and information about the losses in the cavity (and thus information about the Q-factor).

Fig. 3.3 shows the amplitude of the electric modal field of the cavity's first resonant mode (TM_{110}) when the pipe is empty. The default HFSS color map, which is the rainbow one, indicates in red the areas where the E-field is more concentrated field and

in blue the areas where the amplitude of the E-field is zero. As expected from the first mode of a rectangular cavity, the electric field is more concentrated in the center of the cavity, in correspondence of the area where the pipe is placed, and gradually decreases its intensity while approaching the screws on the boundary of the cavity. As shown, with a spacing $s < 6$ mm between the screws, no field is radiated outside the cavity.

Fig. 3.4, instead, reports the magnitude of the simulated S_{11} - as function of frequency - when the pipe is filled with air, isopropanol 100%, a mixture of 85% isopropanol and 15% water, and distilled water. As expected, the minimum of the $|S_{11}|$ shifts downwards in frequency as the dielectric permittivity of the liquid inserted in the pipe increases.

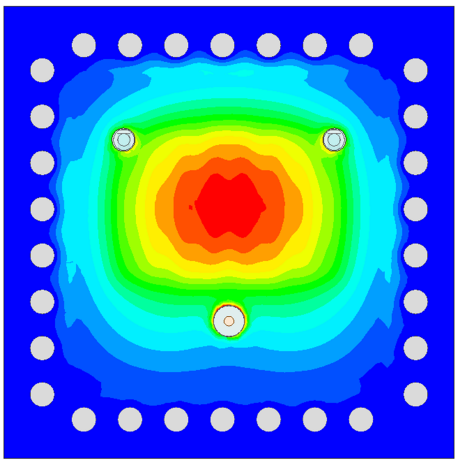

Figure 3.3: Amplitude of the electric modal field of TM_{110}.

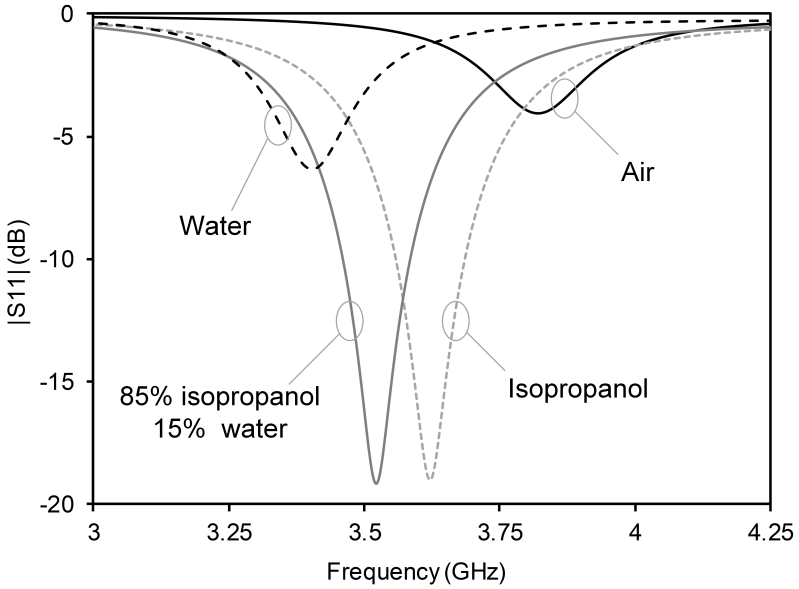

Figure 3.4: Simulated reflection coefficient in four different cases: with empty pipe and with the pipe filled with isopropanol 100%, a mixture of 85% isopropanol and 15% water, and distilled water.

3.2 Fabrication of Microfluidic Sensors

The prototypes were fabricated by the Proto-Lab, a laboratory belonging to the Department of Civil Engineering and Architecture of the University of Pavia. 3D-printing has been adopted to realize the entire structures, both the cavities and the multi-folded pipes.

On one hand, the use of 3D printing allows large flexibility in the design, especially as regards pipe shape and size. On the other hand, it presents a considerable drawback: 3D printed materials often exhibit large dielectric losses which leads, consequently, to a small quality factor when the material is used in a cavity resonator. In particular, the presence of large losses in the resonator could compromise an accurate retrieval of LUT's loss tangent.

In order to mitigate this problem, keeping the Q-factor as high as possible, design precautions were taken in both prototypes. In the first one, the infill percentage of the material constituting the core of the cavity was reduced; in the second prototype, instead of realizing a cavity completely filled of 3D-printed material, just an external dielectric case was designed (together with thin top and bottom layers, which provide planes for the metallization).

In Fig. 3.5 are reported the photographs of the two prototypes.

First Prototype

In order to fabricate this prototype, two different materials were used, ABS and Clear FGLPLC02, and two different AM technologies were adopted, FDM and SLA.

Fig. 3.6(a) shows a 3D side view of the 'disassembled' sensor, divided in three different parts according to the kind of material used:

- The top box, realized through SLA, has the meandered pipe inside.
- The part in the middle represents the portion of ABS substrate with an infill percentage equal to 20%. Thanks to 3D-printing, infact, it is possible to deposit material leaving air gaps between the different filaments, thus creating substrates with different percentage of infill. In [1], [2] it has been demonstrated that changing this percentage allows to decrease the permittivity and the losses of a substrate.
- The structure at the bottom is printed with ABS 100%. It has been used where strictly necessary, i.e., besides the bottom layer and the outer shell (where the screws would have been inserted), to print four square supports and thin walls - 0.5 mm thick - that keep in position the box with the pipe.

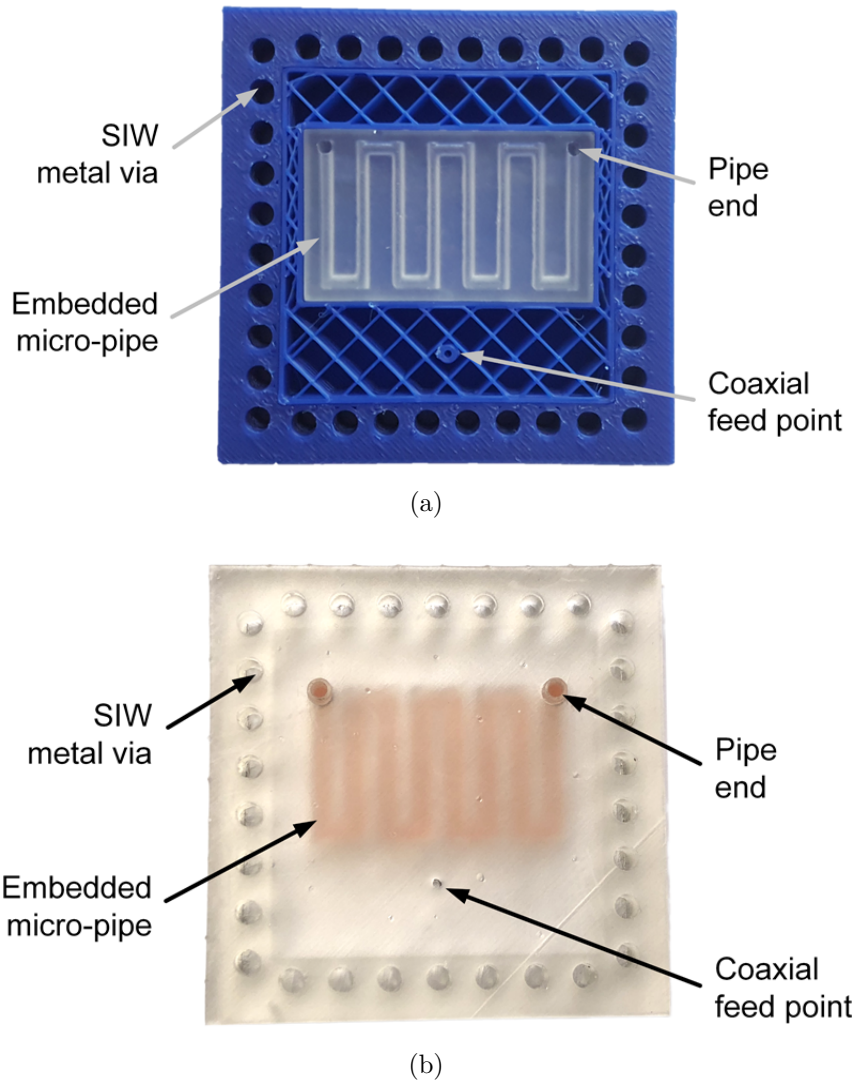

Figure 3.5: (a) Photograph of the first sensor prototype; (b) Photograph of the second sensor prototype.

The reasons why a different material was used to build the pipe box are that: first, the resin, differently from ABS, is completely waterproof (the LUTs we will consider are water-solubles) and, second, that the SLA printer guarantees a higher level of accuracy with respect to the FDM printer.

For these reasons, in the successive prototype, the whole structure was fabricated with photopolymer resin. Clear FLGPCL02 has higher losses compared to ABS, but their effect can be mitigated with a careful design, as described in the following section.

Second Prototype

The structure of the second prototype was completely realized in one step and with a single material [3]. SLA process and a transparent photopolymeric resin,

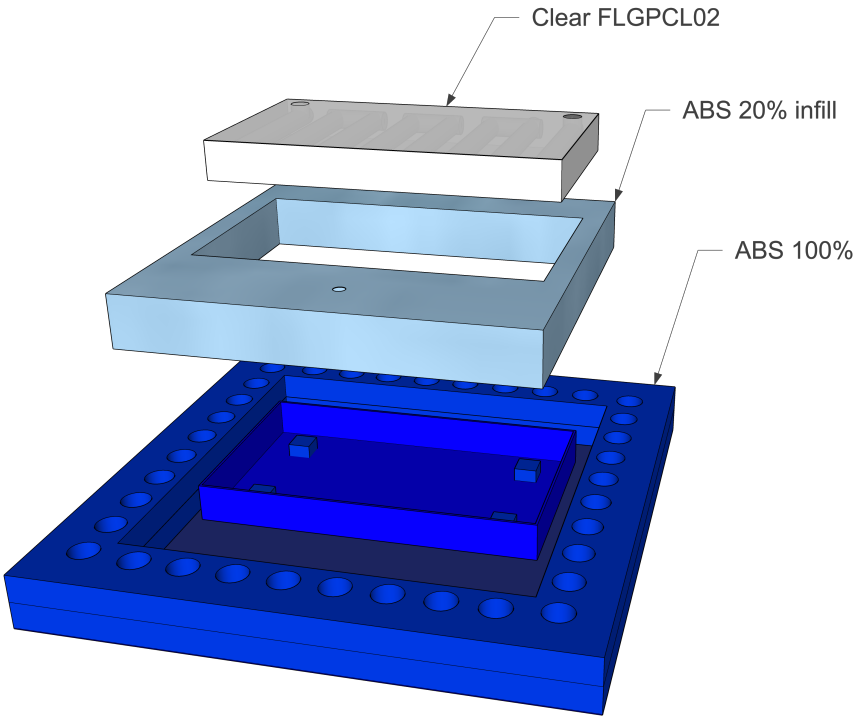

(a)

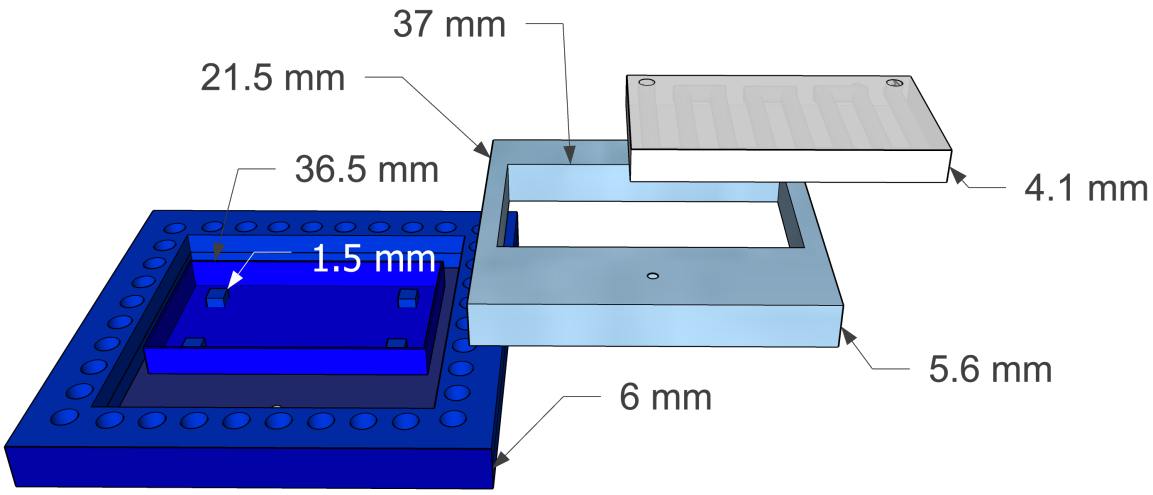

(b)

Figure 3.6: 3D exploded side views of the first sensor prototype: (a) with the different material that make it up indicated; (b) with cavity inner dimensions reported.

Clear FLGPCL02, were used.

As shown in Fig. 3.7, the pipe is located near the bottom of the cavity so that no supports (such as those present in the first prototype) are needed. Moreover, the walls of the pipe have the minimum thickness as to avoid any leakage of liquid.

The structure has a total height of 6 mm, divided in three layers: a bottom layer, 1 mm thick, which, together with the top one, create the plane for the metallization, and a central layer (a square shell empty inside) - 4 mm thick - with the minimum width

that allows to put the screws for the side metalization of the structure. The central core of the structure is left empty (with the exception of the pipe) to reduce as much as possible the dielectric losses.

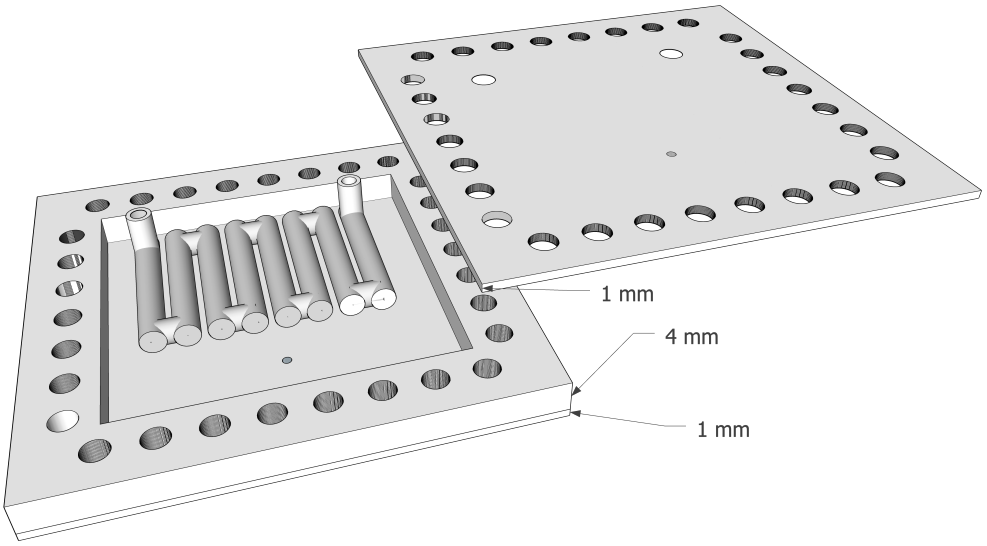

Figure 3.7: 3D side view of the second prototype, with thickness value reported.

3.2.1 Metallization

In both the sensors, the side metal walls, according to SIW technology, were realized through the use of steel screws inserted in the vias. The distance between these screws was fixed to fit them in the cavity boundary, also taking into account the recommended spacing needed to avoid radiation leakage, that is, less than two times the screw diameter (Eq. 2.23c).

As regards the metallization of top and bottom walls, aluminum foil and conductive glue (to make the foil stick to the 3D-printed surface) were used for the first prototype (Fig. 3.8(a)), while aluminum tape was applied to the second sensor (Fig. 3.8(b)).

3.3 Measurements of the Microfluidic Cavity

Nine different mixtures were tested in the sensor, prepared by varying the concentration of isopropanol and water. The reason why DI water and ISP have been used to produce the tested mixtures is strictly related to the relaxation frequencies of these two liquids. As reported in [4], indeed, the relaxation frequency of water if $f_{rel} \approx 20$ GHz, while the one of isopropanol is $f_{rel} \approx 500$ MHz (at room temperature).

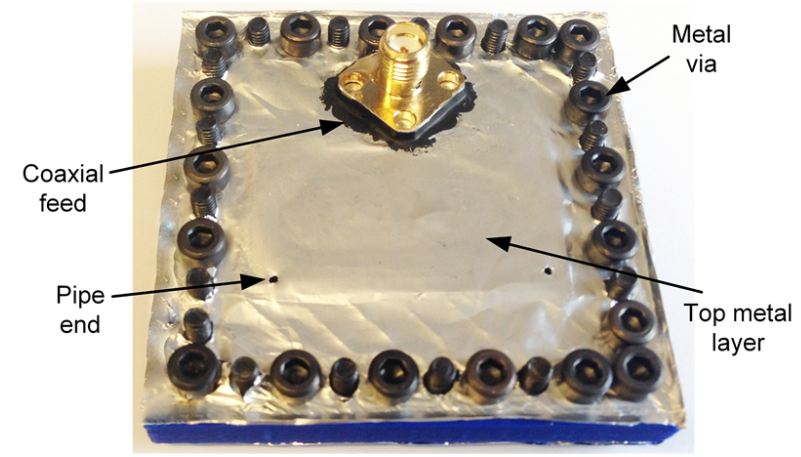

(a)

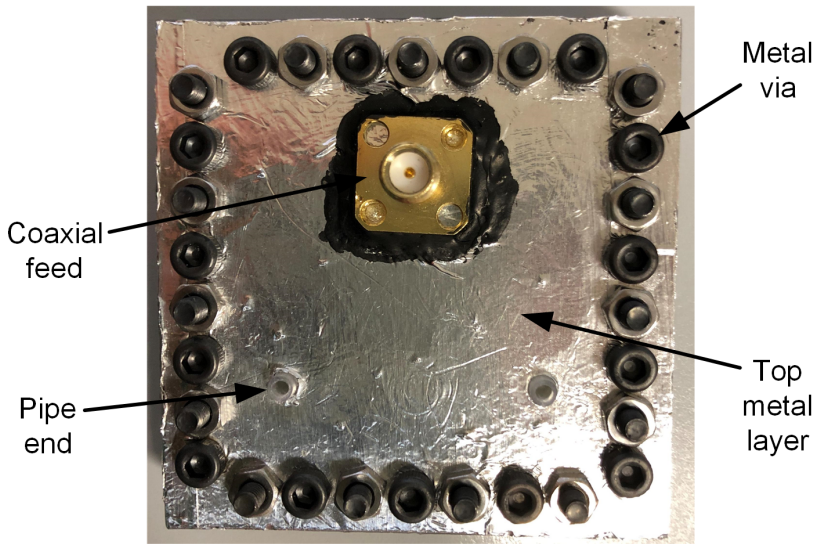

(b)

Figure 3.8: Photographs of the sensors after metallization: (a) first prototype; (b) second prototype.

These characteristics, added to the fact that in both cases the real part of the permittivity monotonically decreases, allowed to make mixtures with dielectric parameters very different from each other, and thus to test the microfluidic sensor in a range of permittivities and loss tangents which varied in a quite wide range.

With this setup, shown in Fig. 3.9(a), the S_{11} of the resonant cavity was measured with a Vector Network Analyzer (VNA). The sensor was connected, with a flexible cable, to a PXIe VNA Keysight M9375A, which performed the measurement of the S-parameter. The analysis was done between 2 GHz to 5 GHz, with the output power set to -20 dBm, to prevent any microwave heating. A pressure-based flow controller by Fluigent was adopted to inject the LUT, with a constant pressure, inside the

pipe (Fig. 3.9(b)). The pressure of the pump was adjusted thanks to the software interface by MAESFLO, which allowed also to stop the injection as soon as the pipe is full.

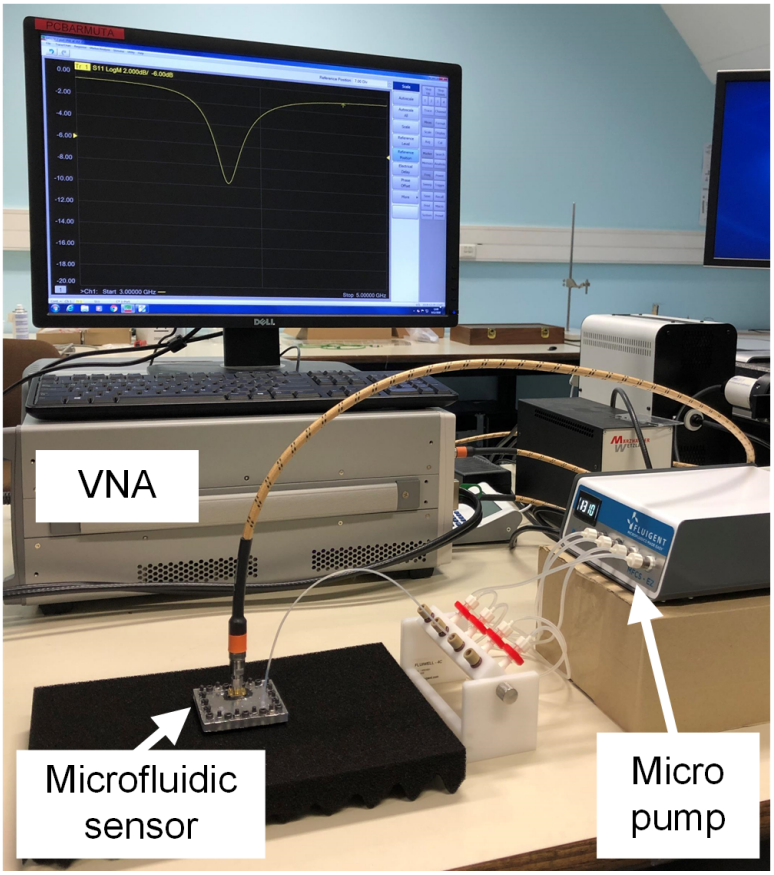

(a)

Figure 3.9: Measurement setups: (a) S-parameter measurements of the sensor (continued on next page).

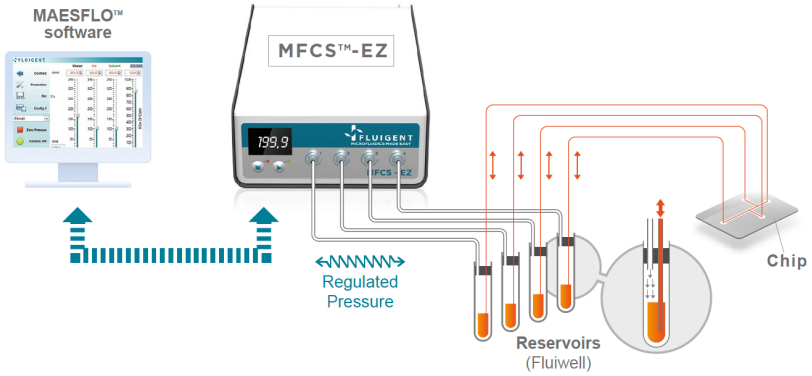

(b)

Figure 3.9: Measurement setups: (b) Schematic setup of Fluigent system with fluid reservoir and connection to the microfluidic device [6].

3.3.1 Results

Thanks to this measurement setup, the scattering parameters S_{11} at the coaxial port of the resonant cavity were measured when different liquids where injected in the pipe.

From the reflection coefficient, both f_0, by taking the minimum of the $|S_{11}|$, and Q_U, by following the procedure described in subsubsection 2.1.2.1, were derived.

First prototype Fig. 3.10 reports the measured S_{11} for three different cases (air, ethanol, water). The resonance frequency of the cavity decreases when increasing the dielectric permittivity of the LUT, from air-filled to water-filled pipe. In particular, it changes from $f_{air} = 4.034$ GHz with empty pipe to $f_{wat} = 3.614$ GHz with water-filled pipe. In addition to the frequency shift, the shape of the $|S_{11}|$ changes when modifying the liquid in the pipe, in accordance with the loss tangent of the LUT. The retrieved values of resonance frequency and Q-factor are reported in Table 3.2.

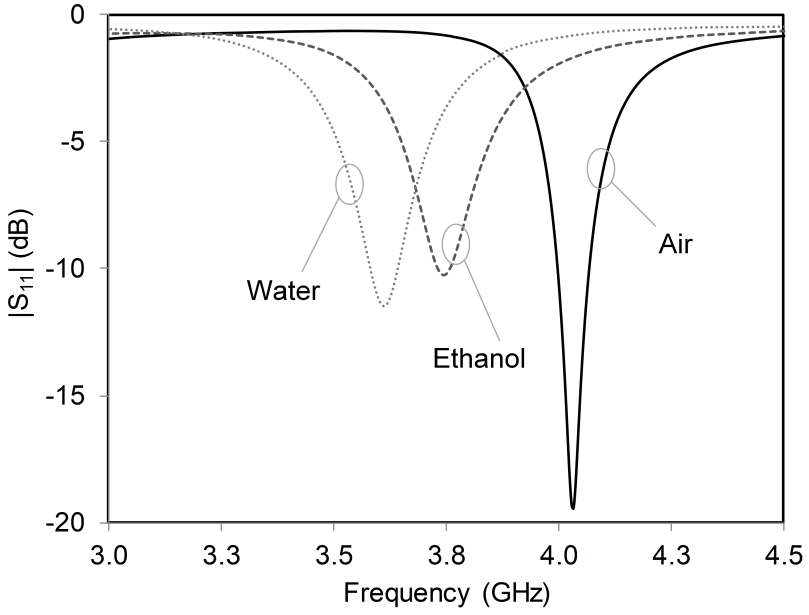

Figure 3.10: Measured scattering parameters for air, pure ethanol and distilled water.

LUT	**Resonance frequency f_0 (GHz)**	**Frequency shift Δf (GHz)**	**Unloaded Q-factor**
Air	4.0340	-	42.6
Ethanol	3.7457	0.2883	18.2
Water	3.6136	0.4204	31.5

Table 3.2: Values of measured resonance frequency, frequency shift (with respect to empty pipe case) and unloaded quality factor when the pipe is filled with the LUTs.

Second prototype In Fig. 3.11 the measured S_{11} of four different cases (air, isopropanol, mixture 85% isopropanol - 15% water, distilled water) is shown. In this cavity, the resonance frequency changed from $f_{air} = 3.827$ GHz with empty pipe to $f_{wat} = 3.408$ GHz with water-filled pipe. The retrieved values of resonance frequency and quality factor are reported in Table 3.3.

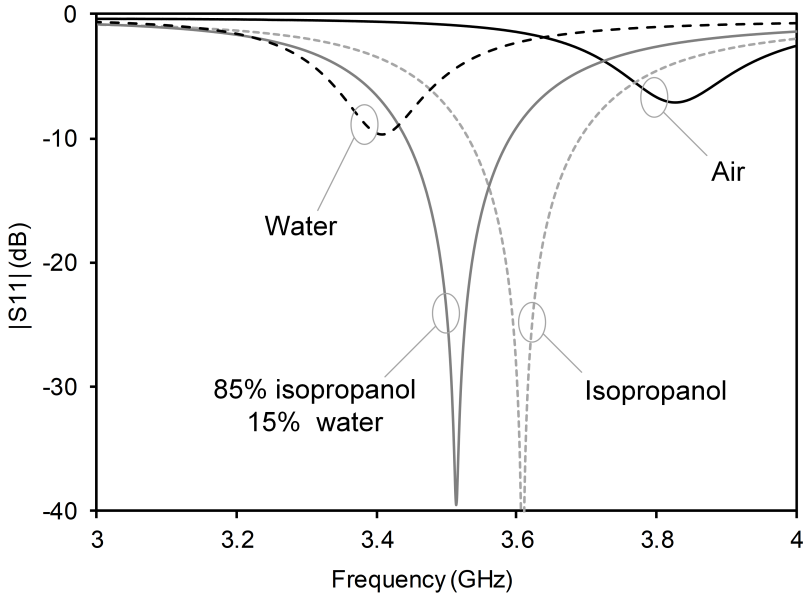

Figure 3.11: Measured scattering parameters for air, isopropanol, mixture 85% isopropanol - 15% water, distilled water.

LUT	**Resonance frequency f_0 (GHz)**	**Frequency shift Δf (GHz)**	**Unloaded Q-factor Q_U^{meas}**
Air	3.8267	0	43.12
Isopropanol	3.6095	0.2172	17.48
Isoprop. 85%/Water 15%	3.5147	0.3120	18.12
Isoprop. 75%/Water 25%	3.4757	0.3510	21.47
Isoprop. 60%/Water 40%	3.4003	0.3793	24.03
Isoprop. 45%/Water 55%	3.4287	0.3980	27.31
Isoprop. 30%/Water 70%	3.4243	0.4024	29.06
Isoprop. 20%/Water 80%	3.4174	0.4093	31.78
Isoprop. 10%/Water 90%	3.4150	0.4117	34.24
Water	3.4077	0.4190	36.73

Table 3.3: Values of measured resonance frequency, frequency shift (with respect to empty pipe case) and unloaded quality factor when the pipe is filled with the LUTs.

3.4 Retrieval of Liquids Dielectric Properties

In this section, only the results relative to the second prototype are reported. The first prototype had indeed two big issues: firstly, the absence of vertical exits for the pipe (added in the second prototype) which, protruding outside the cavity, would have permitted to better keep track of the amount of liquid injected, avoiding it to leaked out and breach into the 20% infill printed substrate. In addition, the ABS printed with 20% infill was not distributed in a homogeneous way, as highlighted by the white dashed ellipse in Fig. 3.12. This made it impossible to run simulation with the exact value for substrate permittivity and loss tangent. For this reason, in the successive prototype, a single material with 100% infill was used, and the pipe was designed to get out from the cavity via two protrusions.

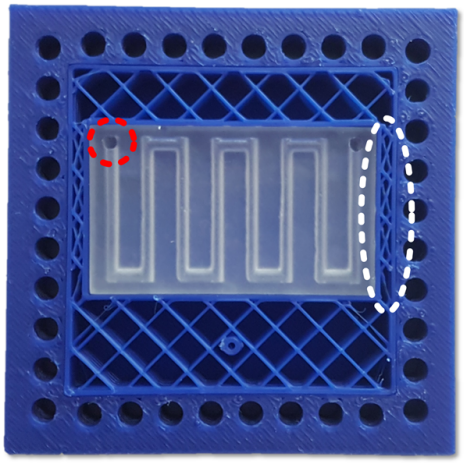

Figure 3.12: First sensor prototype, with highlighted its two major issues: the red dashed line highlights the fact that the end of the pipe dwells inside the cavity itself; the white dashed line, encircles the area where the fill is higher than the expected 20%.

In the following section, the methods developed for the extraction of the liquid dielectric permittivity and loss tangent are presented. The loss tangent is retrieved thanks to a novel method that de-embeds the 3D-printed substrate losses, which could lead to a potential error in the extraction of the LUT loss tangent. This algorithm can be applied for cavity-based microfluidic sensors of whatever shape, as long as one knows the resonance frequency and the quality factor of the cavity.

3.4.1 Dielectric Permittivity Retrieval

First of all, with the aim of extracting LUT's dielectric permittivity from the shift of the resonance frequency, a set of simulations with HFSS was performed. In particular, we considered the pipe filled with liquids having different dielectric permittivity (ε_r

ranging from 1 to 100) and null loss tangent, and, then, we calculated the corresponding frequency shift Δf. These analyses led to the simulation curve shown in Fig. 3.13(a).

With the MATLAB curve-fitting tool, we derived a minimal-error fitting of the simulation results, which relates the dielectric permittivity ε_r of the LUT to the frequency shift Δf. The fitting function has the following expression:

$$\varepsilon_r = \frac{\mathrm{p}_1\Delta f^3 + \mathrm{p}_2\Delta f^2 + \mathrm{p}_3\Delta f + \mathrm{p}_4}{\Delta f^2 + \mathrm{q}_1\Delta f + \mathrm{q}_2} \tag{3.1}$$

where $\mathrm{p}_1 = 14.96$, $\mathrm{p}_2 = -8.889$, $\mathrm{p}_3 = 1.826$, $\mathrm{p}_4 = 0.2086$, $\mathrm{qq}_1 = -0.924$, $\mathrm{q}_2 = 0.2183$ and Δf is expressed in GHz.

The plot in Fig. 3.13(a), or the expression (3.1), permits to retrieve the dielectric permittivity of the LUT once having the value of the measured frequency shift.

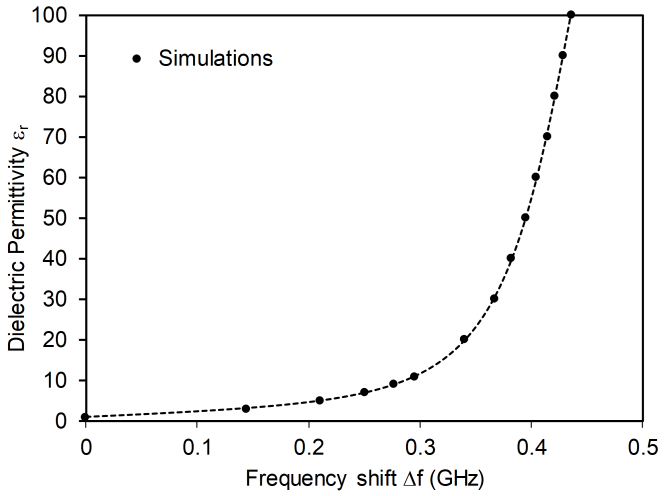

(a)

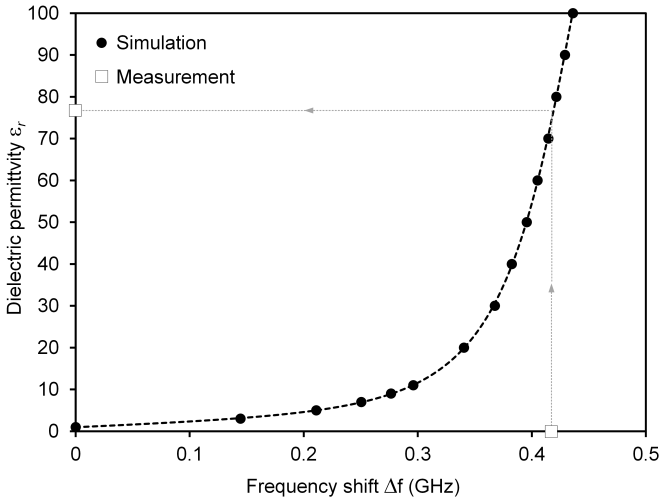

(b)

Figure 3.13: Dielectric permittivity versus the resonance frequency shift: (a) Simulation plot; (b) Simulation plot and experimental validation example for water.

In Fig. 3.13(b) the example of water is reported. When water was injected in the pipe, the measured frequency shift (with respect to the case with empty pipe) was $\Delta f = 0.419$ GHz and thus, according to (3.1) (or the plot in Fig. 3.13(a)), the corresponding permittivity of water was equal to $\varepsilon_r = 76.6$ (square marker in Fig. 3.13(b)). The reference value for the permittivity of water, measured with the coaxial probe, was $\varepsilon_r = 75.6$, thus resulting in a relative error of 1.3%.

This approach was applied to all LUTs and the results are reported in Table 3.4, where the permittivity retrieved by the microfluidic sensor is compared to the reference values obtained with the coaxial probe. While the errors are quite low in the case of water and mixtures with low concentration of isopropanol, they reach unacceptable values for mixtures with high concentration of isopropanol or for pure isopropanol.

LUT	**Microfluidic Sensor**	**Coaxial Probe**	**Relative Error (%)**
Isopropanol	5.24	3.90	+34.2
Isoprop. 85%/Water 15%	13.4	8.04	+67.0
Isoprop. 75%/Water 25%	23.4	14.8	+57.9
Isoprop. 60%/Water 40%	37.5	24.9	+50.9
Isoprop. 45%/Water 55%	52.6	35.3	+48.9
Isoprop. 30%/Water 70%	56.9	49.9	+14.1
Isoprop. 20%/Water 80%	64.5	59.2	+9.00
Isoprop. 10%/Water 90%	67.4	64.9	+3.80
Water	76.6	75.6	+1.30

Table 3.4: Dielectric permittivity retrieved and reference values measured with the coaxial probe.

Novel Method The misstatement in the described approach is the assumption that the resonance frequency of a cavity resonator depends only on the real part of the dielectric permittivity. This condition is valid when losses are small. Viceversa, when dealing with high losses liquids (isopropanol, for example) the imaginary part of the dielectric permittivity (which involves the loss tangent) has to be taken into account, too.

The general formula to calculate the complex resonance frequency f_c in a resonant cavity states that [8]

$$f_c = \frac{k_c}{2\pi\sqrt{\varepsilon\mu}} \tag{3.2}$$

where k_c represents the wavenumber related to the considered cavity resonant mode and ε and μ are the complex values of permittivity and permeability, respectively.

When **lossless** and non-magnetic dielectric materials are considered, the permittivity becomes $\varepsilon = \varepsilon_0 \varepsilon_r$ and the permeability is equal to $\mu = \mu_0$. Hence, (3.2) can be reformulated as

$$f_c = \frac{k_c}{2\pi\sqrt{\varepsilon_0\,\varepsilon_r\,\mu_0}} = \frac{k_c\,c}{2\pi\sqrt{\varepsilon_r}} \tag{3.3}$$

where $c = 1/\sqrt{\varepsilon_0\mu_0}$ is the speed of light in vacuum.

On the contrary, with **lossy** and non-magnetic dielectric materials (which is our case), the permittivity is expressed as $\varepsilon = \varepsilon_0\,\varepsilon_r(1 - j\tan\delta)$, and (3.2) turns into

$$f_c = \frac{k_c\,c}{2\pi\sqrt{\varepsilon_r\,(1 - j\,\tan\delta)}} \tag{3.4}$$

thus showing that also the loss tangent of the material in the cavity has a role in the determination of cavity's resonance frequency.

Initially, we totally ascribed the frequency shift to the dielectric permittivity, and, indeed, the simulations (Fig. 3.13(a)) were performed with $\tan\delta = 0$. If, instead, we take into account the losses, the dielectric permittivity can be retrieved with higher precision.

Knowing that the resonance frequency $f_0 = \mathfrak{Re}\,[f_c]$ and comparing (3.3) and (3.4), a correction factor can be derived, whose value depends both on the dielectric permittivity and the loss tangent.

From (3.3) and (3.4) we get

$$\frac{1}{\sqrt{\varepsilon_r}} \rightarrow \mathfrak{Re}\left[\frac{1}{\sqrt{\varepsilon_r\,(1 - j\,\tan\delta)}}\right] \tag{3.5}$$

By manipulating (3.5) we obtain

$$\varepsilon_r \rightarrow \frac{\varepsilon_r}{2} \cdot \frac{\sqrt{1 + tan\delta^2} + 1}{1 + tan\delta^2} = F \tag{3.6}$$

Essentially, since the shift in the resonance frequency Δf depends both on ε_r and $\tan\delta$, we have to substitute the value of ε_r on the y-axis of Fig. 3.13(b) with the correction factor $F = \frac{\varepsilon_r}{2} \cdot \frac{\sqrt{1+\tan\delta^2}+1}{1+\tan\delta^2}$. Fig. 3.14 reports, in a plot form, the ratio between F and ε_r as function of $tan\delta$. It can be seen how, while $\tan\delta$ increases, the value of F deviates from ε_r, reaching the value of $F = 0.604\,\varepsilon_r$ when $\tan\delta = 1$.

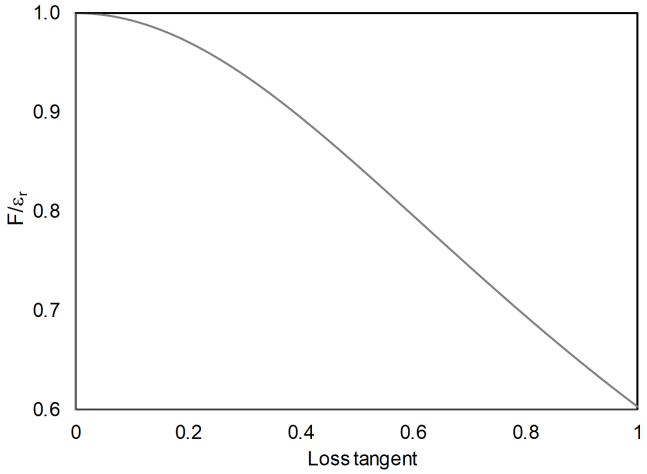

Figure 3.14: Plot of $F\,/\,\varepsilon_r$ as function of the loss tangent.

Thus, once we have the loss tangent (which, as will be explained in subsection 3.4.2, can be extracted from cavity Q-factor) and the Δf, we can obtain the values of ε_r for any LUT. In Table 3.5 these values are compared with the ones extracted through the coaxial probe characterization method. As can be noticed, in all the cases we have a large improvement with respect to table 3.4.

LUT	**Microfluidic Sensor**	**Coaxial Probe**	**% Relative error**
Isopropanol	4.20	3.90	+7.1
Isoprop. 85%/Water 15%	8.60	8.04	+7.5
Isoprop. 75%/Water 25%	16.5	14.8	+11.6
Isoprop. 60%/Water 40%	23.6	24.90	+8.3
Isoprop. 45%/Water 55%	42.0	35.3	+19
Isoprop. 30%/Water 70%	48.9	49.9	-2.1
Isoprop. 20%/Water 80%	59.7	59.2	+0.9
Isoprop. 10%/Water 90%	64.7	64.9	-0.4
Water	75.3	75.6	-0.4

Table 3.5: Dielectric permittivity retrieved by using (3.6) and reference values measured with the coaxial probe.

3.4.2 Loss Tangent Retrieval

The variation of the unloaded quality factor was used to retrieve the loss tangent tanδ of the LUT. By using the values of permittivity retrieved with eq. (3.1) , HFSS simulations were performed for each LUT, by varying the loss tangent from 0 to 5.

In Fig. 3.15 is shown the behaviour of the simulated LUT loss tangent versus the unloaded quality factor $Q_{\mathrm{U}}^{\mathrm{sim}}$. The curve is fitted with the function

$$\tan\delta = \frac{\mathrm{p}_1\, {Q_{\mathrm{U}}^{\mathrm{sim}}}^3 + \mathrm{p}_2\, {Q_{\mathrm{U}}^{\mathrm{sim}}}^2 + \mathrm{p}_3\, Q_{\mathrm{U}}^{\mathrm{sim}} + \mathrm{p}_4}{{Q_{\mathrm{U}}^{\mathrm{sim}}}^2 + \mathrm{q}_1 Q_{\mathrm{U}}^{\mathrm{sim}} + \mathrm{q}_2} \tag{3.7}$$

where p_1 = -0.002965, p_2 = 0.04461, p_3 = 17.92, p_4 = 1.533, q_1 = -12.49, and q_2 = 0.4673.

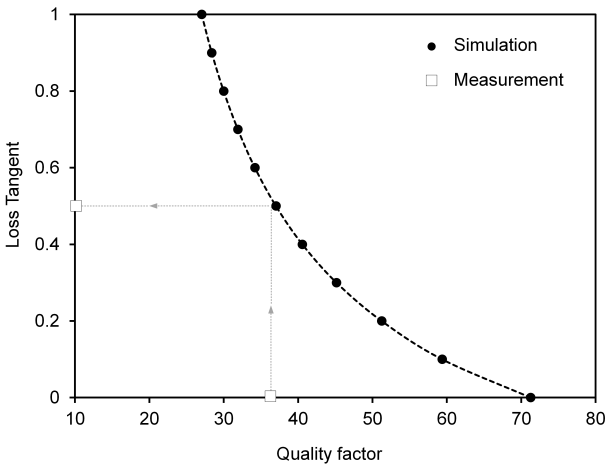

Figure 3.15: Simulated values of the loss tangent versus the unloaded quality factor ($Q_{\mathrm{U}}^{\mathrm{sim}}$), and experimental validation example for water ($Q_{\mathrm{U}}^{\mathrm{meas}}$)

LUT	**Microfluidic Sensor**	**Coaxial Probe**	**% Relative error**
Isopropanol	0.892	0.554	+61.09
Isoprop. 85%/Water 15%	2.360	0.815	+190.67
Isoprop. 75%/Water 25%	2.910	0.775	+275.61
Isoprop. 60%/Water 40%	3.434	0.675	+408.67
Isoprop. 45%/Water 55%	1.636	0.574	+185.04
Isoprop. 30%/Water 70%	1.152	0.451	+155.33
Isoprop. 20%/Water 80%	0.827	0.356	+132.27
Isoprop. 10%/Water 90%	0.660	0.242	+172.65
Water	0.508	0.174	+192.02

Table 3.6: Loss tangent retrieved by using (3.7) and reference values measured with the coaxial probe.

By using the unloaded quality factor $Q_{\mathrm{U}}^{\mathrm{meas}}$ obtained from the measured S-parameters, the loss tangent of the LUT can be retrieved, either from the curve in Fig. 3.15 or from (3.7). In the specific case of water, which is the one reported in the

figure, the unloaded quality factor obtained from measurement was $Q_{\mathrm{U}}^{\mathrm{meas}} = 36.7$. According to (3.7), the corresponding loss tangent of water was $\tan\delta = 0.508$ (square marker). This same approach was applied to all LUTs considered, and the results are reported in Table 3.6, where the loss tangent retrieved by the microfluidic sensor is compared to the reference values obtained with the coaxial probe.

As can be noticed, the discrepancy with respect to the reference values is unacceptably large. The issue is attributed to extra losses and parameter uncertainties in the 3D-printed material, which were not taken into account in the simulation.

We needed to find method to retrieve the correct loss tangent of the LUT, independently of any potential inaccuracies in the determination of the 3D-printed dielectric's characteristics.

Novel Method As regards the simulations, we can write the following expression, that relates the unloaded quality factor of the entire sensor $Q_{\mathrm{U}}^{\mathrm{sim}}$ to the losses in the 3D-printed substrate (described by $Q_{\mathrm{3D}}^{\mathrm{sim}}$) and the losses in the pipe (described by $Q_{\mathrm{liq}}^{\mathrm{sim}}$):

$$\frac{1}{Q_{\mathrm{U}}^{\mathrm{sim}}} = \frac{1}{Q_{\mathrm{liq}}^{\mathrm{sim}}} + \frac{1}{Q_{\mathrm{3D}}^{\mathrm{sim}}} \tag{3.8}$$

From (3.8), the value of $Q_{\mathrm{liq}}^{\mathrm{sim}}$, resulting from liquid losses, can be written as:

$$\frac{1}{Q_{\mathrm{liq}}^{\mathrm{sim}}} = \frac{1}{Q_{\mathrm{U}}^{\mathrm{sim}}} - \frac{1}{Q_{\mathrm{3D}}^{\mathrm{sim}}} \tag{3.9}$$

where $Q_{\mathrm{U}}^{\mathrm{sim}}$ includes also the contribution of the lossy liquid in the pipe, while $Q_{\mathrm{3D}}^{\mathrm{sim}}$ represents just the losses of the 3D-printed structure, and is derived by simulating the sensor with lossless liquid in the pipe (so that losses are due to the 3D-printed material only).

In the hypothesis that the primary cause of error is the poor evaluation of the losses due to the 3D-printed structure, a different methodology to estimate $Q_{\mathrm{3D}}^{\mathrm{sim}}$ needs to be determined. This can be done by considering the measurements: the quality factor $Q_{\mathrm{3D}}^{\mathrm{meas}}$ represents a realistic estimation of the losses in the structure, and can be retrieved from $Q_{\mathrm{U,air}}^{\mathrm{meas}}$, the Q-factor of the resonator with empty pipe. We thus make the following substitution:

$$Q_{\mathrm{3D}}^{\mathrm{sim}} \rightarrow Q_{\mathrm{3D}}^{\mathrm{meas}} = Q_{\mathrm{U,air}}^{\mathrm{meas}} \tag{3.10}$$

It has to be noted that the accuracy of (3.10) is limited by the fact that the presence of liquid in the pipe slightly modify the field distribution with respect to the case with

empty pipe.

At this point, by substituting (3.9) and (3.10) in (3.8), a refined expression of the Q-factor extracted by properly combining simulations and measurements is obtained, and is represented by $Q_{\mathrm{U}}^{\mathrm{sim,ref}}$

$$\frac{1}{Q_{\mathrm{U}}^{\mathrm{sim,ref}}} = \frac{1}{Q_{\mathrm{U}}^{\mathrm{sim}}} - \frac{1}{Q_{\mathrm{3D}}^{\mathrm{sim}}} + \frac{1}{Q_{\mathrm{U,air}}^{\mathrm{meas}}} \tag{3.11}$$

where, on the right hand side, $1\,/\,Q_{\mathrm{U}}^{\mathrm{sim}}$ is related to losses in the LUT, while the other two terms represent the refinement of the losses in the 3D-printed structure, which was applied by replacing the simulated value, $1\,/\,Q_{\mathrm{3D}}^{\mathrm{sim}}$, with the measured one, $1\,/\,Q_{\mathrm{U,air}}^{\mathrm{meas}}$.

By using this method, the curve in Fig. 3.15, which allowed to retrieve the loss tangent from the value of the unloaded quality factor, is modified, turning into the one reported in Fig. 3.16. Here, the grey curve represents the refined version of the black one, because the losses in the 3D-printed material are taken into account. The black markers (corresponding to $Q_{\mathrm{U}}^{\mathrm{sim}}$) have been replaced by the white markers (corresponding to $Q_{\mathrm{U}}^{\mathrm{sim,ref}}$), obtained from (3.11). The measured case of water, where $Q_{\mathrm{3D}}^{\mathrm{sim}} = 71.26$, while $Q_{\mathrm{U,air}}^{\mathrm{meas}} = 43.12$ (Table 3.3), is also reported with the square marker.

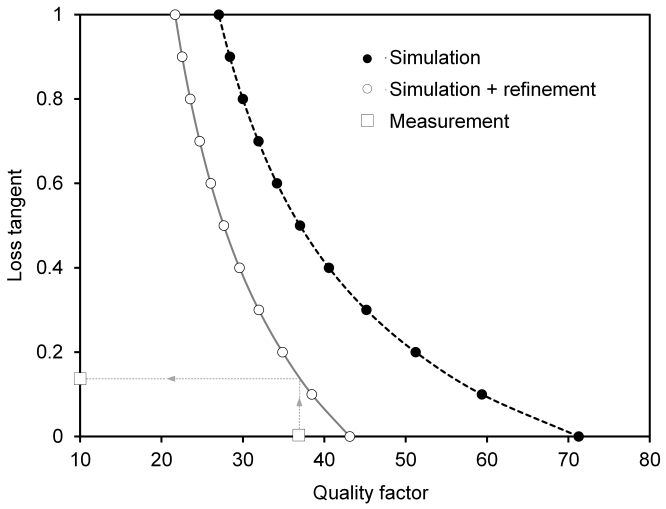

Figure 3.16: Simulated values of the loss tangent versus the unloaded quality factor, with the traditional method ($Q_{\mathrm{U}}^{\mathrm{sim}}$) and the proposed method ($Q_{\mathrm{U}}^{\mathrm{sim,ref}}$), along with the experimental validation example for water ($Q_{\mathrm{U}}^{\mathrm{meas}}$).

The interpolation of the $Q_{\mathrm{U}}^{\mathrm{sim,ref}}$ samples was done with a fitting function whose expression is similar to the one used in (3.7) apart from the coefficients, which in this case are $p_1 = -0.01036$, $p_2 = 0.2325$, $p_3 = 9.03$, $p_4 = 1.609$, $q_1 = -12.42$, and $q_2 = -0.448$.

Thanks to this equation (or by using Fig. 3.16), and to the unloaded quality factor $Q_{\mathrm{U}}^{\mathrm{meas}}$ computed from the measured S-parameters, the loss tangent of the LUTs could

LUT	**Microfluidic Sensor**	**Coaxial Probe**	**% Relative error**
Isopropanol	0.597	0.554	+7.79
Isoprop. 85%/Water 15%	0.910	0.815	+12.03
Isoprop. 75%/Water 25%	0.776	0.775	+0.12
Isoprop. 60%/Water 40%	0.755	0.675	+11.86
Isoprop. 45%/Water 55%	0.594	0.574	+3.49
Isoprop. 30%/Water 70%	0.478	0.451	+6.09
Isoprop. 20%/Water 80%	0.331	0.356	-6.93
Isoprop. 10%/Water 90%	0.238	0.242	-1.61
Water	0.150	0.174	-13.9

Table 3.7: Loss tangent retrieved by using the novel method and reference values measured with the coaxial probe.

be easily retrieved. Let's consider the case of water: since the unloaded quality factor of water was $Q_{\mathrm{U}}^{\mathrm{meas}} = 36.7$, the resulting loss tangent was $\tan\delta = 0.15$, reasonably close to the value obtained with the coaxial probe ($\tan\delta = 0.174$).

This technique was applied to all the other LUTs, and the results are reported in Table 3.7. The accuracy in the determination of $\tan\delta$ is definitely improved, compared to the one shown in Table 3.6, and, in all the cases, the error stays below 13%. The reason for this remaining error is probably due to an imperfect mixing of ISP in water. This, indeed, would lead the liquids characterized with the cavity resonator to have different dielectric parameters with respect to the ones characterized with the probe. Moreover, the reason why the relative errors oscillate, instead of having the same behaviour in all the cases, is related to the way in which the inaccuracies of the measurements (the coaxial probe measurements and the microfluidic sensor measurements) add up.

3.4.3 Error Bars

In order to test the accuracy of the methods used to extract LUTs characteristics, the analysis of the error bars were performed. In Fig. 3.17 the values of dielectric permittivity and loss tangent retrieved from the measurements are compared with the reference values obtained by using the coaxial probe and, for both methods, the corresponding error bars are reported. The grey error bars are relative to the coaxial probe results, while the black ones correspond to the values obtained by using the extraction method in question.

The grey error bars have been generated considering the typical accuracy of the coaxial probe, as reported in the datasheet. Keysight Slim Form Probe's datasheet reports the error in terms of the uncertainty in the real and imaginary parts of the dielectric permittivity. From them, we can get the uncertainty in ε_r and $\tan\delta$:

$$\Delta\varepsilon_r = \pm 0.1\,\varepsilon_r\,|1 - j\tan\delta| \tag{3.12a}$$

$$\Delta\tan\delta = \pm 0.1\,\tan\delta\,|1 - j\tan\delta|\sqrt{\left(1 + \frac{1}{\tan\delta}\right)^2} \tag{3.12b}$$

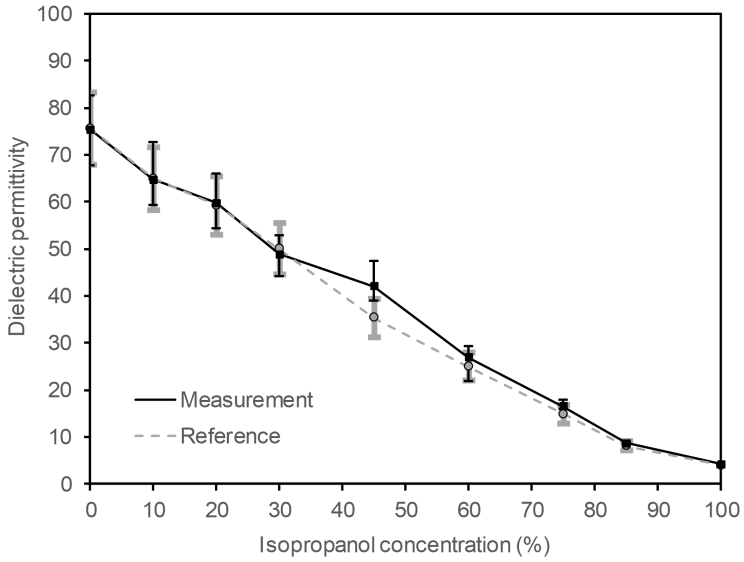

(a)

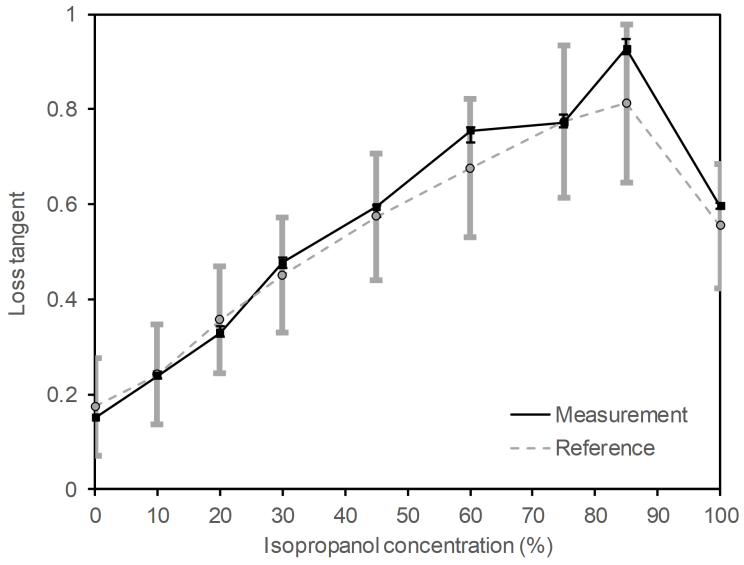

(b)

Figure 3.17: Comparison between the retrieved and reference values of the dielectric characteristics, with error bars: (a) Dielectric permittivity; (b) Loss tangent.

The black error bars, corresponding to the values extracted from the S-parameter measurements, were generated by using the datasheet of the PXIe Vector Network Analyzer, which reports the uncertainty of the reflection coefficient when 85052D standard mechanical 3.5 mm calibration kit is used. From that, an uncertainty of $\pm\,0.0041$ in the value of measured $|S_{11}|$ is indicated in the frequency range of interest (3-5 GHz). This potential error, which could thus have an impact on the value of $|S_{11}|$ at resonance could also, in turn, change the measured Q-factor and resonance frequency. If $|S_{11}|$ changes, the value of the resonance frequency can change, getting either higher or lower, thus generating a variation of the frequency shift and, consequently, giving rise to an inaccuracy in the extraction of the dielectric permittivity. On the other hand, a change in $|S_{11}|$ determines a variation in both the half-power bandwidth and the coupling factor, and, as a result, in the unloaded Q-factor.

In the computation of dielectric permittivity inaccuracy, the contribution of the VNA step size in the measurements can be totally neglected. Let's call by $f(\Delta\mathrm{f})$ the expression

$$\varepsilon_r = \frac{\mathrm{p_1}\Delta\mathrm{f}^3 + \mathrm{p_2}\Delta\mathrm{f}^2 + \mathrm{p_3}\Delta\mathrm{f} + \mathrm{p_4}}{\Delta\mathrm{f}^2 + \mathrm{q_1}\Delta\mathrm{f} + \mathrm{q_2}} = f(\Delta\mathrm{f}) \tag{3.13}$$

and by S the VNA sensitivity, which is equal to

$$S = \frac{5-2}{3201}\left(\frac{\mathrm{GHz}}{\mathrm{points}}\right) = 0.00094\left(\frac{\mathrm{GHz}}{\mathrm{point}}\right) \tag{3.14}$$

since the VNA was set to perform measurements in the frequency range from 2 to 5 GHz and with a number of points equal to 3201. We can now calculate the percentage error in ε_r, by computing:

$$\frac{\Delta\varepsilon_r}{\varepsilon_r}(\Delta\mathrm{f}) = \frac{f(\Delta\mathrm{f}+S) - f(\Delta\mathrm{f})}{f(\Delta\mathrm{f})} \tag{3.15}$$

In Fig. 3.18 is reported the plot obtained by (3.15). As shown, when the step size of the VNA is set to 0.94 MHz, the maximum percentage error in the calculation of the permittivity ε_r is always less than 2%.

In conclusion our method present an uncertainty, in permittivity and loss tangent extraction, which, as shown in Fig. 3.17, is much lower than the uncertainty of the coaxial probe, principally as regards of loss tangent measurements.

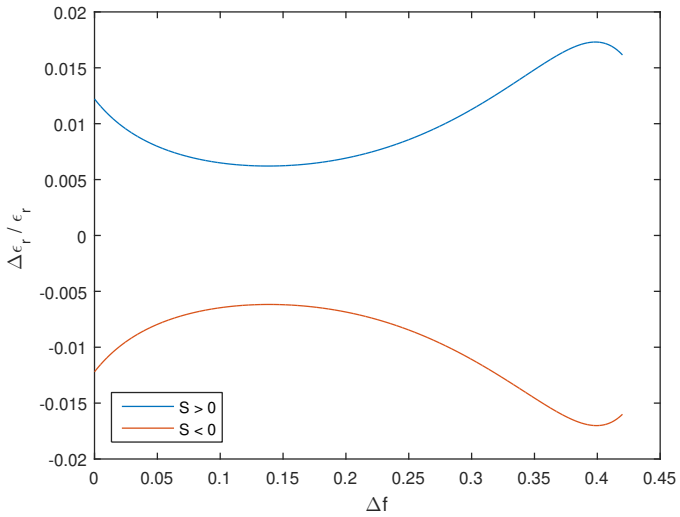

Figure 3.18: Plot of positive and negative error in the dielectric permittivity as function of the frequency, when the sensitivity of the VNA is equal to 0.94 MHz/pt.

3.5 Chapter Summary

In this chapter, two microfluidic sensors, which combine the benefits of 3D-printing and SIW technology, have been fabricated and tested.

The basic structure, common to both sensors, consists in a square SIW resonant cavity with a meandered pipe embedded in it. The differences stay in the materials adopted to print the substrates and in the dimension of the different parts. While in the first prototype two different materials were used (ABS and photopolymer resin), the second prototype was printed by using just the resin; while the first sensor is composed by many parts (an external shell, the inner core made up by ABS 20%, the box with the pipe, four ABS supports for this box), the second one has a cleaner design, with just an external shell and the pipe directly stuck to the bottom of the cavity. Moreover, two vertical protrusion were added to the pipe, making the second version preferable for the accuracy of the measurements.

In the final section, a novel method, used to extract the dielectric characteristics of the liquids, is presented. It allows to retrieve the dielectric permittivity and the loss tangent of the liquid just by using the measured scattering parameter $|S_{11}|$. The novelty of this method consists in the de-embedding of the losses associated to the 3D-printed structure, which constitute a substantial source of error.

Several measurements have been performed, and mixtures of water and isopropanol in different concentration have been made in order to test the efficiency of this extraction method over a wide range of values of dielectric permittivity and loss tangent.

This page is intentionally left blank

References

[1] E. Massoni *et al.*, "3-D Printed Substrate Integrated Slab Waveguide for Single-Mode Bandwidth Enhancement," *IEEE Microwave and Wireless Components Letters*, vol. 27, no. 6, pp. 536-538, June 2017.

[2] C. Tomassoni, R. Bahr, M. Bozzi, L. Perregrini, and M. Tentzeris, "3D Printed Substrate Integrated Waveguide Filters with Locally Controlled Dielectric Permittivity," *46th European Microwave Conference (EuMC2016)*, London, UK, Oct. 3-7, 2016.

[3] G. M. Rocco *et al.*, "3D-Printed Microfluidic Sensor in Substrate Integrated Waveguide Technology," *IEEE MTT-S International Microwave Workshop Series-Advanced Materials and Processes (IMWS-AMP 2018)*, Ann Arbor, USA, 16-18 July 2018.

[4] T. Sato, R. Buchner, "Dielectric relaxation spectroscopy of 2-propanol-water mixtures," *The Journal of Chemical Physics*, no. 10, vol. 118, pp. 4606-4613, 2003.

[5] G. M. Rocco *et al.*, "3D-Printed Microfluidic Sensor in SIW Technology for Liquids Characterization," IEEE Transactions on Microwave Theory and Techniques (under review).

[6] J. P. Roberts, 2013, *Modern Microfluidics via Lab-on-a-Chip*, `https://www.genengnews.com/magazine/213/modern-microfluidics-via-lab-on-a-chip/`, accessed 5 September 2019.

[7] L. F. Chen, C. K. Ong, C. P. Neo, V. V. Varadan, and V. K. Varadan, *Microwave Electronics: Measurement and Materials Characterization*, Hoboken, NJ, USA: Wiley, 2004.

[8] K. Kurokawa, *An Introduction to the Theory of Microwave Circuits*, Academic Press, 1969.

This page is intentionally left blank

Chapter 4

Oscillator based on the 3D-Printed Resonator

The passive structure described in Chapter 3 can be used in the development of an oscillator based on the 3D-printed resonator. In fact, by properly connecting an active circuit to the passive resonator, a reflection-type oscillator can be obtained. This device was designed to get oscillation frequencies strongly dependent on the resonance frequency. The purpose is to estimate the dielectric permittivity of the LUTs by looking at the shift in the oscillation frequency. This platform represents a first step in realizing a complete 3D-printed self-sustained device for liquids characterization.

After a brief introduction on microwave oscillators, the design and the simulations of the active board are presented in detail in section 4.2. Eventually, measurements were performed, and the dielectric permittivity of seven different mixtures was retrieved in section 4.4, demonstrating the validity of the platform for liquids characterization.

4.1 Introduction

The oscillator is the most important component in RF and microwave fields, because it is essential for the generation of high frequency signals [1],[2].

Any oscillator is essentially constituted by a passive resonator and an active network. It is well known that the former, if leaved alone, when subjected to an initial perturbation produces damped oscillations, with a frequency approximately equal to that of the resonance. The production of permanent oscillations, instead, requires that the energy dissipated in each cycle is returned to the resonant circuit. This is accomplished by the presence of an active circuit which, from the point of view of the resonator, appears as a negative resistance that cancels out the resistance

of the resonant circuit (Fig. 4.1(a)).

Another way to think about an oscillator, is to consider it as a positive feedback system that, at frequency f_{osc}, has unitary absolute value for the loop gain and null phase (Fig. 4.1(b)). At this frequency the system has an infinite gain, i.e., there can be an output signal even with a null signal at the input. The frequency f_{osc} is the oscillation frequency of the system.

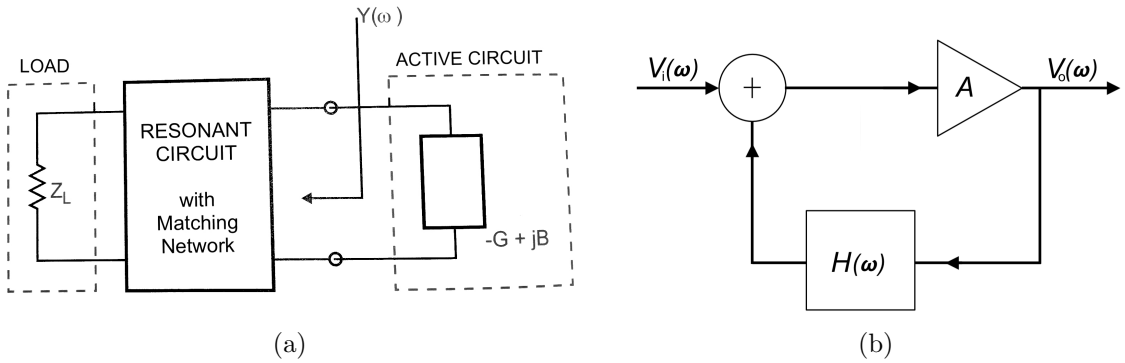

Figure 4.1: Block diagram of an oscillator: (a) negative resistance topology [1]; (b) positive feedback topology [2].

Whatever the adopted point of view is, when the circuit is switched on, any initial perturbation[1] causes the triggering of the oscillations. The oscillations starts to grow, and for small amplitudes the active circuit overcompensates resonator losses. As the amplitude of the oscillation increases, losses compensation is more and more reduced up to the point of equalizing them, obtaining oscillations stable both in amplitude and in frequency.

While at low frequencies basic transistor circuits, in conjunction with crystal resonators, are employed to create oscillators, at microwave frequencies diodes or transistors, biased at a negative resistance operating point, are generally used, producing oscillations up to THz frequencies. Because a nonlinear device is needed, the study and design of an oscillator are nowadays always carried out with CAD tools.

4.2 Design of the Oscillator

In order to explain the operating principle, a simplified diagram of the generator's active circuit is reported in Fig. 4.2 [3].

[1]The initial perturbation can consist in thermal noise or switching-up transistors.

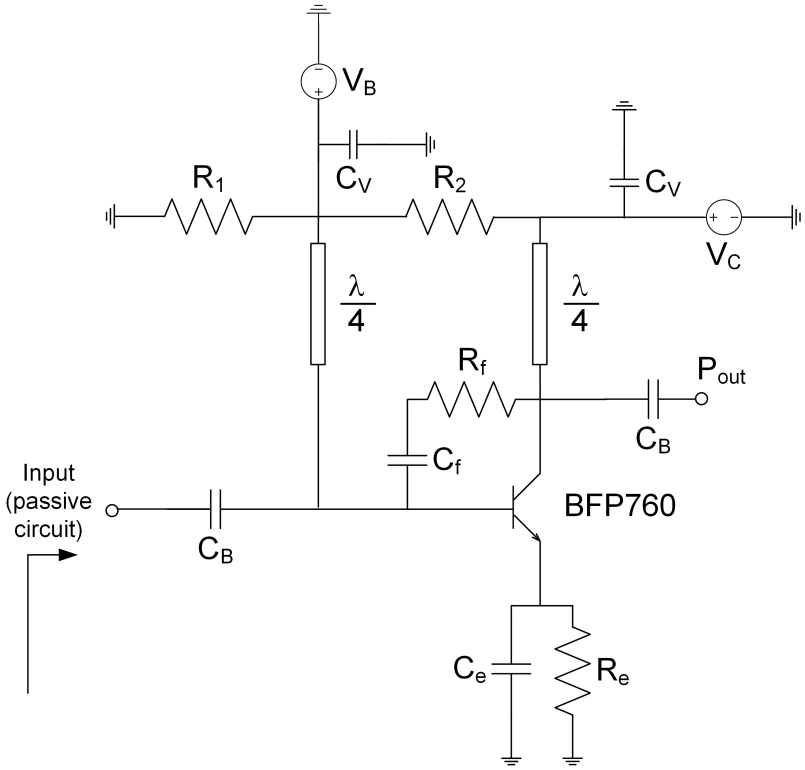

Figure 4.2: Simplified diagram of the active circuit.

The core of the circuit is constituted by R_f and C_f in the feedback loop, by the emitter capacitor C_e and by Infineon BFP760 transistor, which is in common emitter configuration with emitter degeneration. The choice of this particular transistor was dictated by the necessity of having a device with high power gain at the oscillation frequency. The BFP760 bipolar transistor guarantees high gain up to 6 GHz (G_{ms} = 16.5 dB @ 5.5 GHz). Moreover, its transition frequency f_T = 45 GHz make this device particularly suitable for oscillators. R_f, C_f and C_e are the key components to be tuned in order to obtain the desired oscillation frequency.

Resistors R_1 and R_2, together with the emitter resistor R_e, set the proper working point for the transistor, with an emitter current I_C = 30 mA and V_{BE} = 0.8 V. This can also be accomplished by turning on both the voltage supply V_C and exploiting the voltage divider or by directly powering both the collector and the base with V_C and V_B, respectively. High-impedance quarter-wave transmission lines are part of the bias tees, and contribute to isolate the biasing from the RF. Capacitances C_B were used to create DC blocks, while bypass capacitances C_V (they represent the total capacitance of five capacitors in parallel, which have values ranging from 2 pF to 1 μF) were selected to remove high frequency noise originating from the power supplies.

In Table 4.1 the values of all SMD components are reported, together with the value of the biasing voltages.

Parameter	Value	Parameter	Value
R_1	2.7 kΩ	C_e	56 pF
R_2	2.2 kΩ	C_B	30 pF
R_e	62 Ω	C_V	2 pF ÷ 1 μF
R_f	100 kΩ	V_B	2.6 V
C_f	2 pF	V_C	5 V

Table 4.1: SMD components and voltage values in the oscillator design.

RO3006™, a high frequency circuit material belonging to RO3000® series materials (ceramic-filled PTFE laminates provided by Rogers Corp.), was adopted as substrate for the active board. The dielectric parameters of the substrate, that is a dielectric constant equal to 6.5 and a loss tangent of 0.002, allowed to reduce the circuit dimensions as much as possible (compliant to fabrication limits). This helped in making the circuit as compact as possible, in view of creating a handheld device.

Before simulating the circuit, some steps were required. Firstly, the *S*-parameters of the board connectors, as well as that of the right angle connector used to connect the cavity resonator to the active board, needed to be determined. It is important, indeed, to take into account their phase contribution, in order to get a more accurate computation of the oscillation frequency. While the *S*-parameters of the right angle connector can be easily obtained by connecting it to a VNA, the procedure for the characterization of the board connectors takes more efforts. To get the insertion loss of those connectors, two transmission lines with different lengths were designed, fabricated and measured (Fig. 4.3). Starting from the measurements of their *S*-parameters, and in order to extract the insertion loss related to the connectors, an algorithm based on the so called *Through-Line De-embedding Technique* was used [4].

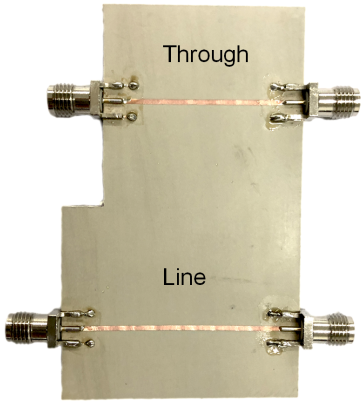

Figure 4.3: Photo of the board used to characterize the connectors through the *Through-Line De-embedding Technique*.

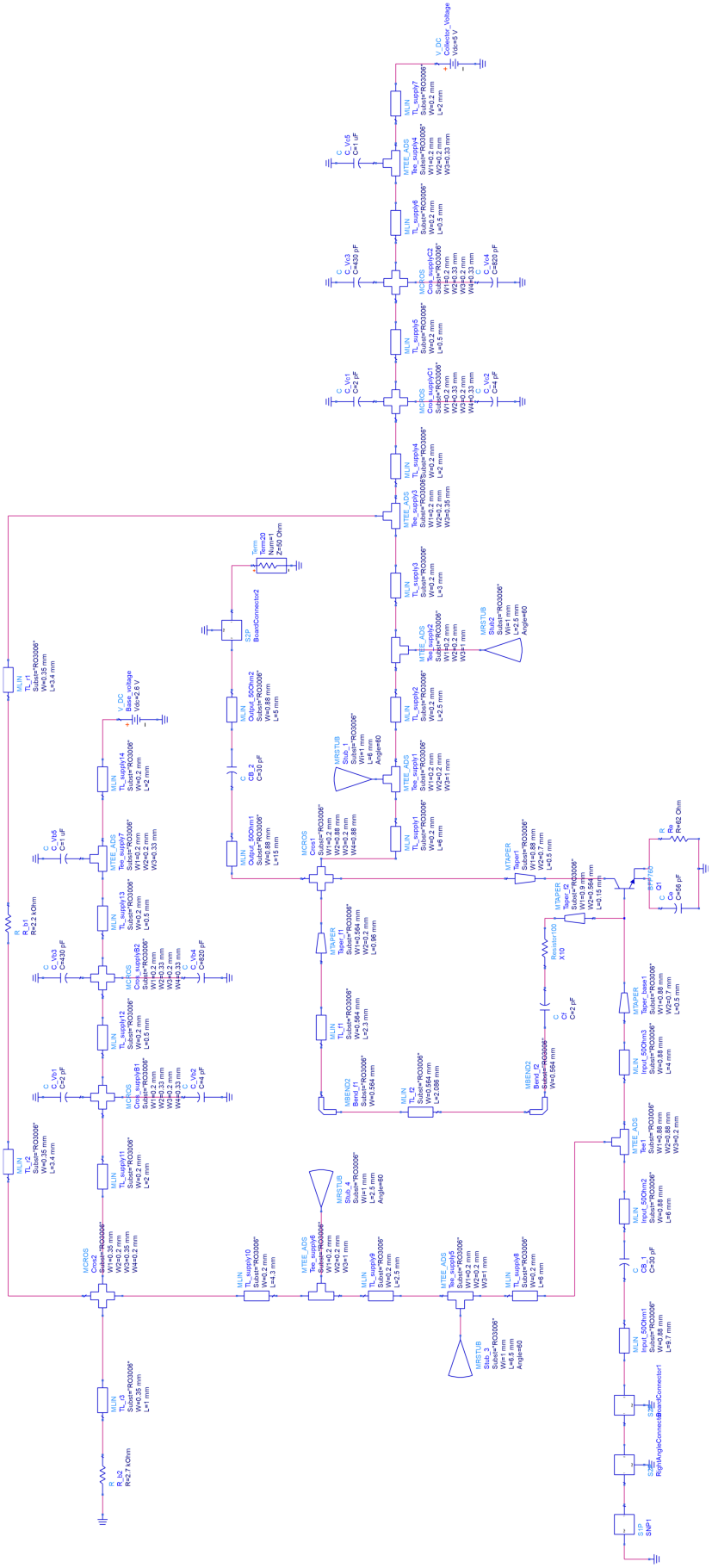

Figure 4.4: ADS schematic of the active circuit with transmission lines.

4.2.1 Simulations of the Oscillator Circuit

Once the S-parameters of all the connectors have been obtained, both these and the S_{11} resulting from the cavity resonator measurements were imported in Keysight ADS. Finally, Harmonic Balance (HB) analysis was used to optimize the oscillator circuitry, in order to find a stable oscillating solution at the desired frequency.

In Fig. 4.4 the schematic of the active circuit, made with ADS, is reported. All the dimensions of the microstrip lines are reported, as well as - inside the S2P blocks - the information about attenuation and phase delays measured for the board connectors and the right angle connector.

Fig. 4.5 shows the results of HB analysis in two cases: when the microfluidic sensor has empty pipe and when it is water-filled. As shown, in the former case the generated fundamental tone has a frequency of 4.033 GHz, with output power $P_{out} = 11.035$ dBm; when water is injected in the pipe, instead, the fundamental tone moves downwards to 3.864 GHz, with an output power $P_{out} = 10.976$ dBm. In both cases the power of the harmonics (just 4 of them are shown, to not overload the figure) is less than -15 dBc.

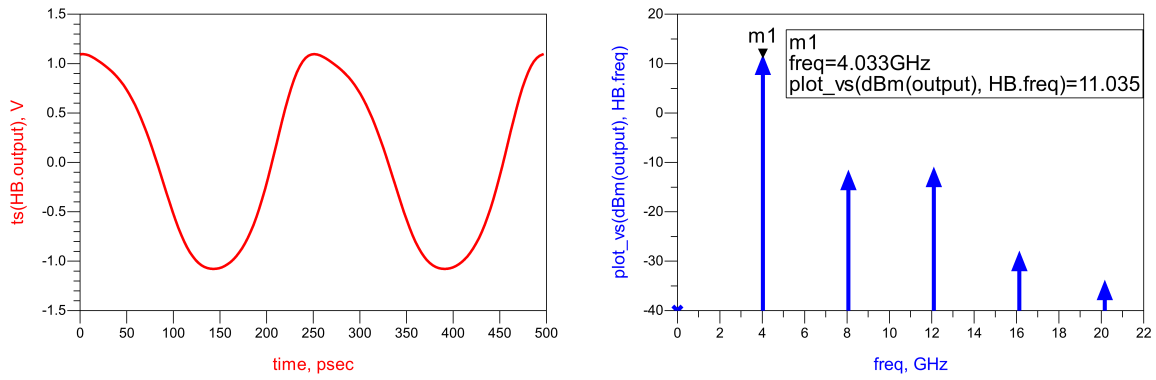

(a)

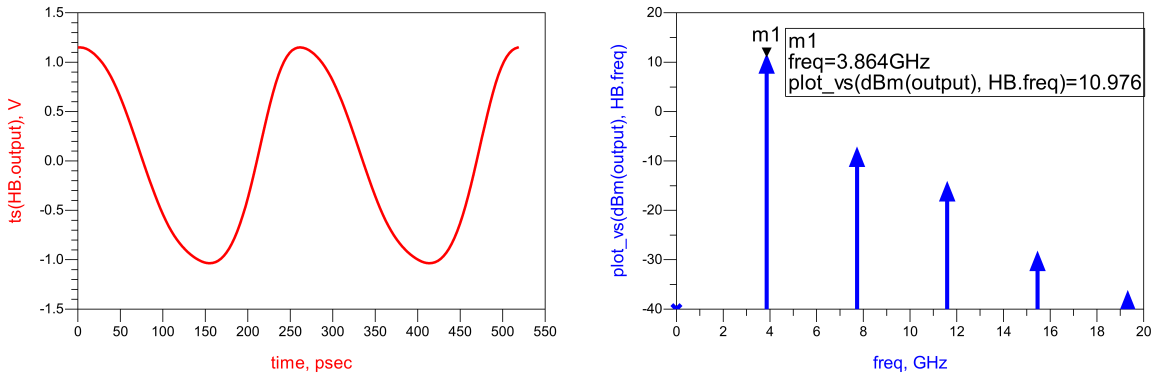

(b)

Figure 4.5: HB simulations results in time and frequency domain: (a) with air-filled microfluidic sensor at the input; (b) with water-filled microfluidic sensor at the input.

Fig. 4.6 reports the results of simulations performed with HB analysis, where the dielectric permittivity ε_r of the LUT injected in the pipe (extracted through coaxial probe method) is plotted with respect to the shift of the oscillation frequency Δf[2]. An exponential function has been used to fit the simulations data, which is represented by the dotted curve. Its equation is

$$\varepsilon_r = a\, e^{b\Delta f} + 1 - a \tag{4.1}$$

where $a = 0.04284$ and $b = 44.0723$. This particular function has been chosen because it passes exactly through the point with coordinates (0;1), which represents the empty pipe case.

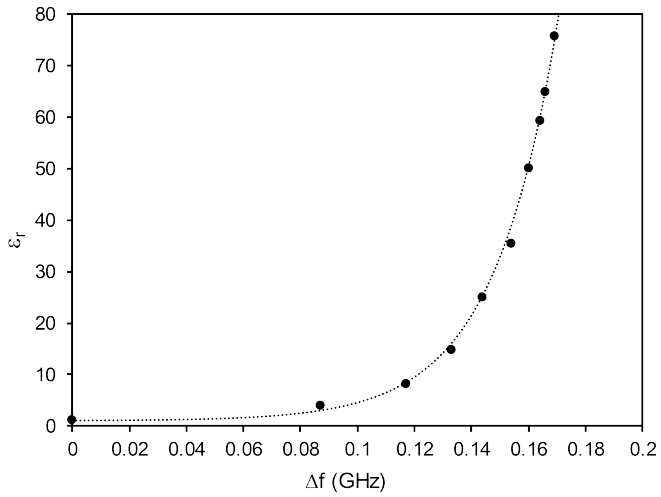

Figure 4.6: Plot of simulation results. The dielectric permittivity, obtained with the coaxial probe method, is reported as function of the shift in the oscillation frequency.

[2]The shift, as always, is calculated with respect to empty pipe case.

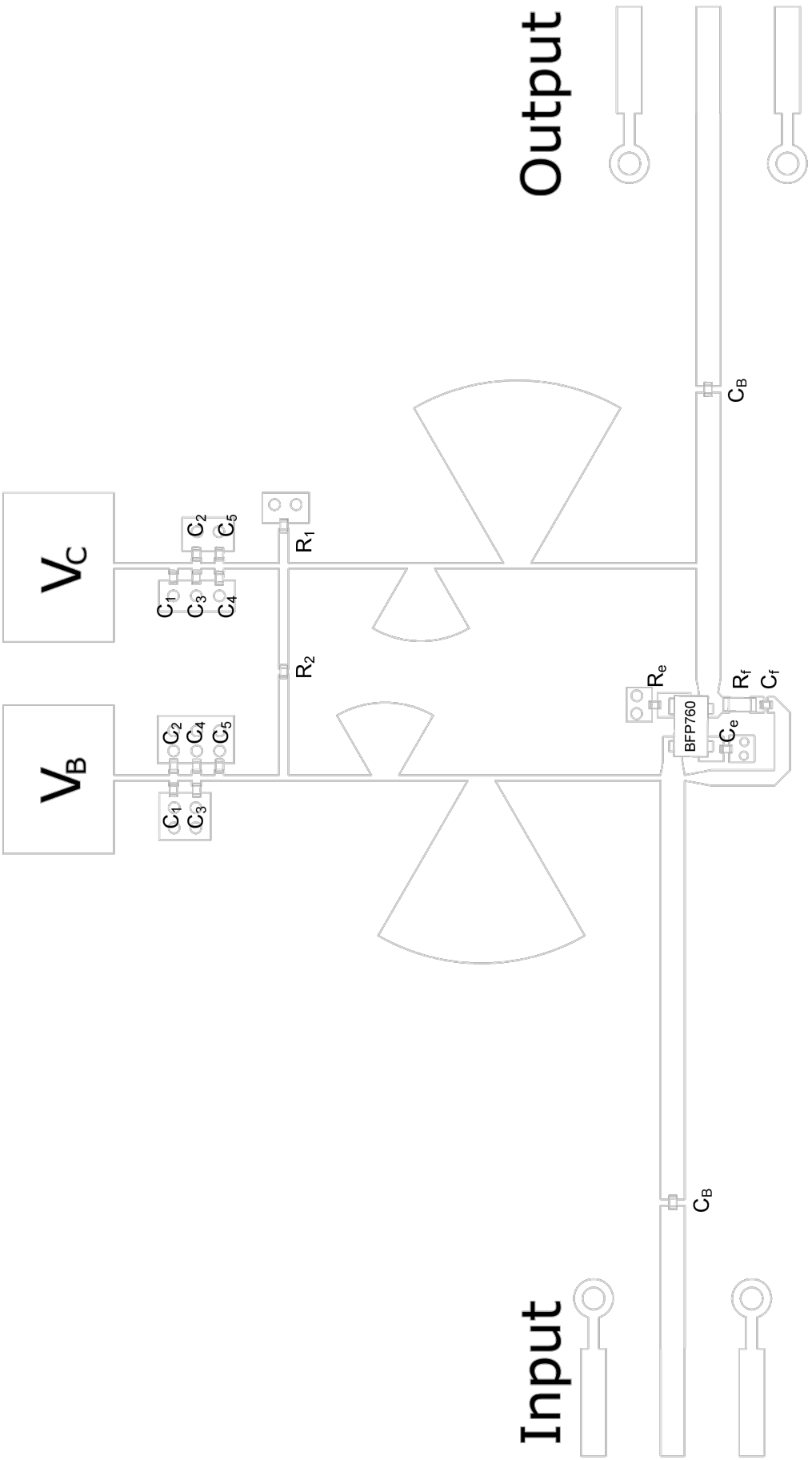

Figure 4.7: Layout of the oscillator active circuit. From the bottom: $C_f = 2$ pF, $R_f = 100$ Ω, $C_e = 56$ pF, $C_B = 30$ pF, $R_e = 62$ Ω, $R_2 = 2.2$ kΩ, $R_1 = 2.7$ kΩ, $C_5 = 2$ pF, $C_4 = 4$ pF, $C_3 = 430$ pF, $C_2 = 820$ pF, $C_1 = 1$ uF.

4.3 Fabrication of the Generator Board

In Fig. 4.7, the layout of the oscillator active board, created with ADS, is reported. The housing of the SMD components is 0201 [in], with the exception of the resistor in the feedback, which has 0402 [in] case (100 Ω high frequency resistors were available only in 0402 - or larger - size cases).

Fig. 4.8 shows a 3D sketch of the generator core part, while, in Fig. 4.9, a photograph of the complete oscillator is reported.

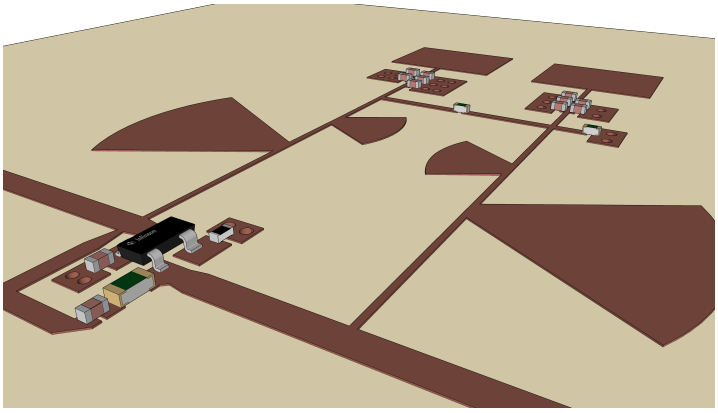

Figure 4.8: 3D view of the central part of the generator board.

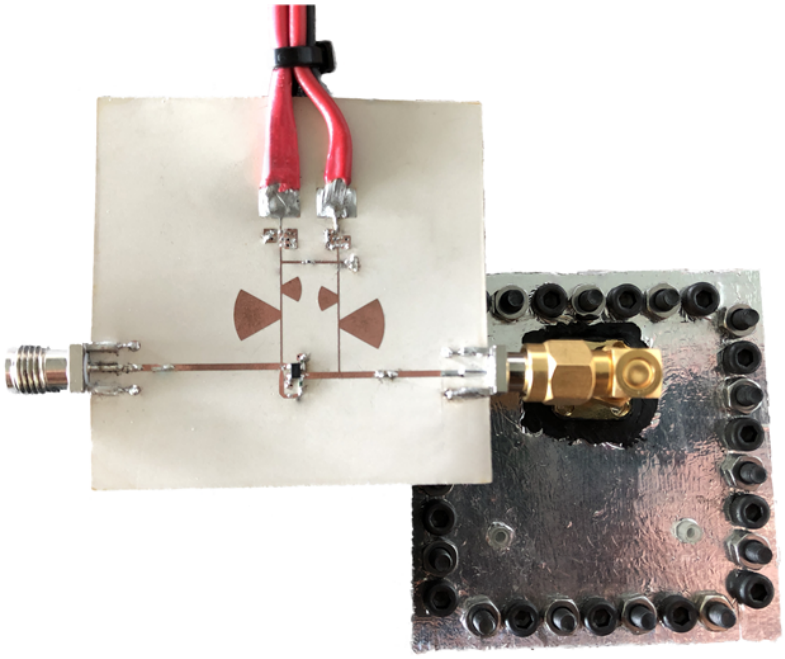

Figure 4.9: Photograph of the oscillator circuit.

4.4 Measurements of the Oscillator Circuit

The measurement setup is based on the spectrum analyzer Keysight N9344C Handheld Spectrum Analyzer (HSA), operating over the frequency range from 1 MHz to 20 GHz. As shown in Fig. 4.10, the output of the oscillator board is connected to the HSA through a flexible coaxial cable. The board, in this case, is powered by using two voltage supplies $V_C = 5\text{V}$ and $V_B = 2.6$ V.

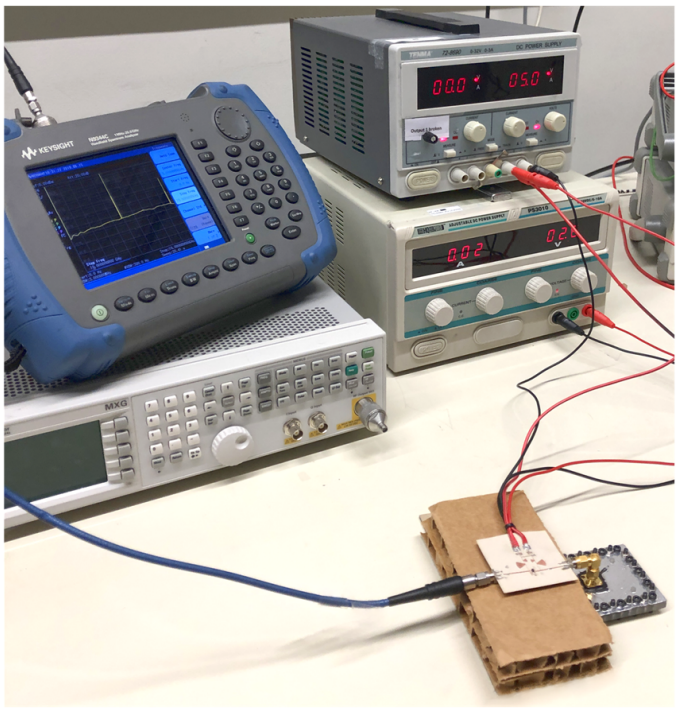

Figure 4.10: Setup for oscillator measurements.

Digital multimeters were also used to simultaneously control the values of collector voltage and current, and a collector current of 29.8 mA was measured with $V_C = 5.036$ V.

4.4.1 Results

The first measurement was done in a large frequency range (from 0.5 GHz to 20 GHz) and with empty sensor pipe. As expected, just a fundamental tone around 4 GHz is present, with its harmonics having lower powers.

Successively, measurements with isopropanol, water and all the mixtures already considered in Chapter 3 were performed. The results obtained with the SA are reported in Fig. 4.12. As expected, the oscillator fundamental tone's frequency shifts downwards as the permittivity of the LUT increases.

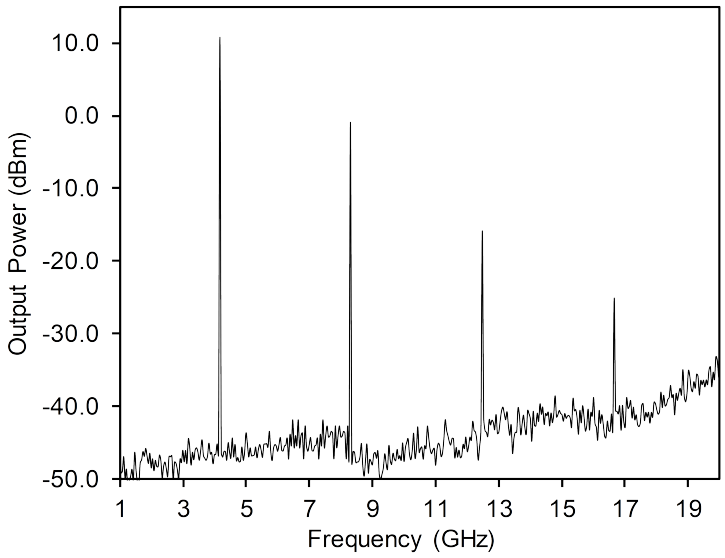

Figure 4.11: Plot of measured generator power when the microfluidic pipe is empty.

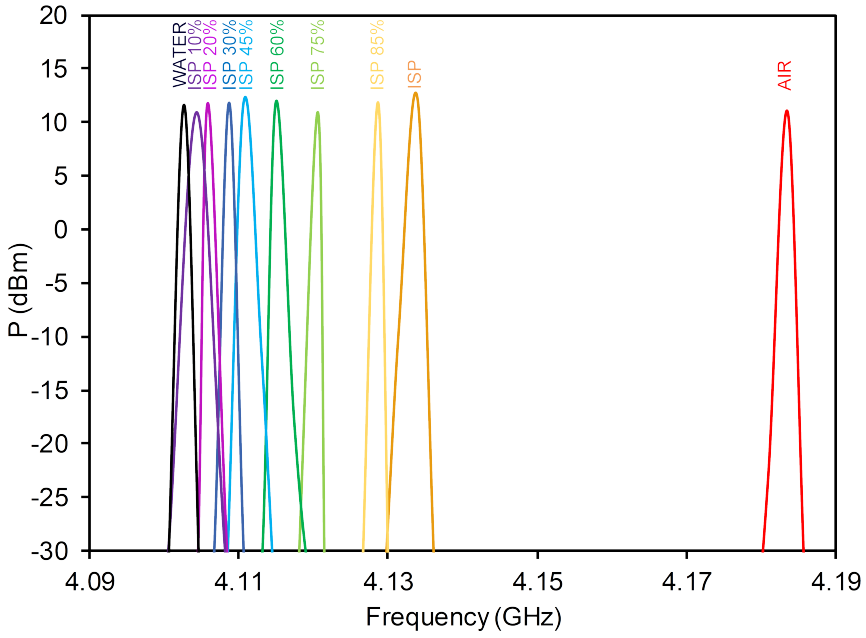

Figure 4.12: Measured generator power when the microfluidic pipe is filled with different liquids.

The purpose of this platform is to retrieve the dielectric permittivity of the LUTs. To do that, a calibration is needed, first. Two liquids - in addition to air - were chosen for the calibration, since their permittivity at microwave frequencies is very well known in literature. In Fig. 4.13, these three measurements are represented by the black square markers. They are used to create an exponential fitting function, represented by the solid grey line, whose equation is the same as (4.1), with parameters $a = 0.0223$ and $b = 100.3$.

By using this function, and knowing the Δf from the measurements, the dielectric permittivity ε_r can be extracted for all the mixtures under test. In order to represent these extracted values, small dot markers have been used, while the diamond markers represent the values of permittivity retrieved from coaxial probe measurements.

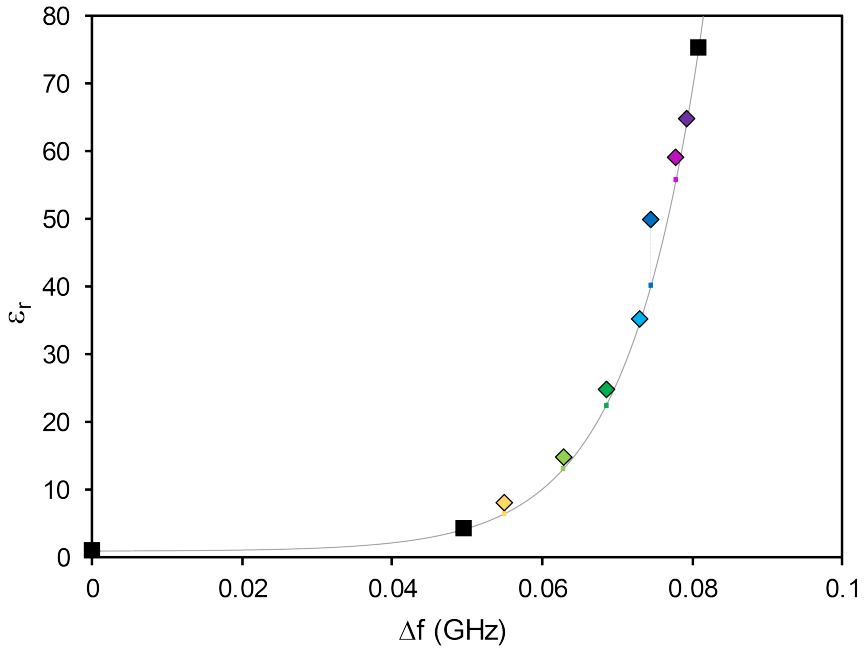

Figure 4.13: Measurements results used for calibration (black square markers) and extracted values of permittivity (dot markers) compared with the reference values (coloured diamond markers).

Table 4.2 compares the retrieved values of permittivity ε_r with the ones measured with the coaxial probe.

LUT	Δf **(GHz)**	**Oscillator** ε_r	**Coax. Probe** ε_r	**Error (%)**
Isoprop. 10%/Water 90%	0.0792	63.82	64.9	-1.67
Isoprop. 20%/Water 80%	0.0777	55.04	59.2	-7.03
Isoprop. 30%/Water 70%	0.0745	40.20	49.9	-19.44
Isoprop. 45%/Water 55%	0.0730	34.72	35.3	-1.65
Isoprop. 60%/Water 40%	0.0686	22.68	24.9	-8.92
Isoprop. 75%/Water 25%	0.0629	13.23	14.8	-10.61
Isoprop. 85%/Water 15%	0.0549	6.47	8.04	-19.53

Table 4.2: Dielectric permittivity extracted by using (4.1) compared with reference values measured with the coaxial probe.

The negative sign in all errors is attributed to the ambient temperature difference between coaxial probe and oscillator measurements. Moreover, the larger error in some mixtures (ISP 30%/water 70% and ISP 85%/water 15%) is probably due to the imperfect mixing of the ISP in the water, which brings the liquid sample characterized with the sensor to be slightly different to the one characterized with the coaxial probe.

4.5 Chapter Summary

In this chapter, an oscillator based on the 3D-printed cavity resonator is presented. The circuit represents a first step in realizing a complete system for the detection of liquids' permittivity in a cheap and simple way. It was enough to perform just three measurements - with air and two known liquids (isopropanol and water) - which were used as calibration, to plot the fitting curve relating dielectric permittivity and shift in the oscillation frequency. At that point, by using the measured frequency shift and the fitting curve, the dielectric permittivity corresponding to all the seven different LUTs considered was extracted. These values were then compared to the ones extracted by coaxial probe method, and the differences were reported and discussed.

This page is intentionally left blank

References

[1] D. M. Pozar, *Microwave Engineering*, John Wiley & Sons, 2005.

[2] R. Sorrentino, G. Bianchi, *Ingegneria delle microonde e radiofrequenze*, McGraw-Hill, 2014.

[3] G. M. Rocco, P. Barmuta, D. Schreurs, and M. Bozzi, "A Novel Platform to Develop 3D-Printed Sensors for Dielectric Permittivity Measurements," *IEEE Microwave and Wireless Components Letters* (under review).

[4] K. W. Eccleston, "A New Interpretation of Through-Line Deembedding," *IEEE Transactions on Microwave Theory and Techniques*, vol. 64, no. 11, pp. 3887-3893, Nov. 2016.

This page is intentionally left blank

Chapter 5

3D-Printed Pumpkin Microfluidic Sensor

In Chapter 3, a 3D-printed microfluidic sensor based on square resonator was presented. Already in that case, the potential of AM has been exploited, in creating a cavity mostly empty and with a multi-folded pipe directly printed inside. In this chapter, that potential is definitely taken to an upper level: a pumpkin-shape resonator, realized through stereolithography technology, is presented. A narrow pipe, passing by one of the structure's symmetry axis, is printed, too, and contributes in making this device a good microfluidic sensor. The reason of choosing such a shape, is that this kind of resonators (in general, the spherical-like shaped resonators) have the peculiarity, when compared to rectangular or cylindrical cavities, of possessing the highest quality factor (with equal wall material).

After a brief introduction on microwave spherical resonators, the design of the cavity is presented in detail in section 5.2. The simulations, performed with the software Ansys HFSS, allowed to optimize the structure, which was consequently fabricated (section 5.3). Eventually, in section 5.4 measurements results are reported: the dielectric permittivity and loss tangent of nine different mixtures were retrieved by using the same approach described earlier in section 3.4.

5.1 Introduction

It was in nineteenth century that, for the first time, the concept of spherical resonator appeared in physics [1]. In 1860 a german physicist, Hermann von Helmholtz, conceived spherical resonant cavities, that were intended to study the sound and its perception (Fig. 5.1). They consisted of hollow spheres, with two

openings on the surface: one with sharp-cut edges, and the other with a cone shape, which was intended to be inserted into the ear. By using more resonators, each having a specific resonance frequency, the harmonics of a given fundamental sound can be easily distinguished. Moreover, it was Helmholtz itself to analytically demonstrate the dependency of the resonance frequency on the cavity volume.

Figure 5.1: Close-up view of two small Helmholtz resonators [2].

In the same period, James Clerk Maxwell wrote his famous paper entitled *Electromagnetic Theory of Light*, where he obtained a wave equation with a speed equal to the speed of light (and Helmholtz demonstrated its validity). Since then, within a few years, the earliest microwave boundary problems were analyzed. One of them, was the study of electromagnetic oscillations within a spherical cavity [3]. In spite of that, spherical-shape resonator, due to the difficulty of fabrication, remained essentially unused for more than a century in microwave engineering.

Today, thanks to AM techniques, many complex-shape devices have been realized, and, even in microwave field, spherical-like geometry is used a lot - especially in filters - due to the high quality factor of these cavities [4], [5].

5.2 Design of the Pumpkin Microfluidic Sensor

The design of the present microfluidic sensor started from the idea of exploiting the high quality factor typical of spherical cavities. From the theory, we know that the field configurations supported by such a structure are the TE^r and/or the TM^r [6]. The expression of the resonant frequencies for the TE^r modes are given by

$$(f_r)_{mnp}^{TE^r} = \frac{\zeta_{np}}{2\pi a\sqrt{\mu\varepsilon}} \qquad \begin{cases} m = 0, 1, 2, ... \leq n \\ n = 1, 2, 3, ... \\ p = 1, 2, 3, ... \end{cases} \tag{5.1}$$

where ζ_{np} represents the p zeros of the spherical Bessel function of order n and a the radius of the sphere. As regards the TE^r modes, instead, the resonance frequencies are calculated as

$$(f_r)_{mnp}^{TM^r} = \frac{\zeta_{np}^{'}}{2\pi a\sqrt{\mu\varepsilon}} \qquad \begin{cases} m = 0, 1, 2, ... \leq n \\ n = 1, 2, 3, ... \\ p = 1, 2, 3, ... \end{cases} \tag{5.2}$$

where $\zeta_{np}^{'}$ represents the p zeroes of the derivative of the spherical Bessel function of order n.

In both (5.1) and (5.2), the resonance frequency expression is independent of the values of m, which means that there exist numerous degeneracies (same resonant frequencies) among the modes.

Let's now consider the fundamental mode of an air-filled spherical cavity resonator (our starting case), that is, the TM_{011} mode. Fig. 5.2 shows the field patterns for the TM_{011} existing inside a hollow spherical resonator constituted by a tiny shell of photopolymer resin.

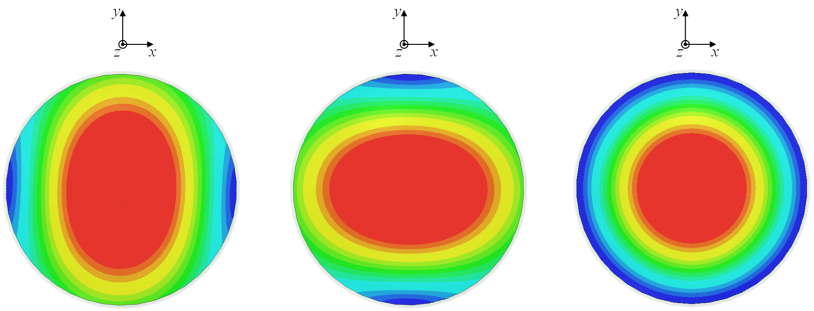

(a)

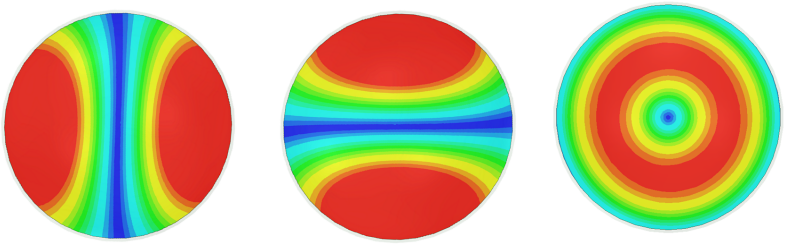

(b)

Figure 5.2: TM_{011} mode field patterns inside an air-filled spherical cavity resonator having a thin dielectric shell and PEC boundary: (a) Electric field amplitude of the three degeneracies; (b) Magnetic field of three degeneracies.

As shown in Fig. 5.2(a), the fundamental mode reaches its maximum in parallel, respectively, to x, y or z axis, depending on the degeneracy considered. By aligning the pipe to one of these axes, where the first mode presents its maximum, we will get the biggest impact on the mode's frequency.

Before getting to the final design of the sensor, one more step was made. As already said, the peculiarity of a symmetrical structure, like the spherical resonator, is to have three modes (degeneracies) at the *same frequency*. This can be kind of a problem, because if the degeneracies have the same resonance frequencies, it is impossible to distinguish what is the first mode when the LUTs is injected in the pipe. Of course, the symmetry is slightly broken when the pipe is inserted in the structure. In any case, due to the thin walls of the pipe, when the empty-pipe case is considered, it can be very difficult to distinguish the first degeneracy from the higher ones. For this reason, a rip in the symmetry is introduced by squeezing the sphere at the two poles, along the z axis, as shown in Fig. 5.3(a). This brings the first degeneracy, which have the maximum electric field in that direction, to split apart, in frequency, from the other modes.

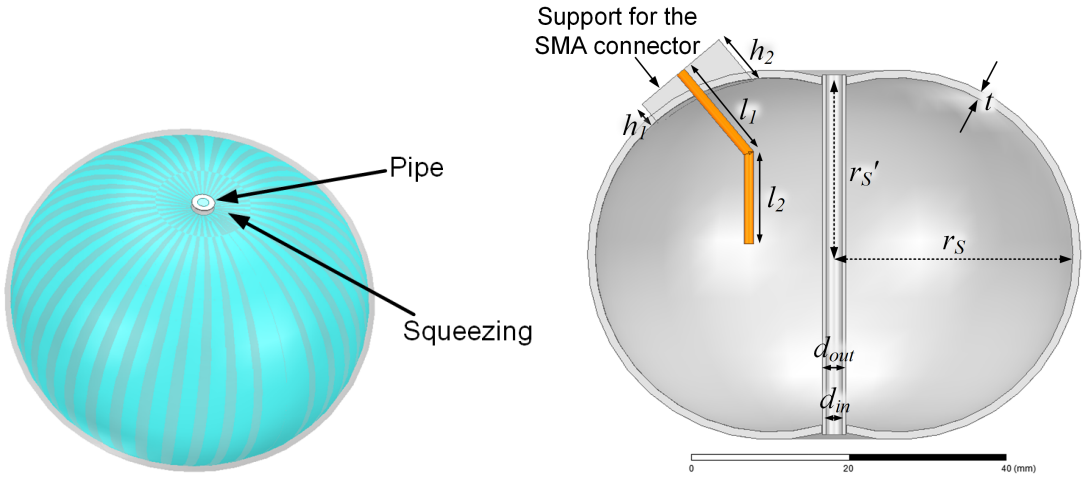

(a) (b)

Figure 5.3: Cavity resonator design: (a) the sphere was slightly squeezed at the poles, to increase the distance in frequency between the degeneracies of the fundamental mode; (b) Design dimensions indicated (in mm): $d_{in} = 2$; $d_{out} = 3$; $r_S = 23$; $r_S^{'} = 22$; $l_1 = 14$; $l_2 = 13$; $t = 2$.

Fig. 5.3(b) shows the final design, realized with HFSS. As explained before, $r_S^{'}$ was specifically designed to be lower than r_S, with the aim to increase the distance in frequency between first and higher modes. In order to determine the optimum value for $r_S^{'}$, we started from the spherical cavity with empty pipe: it can be calculated that the radius that this structure needs in order to have the resonance frequency at

4.3 GHz is $r_S = 30$ mm ($r_S^{'} = 30$ mm). We then started to decrease $r_S^{'}$ and, in order to maintain the resonance frequency of the first mode at the original frequency, $r_S^{'}$ was also decreased. Of course, the more r_S (and $r_S^{'}$) value is reduced, the larger is made the difference in frequency between the first mode and the upper ones. However, while decreasing the value of r_S, the Q-factor of the cavity also drops. Thus, we stopped the reduction of r_S until a difference of 500 MHz between the first mode and the upper ones was obtained, that is, when $r_S = 23$ mm and $r_S^{'} = 22$ mm.

The dimensions of the pipe (its inner diameter and the thickness of the wall) were constrained by some difficulties arose during the manufacturing. In particular, the challenge consisted in realizing a pipe that, while maintaining its patency, could be long enough to protrude, at least a centimetre, outside the cavity. In fact, in all the attempts we made trying to reduce the inner diameter of the pipe below 2 mm, it always happens that parts of the pipe were occluded by resin. The only way to avoid occlusions would have been to reduce the length of the pipe - equal to 66 mm - of a half, but this was not possible, because in that case the pipe would have been shorter than the sphere diameter. In essence, a trade-off was present between the pipe's inner diameter and its length, and it was dictated by manufacturing considerations.

In Fig. 5.3(b) it can also be noted, in orange, the pin for the feed, which is constituted by two parts. This was done to better excite the field when the pipe is filled with different LUT. Moreover, a dielectric support for the connector is designed, so to create a planar contact for the connector flange. The dimensions of each part of the structure are reported in the caption of Fig. 5.3(b).

5.2.1 Simulations of the Pumpkin Resonant Cavity

To carry out EM simulations, Ansys HFSS has been used. In Fig. 5.4 the amplitude of the electric modal field of the cavity's first resonant mode (TM_{011}) is shown, when the pipe is empty. Fig. 5.5 reports the magnitude of the simulated S_{11} when the pipe is filled with: air, ISP, a mixture of 45% isopropanol and 55% water, and DI water.

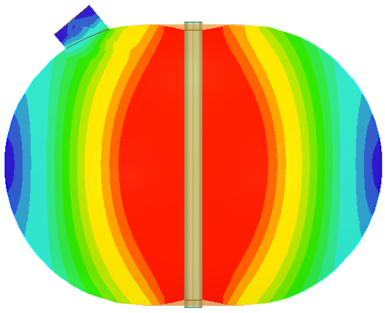

Figure 5.4: Amplitude of the electric modal field of TM_{011}.

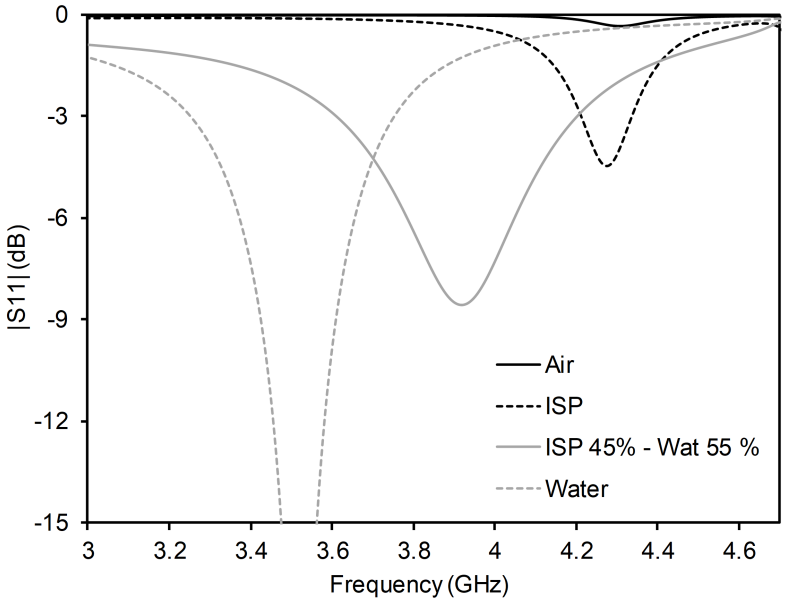

Figure 5.5: Simulated reflection coefficient in four different cases: with empty pipe and with the pipe filled with ISP, a mixture of 45% isopropanol and 55% water, and DI water.

5.3 Fabrication of the Pumpkin Cavity

The design of the structure ready for printing is reported in Fig. 5.6. With respect to the structure used for the simulations, here the resonator is split in two equal parts - to guarantee an easier metallization of the inner parts - and is provided with two screwed flanges that help closing the structure.

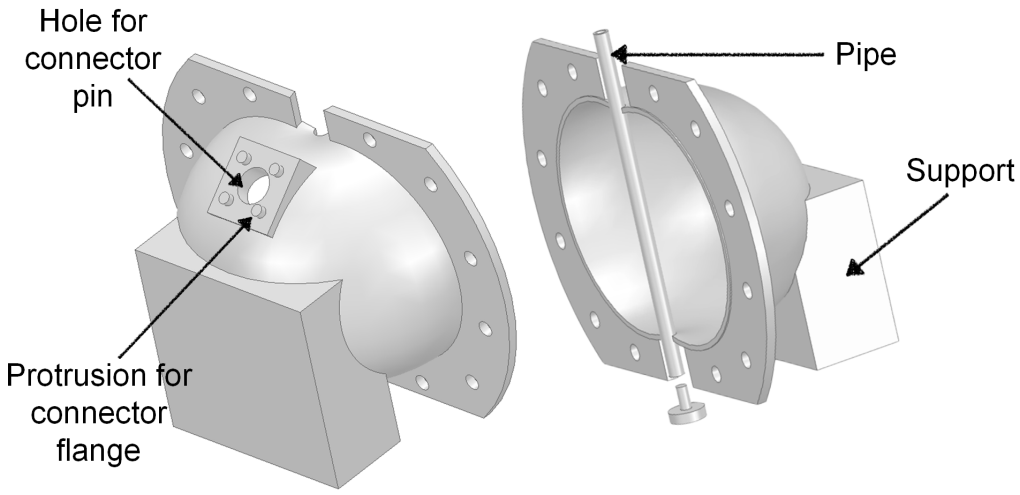

Figure 5.6: Design of the resonator with all the ancillary parts needed to support and close the structure.

As can be noticed, four protrusions were inserted as to help in positioning the SMA connector, and a stopper in order to close the pipe for the measurements, once the LUT has been injected. Moreover, the hole for the connector pin was made larger than the nominal pin diameter. This was done to make the metallization of the surface, which connects the inside of the sensor to the support for the connector, easier and more effective.

The structure was split along the yz plane for a specific reason: in this way, the cut is parallel to the trajectory of the surface current, as shown in Fig. 5.7.

The device was printed using stereolithography technique and the transparent photopolymer resin Clear FLGPCL04. For the metallization, electroplating was used, which guaranteed a uniform deposition of copper in the inner surface of the structure. Fig. 5.8 shows the photograph of the 3D-printed sensor, with the pipe and the cap. The cap is used to keep closed one end of the pipe, while in the other the liquid is injected.

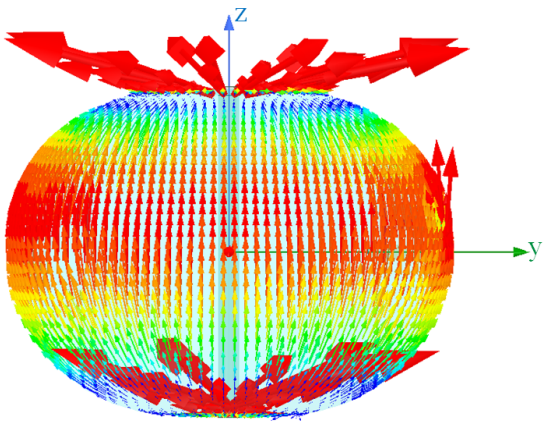

Figure 5.7: Trajectory of the surface current on the pumpkin resonator. The vectors representing its amplitude and directions are parallel to the yz plane.

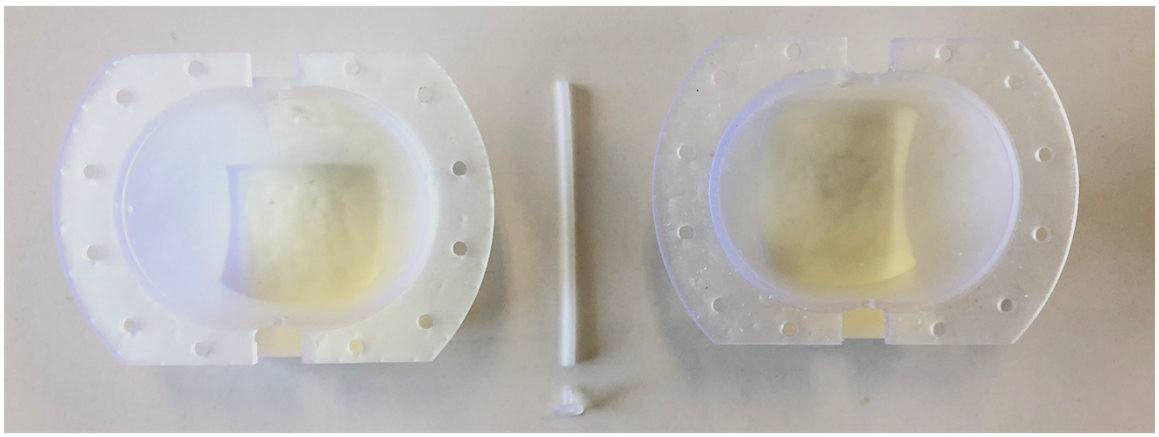

Figure 5.8: Photograph of the sensor taken before the metallization.

5.3.1 Metallization

In order to metalize this particular shape, it is clearly no more possible to use aluminum foils, as was done with the square sensor. A galvanic machine, which exploits electroplating process to perform the metalization, was used. A CopperFace machine, by Robotfactory, was employed, and it is shown in Fig. 5.9.

Figure 5.9: The galvanic machine used to metalize the sensor [7].

The metalization occurs thanks to the voltage difference which is generated, inside the glass containing the electrolytic bath, between the cathode (object) and the anodes. This voltage difference, indeed, entails the deposition of metal on the surface of the object immersed in the acid solution.

The procedure followed to metalize the 3D-printed object consisted of five passages:

1. A silver-copper spray was used to form uniform layers of conductive material on the object;
2. The object was allowed to dry. Step 1 and 2 were repeated until a good conductive layer is created;
3. The object is connected to the metal rod with copper wires, thus forming the cathode, and then inserted in the solution;
4. The magnetic stirrer inside the beaker was turned on;
5. According to the object surface dimensions, the correct galvanic current has to be determined (Robotfactory provides an excel sheet with the function embedded) and used to set the power supply;

6. Once the object is completely metalized, it can be removed from the electrolytic bath, washed with water and then dried with a soft cloth.

Fig. 5.10 shows the two pieces of sensor metalized. To get this result, each of the two pieces was left in the electrolytic bath for half an hour with a current of 1 A.

In Fig. 5.11 a photograph of the sensor ready for the measurements is reported. To hold the SMA connector in place, a bit of glue was used and then conductive paste was applied to create electric contact.

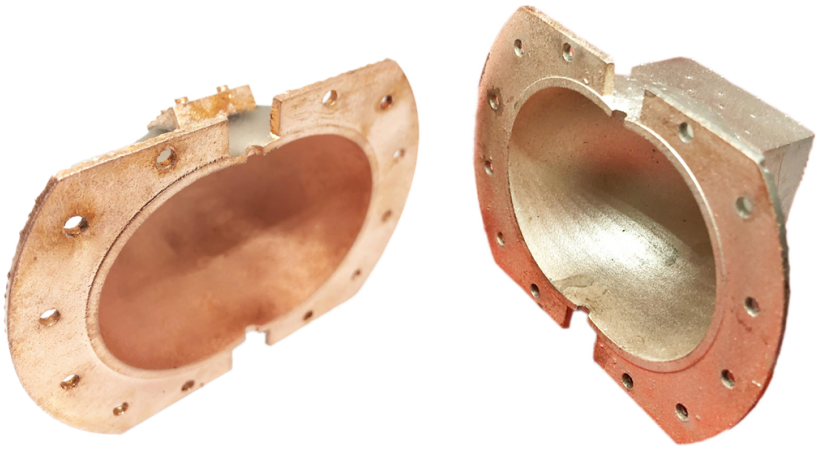

Figure 5.10: The two halves of the pumpkin resonator after the metalization process.

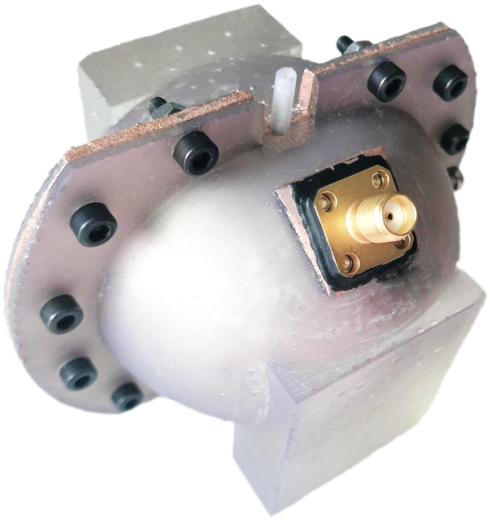

Figure 5.11: The pumpkin resonator closed with the screws and with the SMA connector applied.

5.4 Measurements of the Microfluidic Cavity

The liquids tested in this sensor were the same nine ones used in the square sensor, i.e., mixtures of isopropanol and water from 0% to 100%. As done with the sensor presented in Chapter 3, in order to extract LUTs' electromagnetic properties, the S-parameters of the cavity sensor needed to be retrieved. Fig. 5.12 shows a photograph of the setup employed for the measurements.

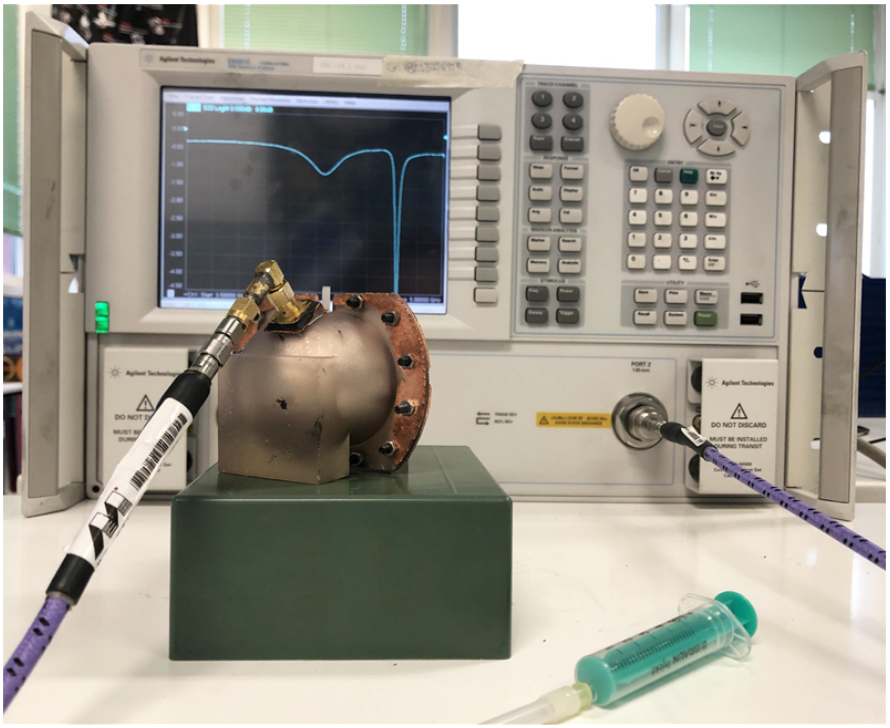

Figure 5.12: Setup for the measurements of the pumpkin sensor's S-parameters.

The sensor was connected, with a flexible cable, to a E8361C PNA Microwave Network Analyzer, which performed S-parameter measurements. The analysis was done sweeping the frequency between 1 GHz to 6 GHz, and the output power was set to -20 dBm, to avoid any microwave heating. A syringe was used to inject the LUT inside the pipe of the sensor, which was closed on the other side with a 3D-printed cap.

Thanks to this measurement setup, the reflection coefficient was measured when filling the pipe with different LUTs. Consequently, by taking the minimum of $|S_{11}|$ and by following the procedure described in subsubsection 2.1.2.1, the resonance frequency and the unloaded quality factor were retrieved.

In Fig. 5.13 the measured $|S_{11}|$ of four different cases (air, isopropanol, mixture 45% isopropanol - 55% water, distilled water) is shown. In this cavity, the resonance frequency changed from $f_{air} = 4.307$ GHz with empty pipe to $f_{wat} = 3.511$ GHz with

water-filled pipe. The retrieved values of resonance frequency and quality factor are reported in Table 5.1.

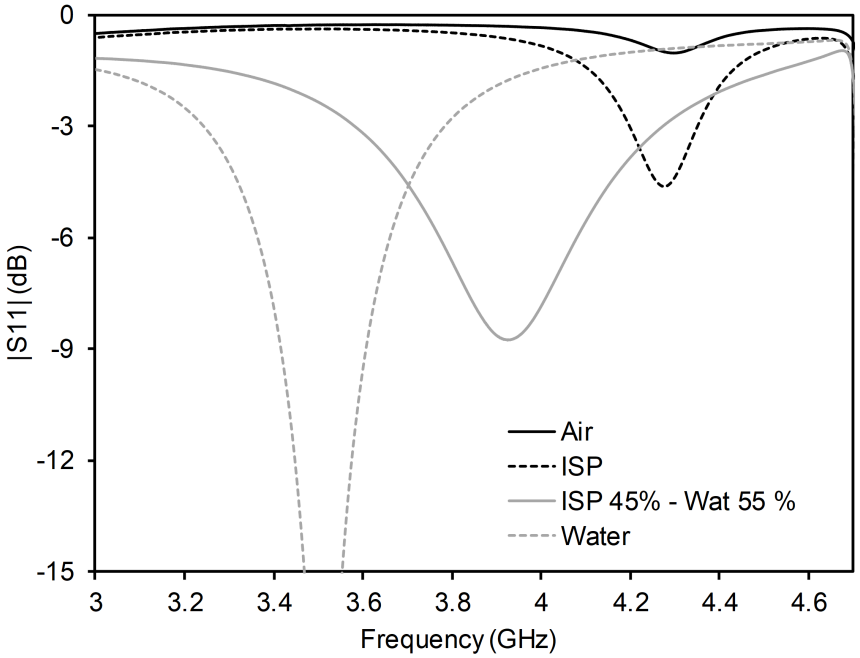

Figure 5.13: Measured scattering parameters for air, isopropanol, mixture 45% isopropanol - 55% water, DI water.

LUT	**Resonance frequency f_0 (GHz)**	**Frequency shift Δf (GHz)**	**Unloaded Q-factor Q_U^{meas}**
Air	4.3072	0	321.35
Isopropanol	4.2763	0.0309	74.73
Isoprop. 85%/Water 15%	4.2334	0.0738	27.28
Isoprop. 75%/Water 25%	4.1934	0.1138	18.26
Isoprop. 60%/Water 40%	4.1022	0.2050	11.29
Isoprop. 45%/Water 55%	3.9272	0.3800	7.28
Isoprop. 30%/Water 70%	3.7766	0.5306	6.69
Isoprop. 20%/Water 80%	3.6816	0.6256	7.54
Isoprop. 10%/Water 90%	3.5778	0.7294	9.13
Water	3.5113	0.7959	12.27

Table 5.1: Values of measured resonance frequency, frequency shift (with respect to empty pipe case) and unloaded quality factor when the pipe is filled with the LUTs.

5.4.1 Retrieval of Liquids Dielectric Properties

In this subsection, the methods used for the extraction of the liquid dielectric permittivity and loss tangent are presented. The loss tangent is retrieved thanks to the approach, presented in Chapter 3, that de-embeds the extra losses; the dielectric permittivity, instead, is extracted by exploiting the measured frequency shift and the loss tangent.

5.4.1.1 Loss Tangent Retrieval

As explained in great detail in subsection 3.4.2, the loss tangent of the LUT can be extracted from the unloaded quality factor by implementing a de-embedding of the extra-losses (Eq. (3.11)) experienced in measurements, which, by definition, in the simulations results are not taken into account.

The grey curve in Fig. 5.14 represents the refined version of the black one, since the losses in the 3D-printed material are taken into account. The black markers (which represent the value of the unloaded Q-factor extracted from the simulations) have been replaced by the white markers, obtained from Eq. (3.11). The isopropanol measured Q-factor, equal to 74.73 (Table 5.1), is also reported with the square marker. By using the measured quality factor and the grey curve, it is possible to retrieve the loss tangent of each LUT. The retrieved values are reported in Table 5.2.

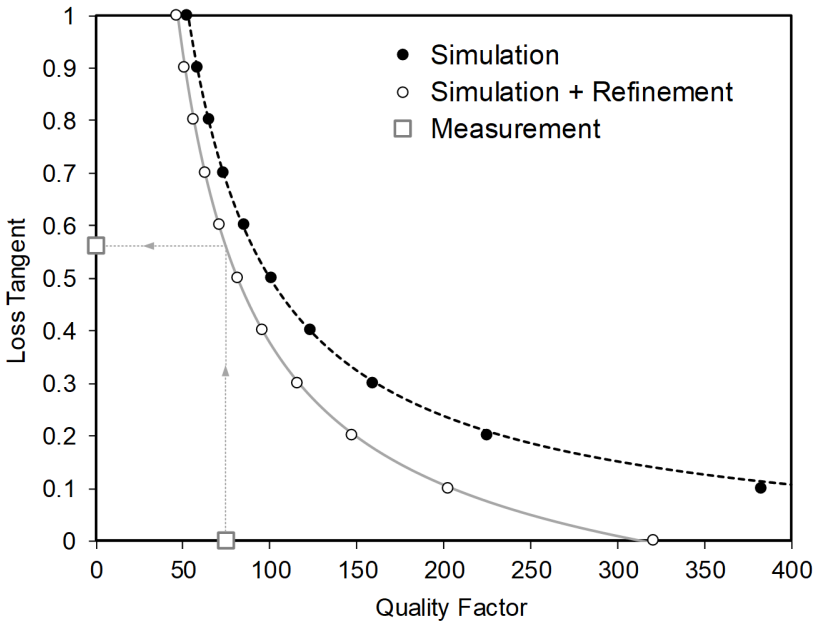

Figure 5.14: Simulated values of the loss tangent versus the unloaded quality factor, extracted from simulations (black markers) and with the refined method (white markers), along with experimental validation for isopropanol.

LUT	**Microfluidic Sensor**	**Coaxial Probe**	**% Relative error**
Isopropanol	0.561	0.539	+4.1
Isoprop. 85%/Water 15%	0.766	0.729	+5.1
Isoprop. 75%/Water 25%	0.763	0.722	+5.7
Isoprop. 60%/Water 40%	0.677	0.662	+2.3
Isoprop. 45%/Water 55%	0.564	0.533	+5.8
Isoprop. 30%/Water 70%	0.448	0.437	+2.5
Isoprop. 20%/Water 80%	0.349	0.33	+5.8
Isoprop. 10%/Water 90%	0.238	0.237	+0.4
Water	0.175	0.166	+5.4

Table 5.2: Loss tangent retrieved by using the novel method and reference values measured with the coaxial probe.

If we compare these results with the ones reported in Table 3.7, we notice that the accuracy is definitely improved.

The pipe shape in the pumpkin cavity is, with respect to the folded shape of the square sensor pipe, simpler and thus more robust to fabrication errors. This results in a greater adherence of the simulations to the measurements, which, in turn, improves the accuracy of the method used to extract the electromagnetic properties of the LUTs.

5.4.1.2 Dielectric Permittivity Retrieval

As explained in Chapter 3, the resonance frequency of a resonant cavity depends on both the dielectric permittivity and the loss tangent. For this reason, in order to extract the dielectric permittivity, we need to know the shift in the resonance frequency as well as the loss tangent. These parameters can be retrieved from the measurements, as explained before. Thus, starting from these data, we want to extract the equation of a polynomial that describe the behaviour of the dielectric permittivity as function of the loss tangent and the Δf.

We simulated the structure with ε_r of the LUT variable between 1 to 100 and with $\tan\delta$ equal to the value extracted from the measurements (as described in the previous section). From those simulations, a distinct ε_r - Δf plot was obtained for the each value of loss tangent, as reported in Fig. 5.15. It can be noticed, as highlighted by the black arrow, that the slope of the fitting line decreases when increasing the loss tangent of the LUT (and for the higher values of Δf). This means that, with the same value

of Δf, the higher is the tanδ the lower is the extracted ε_r.

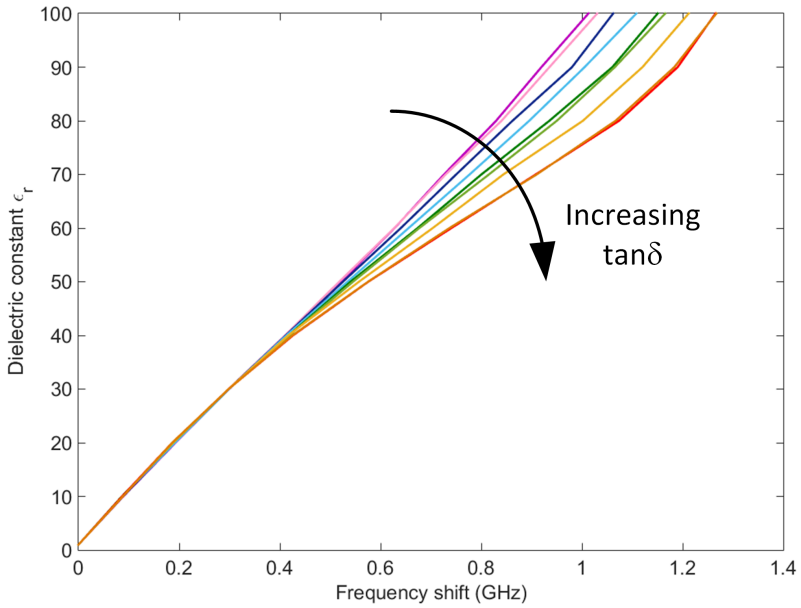

Figure 5.15: Plot of the dielectric permittivity versus the resonance frequency shift with varying loss tangent.

Starting from these simulation results, a polynomial equation was derived that, fitting the data, allowed to extract the dielectric permittivity of the LUT as function of tanδ and Δf:

$$\varepsilon_r(\tan\delta, \Delta f) = p_{00} + p_{01}\Delta f + p_{11}\tan\delta\,\Delta f + p_{12}\tan\delta\Delta f^2 + p_{05}\Delta f^5 \qquad (5.3)$$

where $p_{00} = 1$, $p_{01} = 96.89$, $p_{11} = 17.47$, $p_{12} = -57.32$, $p_{05} = 8.938$. The highly non-linear term means that the spatial distribution of the electric field is lightly modified by its interaction with the LUT in the pipe. This equation guarantees a fitting with R-square = 0.9999 and RMSE < 0.25.

Fig. 5.16 is a 3D-view of this function: on the z-axis the ε_r is reported, while on the x and y axis are, respectively, tanδ and Δf.

Finally, in Table 5.3, the results obtained exploiting (5.3) are compared with the dielectric permittivity extracted with the coaxial probe. The larger errors observed in LUTs with higher concentration of ISP are probably due to the rapid evaporation of the ISP in some conditions, which leads to a different water content in the measurements by coaxial probe compared to the proposed system. As can be noticed, the relative errors are lower than 5% and, in particular, they are definitely lower if compared to the results obtained for the square microfluidic cavity (Table 3.5).

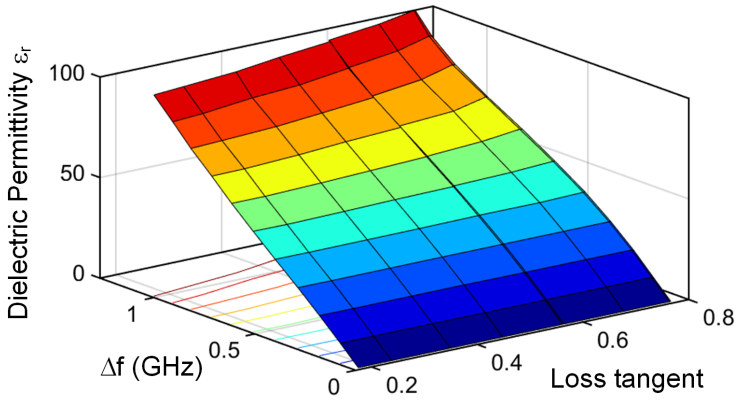

Figure 5.16: 3D-plot of the dielectric permittivity versus the resonance frequency shift with varying loss tangent.

LUT	**Microfluidic Sensor**	**Coaxial Probe**	**% Relative error**
Isopropanol	4.3	4.16	+2.6
Isoprop. 85%/Water 15%	8.9	9.35	-4.8
Isoprop. 75%/Water 25%	13.0	13.61	-4.6
Isoprop. 60%/Water 40%	21.7	22.83	-5.0
Isoprop. 45%/Water 55%	37.0	37.72	-2.0
Isoprop. 30%/Water 70%	49.7	49.43	+0.6
Isoprop. 20%/Water 80%	58.5	58.66	-0.3
Isoprop. 10%/Water 90%	69.3	69.23	+0.1
Water	77.0	75.87	+1.6

Table 5.3: Dielectric permittivity retrieved by using (3.6) and reference values measured with the coaxial probe.

Comparison with the SoA As a conclusion to this chapter, Table 5.4 reports a comparison between the 3D-printed microfluidic sensors presented in this thesis and the state-of-the-art designs proposed in literature. The advantages of the proposed sensors, with respect to other designs, consist in the fact that they allow to characterize liquids in a wide range of permittivities and with a good sensitivity. Moreover, while all the other resonators were realized on standard low loss substrate, the proposed ones have been completely fabricated with 3D-printing.

Sensor	f_{air} (GHz)	$f_{air} - f_{\varepsilon_r}$ (GHz)	ε_r range	Meas. Sensitivity $S = \frac{f_{air} - f_{\varepsilon_r}}{f_{air}(\varepsilon_r - 1)} \cdot 100$	Ref.
Planar resonator & PDMS pipe	22.6	4.7	20-40	0.53	[8]
CSRR & glass pipe	2.37	0.065	9-79	0.03	[9]
CSSR & PDMS pipe	2	0.48	9-79	0.30	[10]
CSRR & PDMS pipe	2	0.7	30-80	0.44	[11]
Planar resonator & 3D-printed pipe	5.3	0.5	8-80	0.11	[12]
Square 3D-printed cavity & pipe	3.82	0.42	4-76	0.15	This thesis
Pumpkin 3D-printed cavity & pipe	4.31	0.8	4-76	0.25	This thesis

Table 5.4: Comparison of the proposed sensors with the state of the art.

5.5 Chapter Summary

In this chapter, a novel design for a microfluidic sensor is presented. The structure, a sphere slightly squeezed at the poles, is particularly interesting because of its high quality factor. In the central part of the cavity a tiny pipe is placed, and here the liquids under test can be easily injected. The cavity is empty - a part from the presence of the pipe - and metallized inside. This permits to increase the unloaded quality factor -with respect to the square cavity - which, in the case of air-filled pipe, is higher than 300. The design principles are outlined, and the steps required to pass from a spherical shape to the actual shape are explained in details. Several measurements have been performed, and mixtures with different concentration of isopropanol have been used in order to test the efficiency of the extraction algorithm introduced in Chapter 3. All the main 3D-printing advantages - possibility to develop complex structure, low cost, fast prototyping - are exploited to realize this structure, which allowed to retrieve with good accuracies the dielectric permittivity and the loss tangent of liquids.

References

[1] D. Rebuzzi, Dip. di Fisica, Università di Roma La Sapienza, *Collezione di risonatori sferici di Helmholtz*, accessed 29 Sept. 2019, `https://www.phys.uniroma1.it/DipWeb/museo/acu12.htm`.

[2] *Resonateurs de Helmholtz*, `http://rhe.ish-lyon.cnrs.fr/instruments-scientifiques/instr_aco_resonnateurs.htm`, accessed 29 Sept. 2019.

[3] S. Gallagher and W. J. Gallagher, "The Spherical Resonator," *IEEE Transactions on Nuclear Science*, vol. 32, no. 5, pp. 2980-2982, Oct. 1985.

[4] C. Guo, X. Shang, M. J. Lancaster and J. Xu, "A 3-D Printed Lightweight X-Band Waveguide Filter Based on Spherical Resonators," *IEEE Microwave and Wireless Components Letters*, vol. 25, no. 7, pp. 442-444, July 2015.

[5] C. Guo, J. Li, D. D. Dinh, X. Shang, M. J. Lancaster and J. Xu, "Ceramic filled resin based 3D printed X-band dual-mode bandpass filter with enhanced thermal handling capability," *Electronics Letters*, vol. 52, no. 23, pp. 1929-1931, 10 11 2016.

[6] C. A. Balanis, *Advanced Engineering Electromagnetics,* Wiley 2012.

[7] Robotfactory `http://lnx.robotfactory.it/it/copperface/`, accessed 19 October 2019.

[8] T. Chretiennot, D. Dubuc and K. Grenier, "A Microwave and Microfluidic Planar Resonator for Efficient and Accurate Complex Permittivity Characterization of Aqueous Solutions," *IEEE Transactions on Microwave Theory and Techniques*, vol. 61, no. 2, pp. 972-978, Feb. 2013.

[9] E. L. Chuma, Y. Iano, G. Fontgalland and L. L. Bravo Roger, "Microwave Sensor for Liquid Dielectric Characterization Based on Metamaterial Complementary

Split Ring Resonator," *IEEE Sensors Journal*, vol. 18, no. 24, pp. 9978-9983, 15 Dec.15, 2018.

[10] A. Ebrahimi, W. Withayachumnankul, S. Al-Sarawi and D. Abbott, "High-Sensitivity Metamaterial-Inspired Sensor for Microfluidic Dielectric Characterization," *IEEE Sensors Journal*, vol. 14, no. 5, pp. 1345-1351, May 2014.

[11] A. Ebrahimi, J. Scott and K. Ghorbani, "Ultrahigh-Sensitivity Microwave Sensor for Microfluidic Complex Permittivity Measurement," *IEEE Transactions on Microwave Theory and Techniques*, vol. 67, no. 10, pp. 4269-4277, Oct. 2019.

[12] B. D. Wiltshire and M. H. Zarifi, "3-D Printing Microfluidic Channels With Embedded Planar Microwave Resonators for RFID and Liquid Detection," *IEEE Microwave and Wireless Components Letters*, vol. 29, no. 1, pp. 65-67, Jan. 2019.

Chapter 6

Conclusions and Future Perspectives

"Home is behind, the world ahead,
and there are many paths to tread
through shadows to the edge of night,
until the stars are all alight."
- J. R. R. Tolkien, *The Lord of the Rings*

6.1 Conclusions on the Contribution of the PhD Research

In last years, 3D-printing has made great strides by offering cutting-edge solutions in the field of rapid prototyping. Additive manufacturing technologies are generally faster and easier to use than other subtractive production technologies. International newspapers and experts have defined 3D-printing as the industrial revolution of this century [1]. And they were not that far wrong. For some time now, the era of the "personal factory" has begun, an era where everything you want can be realized. In particular, 3D-printing is proving to be of great attraction for the production of high performance microwave components [2]. It is within this scenario that my PhD thesis has contributed, being entirely dedicated to 3D-printing technology and its applications in the development of microwave microfluidic platforms.

The major achievements accomplished with this thesis can be summarized in three points:

1. An innovative class of microfluidic cavities, fully fabricated with 3D-printing technologies, has been realized. The proposed prototypes present two great advantages, with respect to common microfluidic sensors: the first benefit consists in a one-step-process fabrication, being that the material used is the same for the all structure. This leads to a reduction of the production times and, consequently, to a cost cutting. The second advantage is the possibility to create complex or unusual shapes, with the cavities almost completely empty, thus guaranteeing a higher quality factor. This particular choice, dictated by the necessity to reduce as much as possible the dielectric losses (which are quite high in 3D-printed materials), is accomplished precisely because of the use of AM technologies.

   Of course, the performance of the proposed sensors cannot attain the results of sensors developed with commonly used dielectric materials. Nevertheless, the low cost and fast prototyping of 3D-printing, together with the good shielding and the potential system integration of SIW technology, represent an important step toward the implementation of this kind of cost-effective devices in future wireless terminals.
2. A novel method for the extraction of dielectric properties of LUTs is presented. In particular, a new efficient algorithm to retrieve the loss tangent of the liquids is described. The developed method allows to de-embed any extra loss (due, for example, to an inaccurate characterization of the 3D-printed material) and then extract the loss tangent of the LUT considered by simply using the measured unloaded quality factor of the cavity. The great potential of this algorithm therefore appears clear: it can be applied, with successful results, to extract the loss tangent of liquids when cavity resonator sensors are used.
3. A platform for dielectric permittivity measurements has been proposed, in view of creating a self-sustained device for liquids characterization. It consists of an oscillator, made on a standard substrate, which presents as resonant part the 3D-printed square sensor. This oscillator was tested with several different liquids, highlighting how this platform - after a simple calibration - allows the retrieval of liquids' permittivity with a reasonable accuracy.

   The great advantage and the novelty of this kind of platform, more than the retrieval method, consists in creating an oscillator with a 3D-printed resonator. The most important benefit, besides the low-cost for short series production, is the high flexibility. This means the possibility of realizing devices with many different shapes, dimensions, and fabrication materials.

The results presented in this PhD thesis are well integrated in the exciting and continuously-growing research field of 3D-printing. All objectives established at the beginning of this work are met - two microwave cavity resonators for liquids characterization were realized, and the designed devices achieved results that contribute to the advancement of microwave 3D-printing research. Moreover, the design and realization of a microwave oscillator, as set in the objectives, was completed and constitutes the first step in the creation of a self-sustained device for LUTs' characterization. This achievement will contribute in founding a future class of microwave components and sensors, that well fit under WSN applications' umbrella.

6.2 Future Perspectives

This PhD work has been conceived to be a step forward in the scenario of cost-effective and fast prototyping technologies for the development of 3D-printed microwave sensing components. This topic has multiple interesting future perspectives, which can be summarized as follows:

- *Microwave 3D-printed flexible sensors.*
  A first step, that can be performed over the short term, could be the investigation and characterization of new 3D-printed materials that can be used to create flexible microwave sensors. For example, there exists an SLA-printable flexible resin that can be adopted to develop permittivity sensors that could be subsequently integrated in devices for smart health applications. This work would thus merge results reported in this manuscript and studies recently conducted by other authors about the possibility of using flexible and stretchable resins in IoT devices [3]-[5].
- *3D-printed devices for multi-frequency liquids characterization.*
  Future work on 3D-printed microfluidic sensors should also deal with the extension of the frequency characterization range. In order to achieve this result, a set of cavity resonators, placed side by side (or one on top of the other) and with a common pipe where the LUT can flow, can be fabricated. This idea, based on a paper by Krupka [8], would exploit cavity resonators of the same shape but different dimensions, so to have different resonant frequency and thus characterize liquids in a wider frequency range.
- *3D-printed multi-mode resonators for liquids characterization.*
  Another aspect that could also be studied in the future, is the possibility to exploit the higher modes of resonant cavities, and not just the fundamental one,

to get a more accurate extraction of the LUT's dielectric parameters. The main advantage of using higher order modes is the fact that they have a higher quality factor with respect to the fundamental mode, feature that would lead to a more accurate loss tangent's retrieval.

- *Development of structures with increased sensitivity.*
  Future work on 3D-printed cavity resonators for liquids characterization could also deal with studies on how to further increase their sensitivity. It is common pratice, indeed, to place the pipe where the fluid is injected in the location of maximum electric field, so as to increase the sensitivity of the device. In order to increase it even further, a possible solution could be to create a ridge inside the cavity, either with metal screws, as is done in [9], or by shaping the dielectric substrate directly during the 3D-printing phase.
- *3D-printed handheld device for biological and chemical applications.*
  A long term objective could be to design and realize the microwave circuitry that is needed to create a handheld and self-sustained device for liquids characterization. This means to add, to the platform presented in Chapter 4, a mixer to bring the signal to the baseband and an ADC or a frequency counter so to easily read the output signal. This chain of components would allow to perform LUT's measurements and obtain results onsite and in realtime. If the purpose was, instead, to use the system as part of a WSN, an upconverter would have to be added to the chain together with, for example, a patch antenna. These last components would allow to complete the system and to use it to acquire data measured remotely.
  The platform, thereby completed, could consequently be employed in different biological or chemical applications. For example, it could constitute a potential alternative to the procedure presently used to estimate the concentration of bacteria or other cells in a liquid, the "OD 600"[1][6]. The estimation of the optical density, indeed, is usually performed through a spectrophotometer, which is an expensive and quite bulky instrument.

At the end, it is possible to conclude that 3D-printing combined with microwave fluidic sensing has a great potential and could have - on a long-term scale - a relevant impact, in research fields as well as in industrial domains of biochemistry and bioengineering.

[1]OD 600 stays for optical density, or absorbance, and represents the measurement, with visible light at $\lambda = 600$ nm, of the turbidity of bacterial cells in liquid cultures.

References

[1] The Economist, April 21st, 2012, *The third industrial revolution*, https://www.economist.com/leaders/2012/04/21/the-third-industrial-revolution, accessed on 26 Sept. 2019.

[2] R. Bahr, B. Tehrani and M. M. Tentzeris, "Exploring 3-D Printing for New Applications: Novel Inkjet- and 3-D-Printed Millimeter-Wave Components, Interconnects, and Systems," *IEEE Microwave Magazine*, vol. 19, no. 1, pp. 57-66, Jan.-Feb. 2018.

[3] W. Su *et al.*, "3D printed wearable flexible SIW and microfluidics sensors for Internet of Things and smart health applications," 2017 IEEE MTT-S International Microwave Symposium (IMS), Honololu, HI, 2017, pp. 544-547.

[4] C. Votzke, U. Daalkhaijav, Y. Mengüç and M. L. Johnston, "3D-Printed Liquid Metal Interconnects for Stretchable Electronics," *IEEE Sensors Journal*, vol. 19, no. 10, pp. 3832-3840, May 15, 2019.

[5] M. Rizwan, M. W. A. Khan, H. He, J. Virkki, L. Sydänheimo and L. Ukkonen, "Flexible and stretchable 3D printed passive UHF RFID tag," *Electronics Letters*, vol. 53, no. 15, pp. 1054-1056, July 20, 2017.

[6] Eppendorf, 2015, https://www.eppendorf.com/product-media/doc/en/148370/Detection_White-Paper_028_BioPhotometer-D30_BioSpectrometer-family_OD600-Measurements-Different-Photometers.pdf, accessed 20 Oct. 2019.

[7] T. R. Jones, M. H. Zarifi and M. Daneshmand, "Miniaturized Quarter-Mode Substrate Integrated Cavity Resonators for Humidity Sensing," *IEEE Microwave and Wireless Components Letters*, vol. 27, no. 7, pp. 612-614, July 2017.

[8] J. A. Krupka, "Measurements of the complex permittivity of highly concentrated aqueous NaCl solutions and ferrofluid employing microwave cylindrical cavities", *Measurement Science and Technology*, 26 095702, July 2015.

[9] T. R. Jones and M. Daneshmand, "The Characterization of a Ridged Half-Mode Substrate-Integrated Waveguide and Its Application in Coupler Design," *IEEE Transactions on Microwave Theory and Techniques*, vol. 64, no. 11, pp. 3580-3591, Nov. 2016.

Highlights of the Ph.D.

In the framework of this joint doctoral degree, I attended three conferences on electrical and microwave engineering, as well as two Ph.D. schools, three courses and tens of technical seminars; I spent a research period of 9 months abroad at the university of Leuven and, during this stay, I held two technical seminars at the Department of Electrical Engineering (ESAT); I have been tutor and teacher assistant for two bachelor courses and a master course of electronic delivered by the University of Pavia; I published 4 conference papers and submitted 2 journal articles.

Attendance to Congresses

- EuMC 2017 - *European Microwave Conference* - Nuremberg, Germany, 8 - 13 October, 2017.
- IMWS-AMP 2018 - *International Microwave Workshop Series-Advanced Materials and Processes* - Ann Arbor, MI, USA, 16 - 18 July, 2018 (conference with presentation).
- XXII RiNEm - *XXII Riunione Nazionale di Elettromagnetismo* - Cagliari, Italy, 3 - 6 September, 2018 (conference with presentation).

Attendance to Schools

- "Transkills. Competenze Strategiche per i Giovani Ricercatori", 4 - 7 July 2017, Villa Vigoni, Loveno di Menaggio (CO), Italy.
- "Linguaggi, problemi e metodi della comunicazione della ricerca scientifica", 6 February - 28 March 2017, Collegio Nuovo - University of Pavia (PV), Italy.

Courses and Seminars

- "Multidimensional inverse problems: applications to hyperspectral imaging", Prof. J. Bioucas Dias (Instituto Superior Técnico, Lisbon, Portugal), 16 - 22 December 2016, University of Pavia (short course).
- "Open access, Open data, open science", Prof. P. Galimberti, 13 February 2017 (short course).
- "Leadership al femminile: costruiscila con noi", Prof. S. Cuomo (SDA Bocconi), 22 - 24 March 2017, SDA Bocconi, Milano (course).
- "Designing Wearable Systems in The Internet of Things", Prof. D. Atienza Alonso (EPFL, Lausanne), 6 - 9 June 2017, University of Pavia (short course).
- "Virtual Modeling and Additive Manufacturing", Prof. F. Auricchio (University of Pavia), 31 October - 14 December 2017, Almo Collegio Borromeo - University of Pavia (course).
- "Technical Writing Lectures for PhD (EWT)", H. de Jonge, 14 December 2017 - 18 January 2018, University of Pavia (short course).
- "Crisi della fisica classica e fisica quantistica", Prof. A. De Ambrosis (Piano Lauree Scientifiche - Sez. Fisica), 6 - 28 February 2018, University of Pavia (course).

- "3D-Printed Microfluidic Sensor in Substrate Integrated Waveguide Technology", ESAT Department, KU Leuven, Belgium, 4 July 2018 and 22 November 2018, seminars held.

- Attendance to over 30 technical seminars delivered by the *Ph.D. School in Electronics, Computer Science and Electrical Engineering*, University of Pavia, between 2016 and 2019.

Period Spent Abroad

I spent 9 months at Katholieke Universiteit of Leuven (Belgium):

- from April 24$^{\text{th}}$ to May 27$^{\text{th}}$ during the A.Y. 2016-2017;
- from March 8$^{\text{th}}$ to July 31$^{\text{st}}$ during the A.Y. 2017-2018;
- from October 1$^{\text{st}}$ to December 14$^{\text{th}}$ and from May 28$^{\text{th}}$ to June 28$^{\text{th}}$ during the A.Y. 2018-2019.

Teaching Activities

- Tutor for the bachelor course of "Circuiti elettrici lineari" ("Campi elettromagnetici e circuiti I"), Prof. L. Perregrini, A. Y. 2016-2017 and A. Y. 2018-2019.
- Teaching assistant for the course of "Antennas and Propagation", Prof. M. Bozzi, A. Y. 2017-2018.
- Tutor for the bachelor course of "Elettronica I", Prof. G. Martini and Prof. S. Merlo, A. Y. 2016-2017 and A. Y. 2018-2019.

List of Publications

1. **G. M. Rocco**, N. Delmonte, M. Bozzi, D. Schreurs, S. Marconi and F. Auricchio "3D-Printed Pumpkin-Shaped Resonator for Liquids Complex Permittivity Extraction," *IEEE Microwave and Wireless Components Letters* (under review).
2. **G. M. Rocco**, P. Barmuta, D. Schreurs, and M. Bozzi, "A Novel Platform to Develop 3D-Printed Sensors for Dielectric Permittivity Measurements," *IEEE Microwave and Wireless Components Letters* (under review).
3. **G. M. Rocco**, M. Bozzi, D. Schreurs, L. Perregrini, S. Marconi, G. Alaimo and F. Auricchio, "3D-Printed Microfluidic Sensor in SIW Technology for Liquids Characterization," *IEEE Transactions on Microwave Theory and Techniques*, 2019.
4. **G. M. Rocco**, M. Bozzi, D. Schreurs, S. Marconi, G. Alaimo, F. Auricchio, "3D-Printed Substrate Integrated Waveguide Cavity for Fluids Characterization," *XXII Riunione Nazionale di Elettromagnetismo (XXII RiNEm)*, 2018.
5. **G. M. Rocco**, M. Bozzi, D. Schreurs, S. Marconi, G. Alaimo, F. Auricchio, "3D-Printed Microfluidic Sensor in Substrate Integrated Waveguide Technology," *IEEE MTT-S International Microwave Workshop Series-Advanced Materials and Processes (IMWS-AMP 2018)*, 2018.
6. M. Bozzi, E. Massoni, **G. M. Rocco**, C. Tomassoni, and L. Perregrini, "New Materials and Fabrication Technologies for Substrate Integrated Waveguide (SIW) Components," *Progress In Electromagnetics Research Symposium (PIERS 2017)*, Singapore, Singapore, 19-22 Nov. 2017 (invited paper).
7. M. Bozzi, S. Moscato, L. Silvestri, E. Massoni, N. Delmonte, **G. M. Rocco**, M. Pasian, L. Perregrini, and C. Tomassoni, "Novel Materials and Fabrication

Technologies for SIW Components for the Internet of Things," *2016 IEEE International Workshop on Electromagnetics: Applications (iWEM2016)*, Nanjing, China, May 16-18, 2016 (invited paper).